

https://dspace.org/

Multiwavelength study of the 2020 and 2021 flares of S5 1803+784 and BL Lacertae

Omojola, Joseph

2022

https://hdl.handle.net/10539/37149

Downloaded from a DSpace repository. https://dspace.org/

Multiwavelength study of the 2020 and 2021 flares of S5 1803+784 and BL Lacertae

Joseph Omojola

A Thesis submitted to the Faculty of Science, University of the Witwatersrand, in fulfilment of the requirements for the degree of Doctor of Philosophy.



Johannesburg, 2022

DECLARATION

I, Joseph Omojola, declare this thesis is my own, unaided work. It is being submitted for the Degree of Doctor of Philosophy at the University of the Witwatersrand, Johannesburg. It has not been submitted before for any degree or examination at any other University.



Joseph Omojola

(Signature of candidate) (Name)

26th day of October 2022 in Johannesburg

ABSTRACT

This thesis presents a detailed spectral and temporal analysis of two blazars (S5 1803+784 and BL Lacertae) during their recent flaring states from 2020 to 2021. They are both low synchrotron peak (LSP) BL Lac objects and reached their highest daily fluxes yet observed during these flares. The time-resolved spectral energy distribution (SED) and the spectral characteristics are used to study the high-energy emission mechanism and the nature and location of the emitting region in the framework of the single-zone leptonic jet model. The phenomenological spectral fits provide some constraints on the characteristics of the jet and emitting region structure, gamma-ray emission process, and the likely driver of particle acceleration. The two sources have unique emission characteristics that suggest the existence of external soft photons from outside the jet (EC) undergoing inverse Compton scattering in addition to synchrotron self-Compton scattering of the synchrotron photons intrinsic to the jet. In the case of S5 1803+784, the temporal analysis indicates six distinct flares, four of which have symmetric profiles, while two are asymmetric.

The broadband SED of S5 1803+784 during the period labeled as Flare A, which peaked on April 12, 2020, was fit to a single-zone model using both synchrotron+SSC only and SSC+EC components. The X-ray emission in the quiescent state comes from inverse Compton scattering, while during the flare, the X-ray forms part of the upper tail of the synchrotron emission due to the acceleration of the emitting particles in the photon radiation field. The best-fit parameters show that the dusty torus (DT) may be the primary source of the external photons responsible for the inverse Compton emission. The synchrotron+SSC only model only fits the data if some parameters have unphysical values, favouring the SSC+EC model. The single-zone leptonic jet model could fit the SED during the flare with an emitting region size of $R = 3.42 \times 10^{16}$ cm and a distance from the central black hole $R_H = 5.00 \times 10^{17}$cm. The size of the emitting region becomes more compact during the flare; one possible scenario is a collapse of the emitting region size, which could be triggered by sudden rearrangement of the magnetic field lines within the emitting region. The hard power-law spectrum of the low energy spectral slope is consistent with magnetic dissipation as the likely driver of particle acceleration during the flare.

The highest daily flux ever observed from BL Lacerate $(64.86 \pm 3.16) \times 10^{-7}\mathrm{cm}^{-2}\mathrm{s}^{-1}$ in the 0.1-300GeV energy range was observed with a flare duration of less than six days. The shortest flare has a duration of 2.1 days; the short variability time scale during the flares was also observed in both the X-ray and the optical wavebands. The BL Lacertae flare labeled as Flare

A1 has an asymmetric flare profile with flare-time gamma-ray flux variability of 84%, the highest observed up to that time from BL Lacertae, with a less than a day variability timescale. The size of the emitting region of $R < 2.70 \times 10^{15}$ cm, estimated using both the VLBI measured Doppler factor and the variability time scale (t_{var}) from the gamma-ray flux cannot fit the SED with either the single-zone synchrotron+SSC-only or the SSC+EC model; the inability of the single-zone model to satisfy this constraint points to the possibility of multiple emitting blobs and that the gamma-ray flux variability timescale (t_{var}) is likely from such blobs. The single-zone SED model produces the best fit with an emitting region of size $R = 1.38 \times 10^{17}$ cm and the distance of the emitting region from the black hole $R_H = 1.37 \times 10^{17}$cm, which were used to constrain and model the SED in two-zone emission SSC+EC models. The two-zone model can reproduce the emitting region's physical features and spectral characteristics during the flare.

In both blazars' SED models, the emitting region is particle-dominated. The gamma-ray emitting region electron low-energy spectral slopes return a hard power-law consistent with magnetic turbulence driven by reconnecting field lines.

The two blazars share some similarities in that they are both BL Lac objects and LSP in their quiescent states, and the same mechanism may be responsible for enhancing particle acceleration in the emitting region during the flares; they require different approaches to explain the emitting region structure and emission processes and the observed fluxes during the flares. While S5 1803+784 SED S5 shows synchrotron-dominated X-ray emission during the flare for the first time, BL Lacertae requires a two-zone model to satisfy the variability time scale constraint.

Dedication

In memory of my father

ACKNOWLEDGMENTS

The acknowledgment must go to Professor Andrew Chen, whose guidance and knowledge have been key to the success of this work. My appreciation goes to the head of the School of Physics, Prof. Deena Naidoo, for his fatherly role and encouragement throughout my studentship. My special thanks go to Prof. Justin Finke, my mentor (in the *Fermi*-LAT mentor-mentee program), for reading the thesis draft and making comments that improved the work, and Prof. Francesco Longo, my recent mentor in the *Fermi*-LAT mentor-mentee program, whose advice and encouragement help me immensely during this research. Worthy of mention are Dr. Deirdre Horan and Dr. Sara Buson for reading and making suggestions on my presentations and publication. I also thank my wife, Abimbola Joseph, my children, and the rest of my family for their prayers, support, and encouragement. I acknowledge funding support from my home university (Federal University of Lafia), Academic Staff Training and Development (ASTD), administered through TETFund. Also, thanks to the South African Gamma-ray Astronomy (SA-GAMMA) Consortium for the 2021 academic session tuition fees support. I acknowledge the *Fermi*-LAT Collaboration's support received during meetings and presentations throughout this work.

My acknowledgments go to the following people who have assisted in getting the multiwavelength data used in my thesis; Prof. Filippo D'Ammando for the *Swift* data, NuSTAR and NICER X-ray data and Prof. Anne Lahteenmaki for the BL Lacertae 37 GHz radio data. Lastly, my appreciation goes to Prof. Andrea Tramacere for the *JetSeT* code.

CONTENTS

DECLARATION ii

ABSTRACT iii

ACKNOWLEDGMENTS vi

LIST OF FIGURES xi

LIST OF TABLES xiv

LIST OF RESEARCH OUTPUT AND PUBLICATIONS xvii

CHAPTER 1 1

1.0 Overview 1

1.1 Blazars 2

1.2 The blazar conundrum 4

1.3 Radiation loss mechanisms in blazar jets 5

1.4 Particle acceleration in relativistic jets 5

1.5 Aims and objectives 7

CHAPTER 2 8

2.0 The leptonic jet model 8

2.1 Synchrotron emission 8

2.2 Inverse-Compton scattering 10

2.2.1 Synchrotron self-Compton scattering 12

2.2.2 External inverse-Compton scattering 12

2.3 Observational tools in blazar studies 14

2.3.1 Multiwavelength observations 14

2.3.1.1 Spectral energy distributions 15

2.3.1.2 Intra-day and long-term light curves 15

2.3.2 Very long baseline interferometry (VLBI) 16

2.3.3 Multi-messenger observations 16

2.4 Magnetic energy dissipation through reconnecting field lines 17

2.5 The photon seed factor 18
2.6 Blazar phenomenological (sequence) trends 18
2.7 Examples of previous studies of BL Lacetae and S5 1803+784 19
CHAPTER 3 21
3.0 Blazar observations, analysis methods, and SED modelling 21
3.1 Observation of blazar jets with the *Fermi* Large Area Telescope 21
3.1.1 *Fermi* Large Area Telescope 21
3.1.2 *Fermi*-LAT data analysis 21
3.1.3 *Fermi*-LAT analysis procedure 22
3.1.4 *Fermi*-LAT Gamma-ray emission spectra 23
3.2 Flare definition and description 23
3.3 Archival data 27
3.4 Radio data 27
3.4.1 Metsähovi Radio Observatory 27
3.5 Swift Telescope data 29
3.5.1 S5 1803+784 Swift/XRT/UVOT data 29
3.5.2 BL Lacertae Swift/XRT/UVOT data 30
3.6 Other optical and X-ray data used in the SED model 33
3.6.1 ATLAS data 33
3.6.2 NuSTAR and NICER X-ray data observations from BL Lacertae 35
3.7 *JetSeT* code implementation of the leptonic jet model 35
3.7.1 Synchrotron and SSC model 35
3.7.2 External inverse-Compton model 36
3.7.3 Electron distributions and the radiating particle model 36
3.7.4 Emitting region energy densities 38
3.7.5 *JetSeT* 39
3.7.5.1 Phenomenological spectral fits and model minimizers 39

3.7.5.2 Markov chain Monte Carlo (MCMC) sampling....40
3.8 Minimum Doppler factor....40
3.9 BL Lacertae multiwavelength flux doubling timescale....41
CHAPTER 4....42
4.0 Multiwavelength flux variability and inverse Compton external seed photons....42
4.1 Gamma-ray flux variability....42
4.2 BL-Lacertae X-ray flux variability....43
4.3 BL-Lacertae radio flux variability....44
4.4 Flaring period photon seed factor....45
CHAPTER 5....51
5.0 S5 1803+784 (4FGL J1800.6+7828)....51
5.1 S5 1803+784 flares of 2020 April to 2021 April....51
5.1.1 S5 1803+784 gamma-ray emission model and characteristics....52
5.1.2 Temporal profiles of S5 1803+784 flares and broadband spectral fits....56
5.1.3 Multiwavelength SED of S5 1803+784....57
5.1.4 Phenomenological spectral best fits of S5 1803+784....64
5.2 Gamma-ray emission and acceleration processes in S5 1803+784....65
CHAPTER 6....66
6.0 Recent flares of BL Lacertae (4FGL J2202.7+4216)....66
6.1 BL Lacertae flares of 2020 August to 2021 August....66
6.1.1. BL Lacertae gamma-ray spectra and characteristics during the 2020 to 2021 flares....67
6.1.2 Temporal characteristics of BL Lacertae during the 2020 and 2021 flares....71
6.2 Multiwavelength SED model of BL Lacertae using simultaneous data....73
6.3 Implications for gamma-ray emission and the emitting region....80
CHAPTER 7....82
7.0 Results outlook....82

7.1 Implications of the single-zone fits to the multiwavelength SEDs with *JetSeT* 82
7.1.1 S5 1803+784.....82
7.1.2 BL Lacertae 83
7.2 Two-zone multiwavelength SED model of BL Lacertae Flare A1.....84
CHAPTER 8 91
8.0 Summary of results and conclusion 91
8.1 Summary of results.....91
8.1.1 S5 1803+784.....91
8.1.2 BL Lacertae 92
8.2 Conclusion and outlook.....93
REFERENCES.....95
APPENDIX 106

LIST OF FIGURES

CHAPTER 1

Figure 1. Schematic diagram (not to scale) describing the unified model of a radio-loud AGN (Cerruti, 2020) showing the narrow-line region (NLR), the broad line region (BLR) and the dusty torus (DT) in relation to the accretion disk and the central black hole (BH).

CHAPTER 2

CHAPTER 3

Figure 3.1: (Left panel) The 30-day binned *Fermi*-LAT light curve of S5 1803+784.
(Right panel) The BL Lacertae 30-day binned *Fermi*-LAT light curve. The light curves are from the onset of *Fermi*-LAT observations from 2008-08-04 to 2022-03-30 (MJD 54682-MJD 59668).

Figure 3.2: (Upper panel) The Bayesian blocks of S5 1803+784. (Lower panel) The Bayesian blocks of BL Lacertae.

Figure 3.3: S5 1803+784 gamma-ray light curve (upper left), radio light curve (lower left) and the LCCF (right panel) (2019-05-30 to 2020-06-30) (Edelson and Krolik, 1988; Max-Moerbeck *et al.*, 2014; Robertson *et al.*, 2015).

Figure 3.4: BL Lacertae gamma-ray light curve (upper left), radio light curve (lower left) and the LCCF (right panel) of the flare period (2020-07-30 to 2021-08-30) (Edelson and Krolik, 1988; Max-Moerbeck *et al.*, 2014; Robertson *et al.*, 2015).

Figure 3.5: Leptonic jet model and definitions of parameters used in the *JetSeT* code (not to scale).

Figure 3.6: Emitting region model description (not to scale).

CHAPTER 4

Figure 4.1: Flare A1 Swift/XRT 0.3-10 keV light curve.

Figure 4.2: Flare period 37 GHz radio light curve

Figure 4.3: (a) S5 1803+784 polynomial fit to determine the peak fluxes and frequencies (Flare A1).

Figure 4.4: (b) S5 1803+784 polynomial fit to determine the peak fluxes and frequencies (Quiescent state).

Figure 4.5: (a) BL Lacertae polynomial fit to determine the peak fluxes and frequencies (Flare

A1).
Figure 4.6: (b) BL Lacertae polynomial fit to determine the peak fluxes and frequencies (Quiescent state).
CHAPTER 5

Figure 5.1: S5 1803+784 Bayesian block showing the period of the flares and the flare epochs in a daily binned light curve (0.1-300 GeV).

Figure 5.2: The gamma-ray spectra of the six flares of S5 1803+784 fitted with three spectral models (continued on the next page).

Figure 5.3: Temporal profiles of the flares, each fitted with the function in Equation 3.6.

Figure 5.4: Multiwavelength light curve of S5 1803+784.

Figure 5.5: (a) S5 1803+784 broadband SED (Quiescent state, best-fit SSC model); (b) Residual of the fit.

Figure 5.6: (a) S5 1803+784 broadband SED (Quiescent state, best-fit SSC model), where the shaded area is the upper and the lower bounds of the MCMC sampling; (b) Residual of the fit.

Figure 5.7: (a) S5 1803+784 broadband SED (Quiescent state, best-fit SSC+EC model); (b) Residual of the fit.

Figure 5.8: S5 1803+784 broadband SED (Quiescent state, best-fit SSC+EC model), where the shaded area is the upper and the lower bounds of the MCMC sampling; (b)Residual.

Figure 5.9: (a) S5 1803+784 broadband SED (Flare A, best-fit SSC model); (b) Residual of the fit.

Figure 5.10: (a) S5 1803+784 broadband SED (Flare A, best-fit SSC model), where the shaded area is the upper and the lower bounds of the MCMC sampling; (b) Residual of the fit.

Figure 5.11: (a) S5 1803+784 broadband SED (Flare A, best-fit SSC+EC model); (b) Residual of the fit.
Figure 5.12: (a) S5 1803+784 broadband SED (Flare A, best-fit SSC+EC model), where the shaded area is the upper and the lower bounds of the MCMC sampling; (b) Residual of the fit.

CHAPTER 6

Figure 6.1: The daily binned light curve of BL Lacertae at 0.1-300 GeV during the flare.
Figure 6.2: Bayesian blocks light curve (LC) of BL Lacertae during the 2020 and 2021 flares in daily (upper panel) and 12 hourly bins (lower panel).

Figure 6.3: The gamma-ray spectra of the BL Lacertae flares fitted with three spectral models (continued on the next page).

Figure 6.4: The temporal profiles of the flares fitted with the function in Equation 3.6 (continued on the next page).

Figure 6.5: Multiwavelength light curves of BL Lacertae during the 2020 and 2021 flaring periods.

Figure 6.6: (a) BL Lacertae broadband SED (Quiescent state, best-fit SSC model); (b) Residual of the fit.

Figure 6.7: (a) BL Lacertae broadband SED (Quiescent state, best-fit SSC+EC model); (b) Residual of the fit.

Figure 6.8: (a) BL Lacertae broadband SED (Flare A1, best-fit SSC model); (b) Residual of the fit.
Figure 6.9: (a) BL Lacertae broadband SED (Flare A1, best-fit SSC model) using an emitting region size of 2.60×10^{15}cm as constrained by t_{var}; (b) Residual of the fit.
Figure 6.10: (a) BL Lacertae broadband SED (Flare A1, best-fit SSC+EC model); (b) Residual of the fit.
BL Lacertae broadband SED (Flare A1, best-fit SSC+EC model) using an emitting region size of 2.60×10^{15}cm as constrained by t_{var}; (b) Residual of the fit.

CHAPTER 7

Figure 7.1: BL Lacertae jet components and the emitting region location and structure (not to scale).
Figure 7.2: BL Lacertae two-zone SSC leptonic jet model fit to the quiescent state.
Figure 7.3: BL Lacertae two-zone leptonic jet SED model of the quiescent state.
Figure 7.4: BL Lacertae two-zone leptonic jet SED model of Flare A1.

LIST OF TABLES

CHAPTER 1

CHAPTER 2

Table 2.1: List of blazars studied and their characteristics.

CHAPTER 3

Table 3.1: (a) The flaring period of S5 1803+784 and their labels used in this work.

Table 3.1: (b) The flaring period of BL Lacertae and their labels used in this work.

Table 3.2: 4FGL-DR2 catalog 10-year average flux.

Table 3.3: BL Lacertae 37 GHz radio data for October 2020 flare.

Table 3.4: BL Lacertae Swift/XRT data simultaneous with Flare A1.

Table 3.5: V-band BL Lacertae data simultaneous with Flare A1.

Table 3.6: B-band BL Lacertae data simultaneous with Flare A1.

Table 3.7: U-band BL Lacertae data simultaneously with Flare A1.

Table 3.8: S5 1803+784 ATLAS c-filter of the B-band data simultaneous with Flare A.

Table 3.9: S5 1803+784 ATLAS o-filter of the R-band data simultaneous with Flare A.

Table 3.10: NuSTAR orbit-by orbit observations of BL Lacertae 2020 October 11-12 (3-79 keV).

Table: 3.11: BL Lacertae multiwavelength flux doubling timescale.

CHAPTER 4

Table 4.1: S5 1803+784 fractional variability amplitudes for Flare A and the entire duration of the Fermi-LAT observations up to 2022-03-30.

Table 4.2: BL Lacertae fractional variability amplitude estimation for Flare A1 and the entire duration of the Fermi-LAT observation up to 2022-03-30.

Table 4.3: Flare A1 X-ray flux variability amplitude.

Table 4.4: Flare-period radio flux variability amplitude.

Table 4.5: Summary of the peak fluxes and frequencies of the flares.

Table 4.6: Summary of the peak fluxes and frequencies of the quiescent states.

Table 4.7: Observer frame (obs) synchrotron and inverse Compton peak luminosities, and the photon seed factor during the flares.
Table 4.8: Observer frame synchrotron and inverse Compton peak luminosities in the quiescent states.

CHAPTER 5

Table 5.1: Using the log-parabola model, spectral characteristics of the gamma-ray spectrum of S5 1803+784 during the flares.
Table 5.2: Comparison of the gamma-ray spectra models for S5 1803+784.

Table 5.3: Comparison of the gamma-ray spectra parameters of the log parabola (LP) distribution function for the two blazars. LT is the long-term SED from 2008/08/04-2022/03/30; FT is the 2020-2021 flare period, and Flare A is defined in the text.
Table 5.4: Temporal characteristics of S5 1803+784 during the flares.
Table 5.5: SSC+EC leptonic model parameters fixed in the quiescent state.

Table 5.6: Best fit parameters of S5 1803+784 for the quiescent state, SSC only and SSC+EC model.

Table 5.7: Best fit parameters of S5 1803+784 SSC only and SSC+EC leptonic model.

Table 5.8: Emitting region energy densities of S5 1803+784 during Flare A.

CHAPTER 6

Table 6.1: Spectral characteristics of the gamma-ray spectra during the flares using the log parabolic distribution.
Table 6.2: Comparison of the gamma-ray spectra models for BL Lacertae.

Table 6.3: Comparison of the gamma-ray spectra parameters of the log parabola (LP) distribution function for the two blazars. LT is the long-term SED from 2008/08/04-2022/03/30; FT is the 2020-2021 flare period, and Flare A1 is defined previously.

Table 6.4: Temporal characteristics of BL Lacertae during the 2020 and 2021 flares.
Table 6.5: SSC+EC jet structure parameters during the flare.

Table 6.6: SSC only and SSC+EC quiescent state best-fit parameters.

Table 6.7: SSC only and SSC+EC Flare A1 best fit parameters.

Table 6.8: Emitting region energy components of BL Lacertae jet during Flare A1.

CHAPTER 7

Table 7.1: Synchrotron+SSC and SSC+EC quiescent and flaring states best-fit parameters.

Table 7.2: Two-zone SED model best-fit parameters of the quiescent state (Q).

Table 7.3: Two-zone SED model best-fit parameters of Flare A1.

LIST OF RESEARCH OUTPUT AND PUBLICATIONS

Publications

Part of the thesis initial results titled: 'Spectral analysis of S5 1803+784 in the recent flaring state' was published in the High Energy Astrophysics in Southern Africa Proceeding of Science (HEASA-POS).

Multiwavelength study of S5 1803+784 during 2020 and 2021 flares. Submitted for Fermi Collaboration internal review.

Multiwavelength features of BL Lacertae object flare of 2020 October 6 and its inconsistency with single-zone leptonic model. Submitted for Fermi Collaboration internal review.

Conferences attended and presentations

Part of the research was presented during the 10th International Fermi Symposium held between 9-15 October 2022.

Part of the work was presented at the High Energy Astrophysics in Southern Africa (HEASA) conference held between 13-17 September 2021 (Virtual).

Poster presentation at the South African Institute of Physics (SAIP) Conference held between 22-30 July 2021 (Virtual).

Part of the research was also presented during the Ninth International Fermi Symposium held between 12-17 April 2021 (Virtual).

Poster Presentation at the 30th Texas Symposium on Relativistic Astrophysics in Portsmouth, UK, held between 15-20 December 2019.

CHAPTER 1

1.0 Overview

Active galactic nuclei (AGN) are bright, compact regions in the center of certain galaxies, bright enough that they can be detected at cosmological distances, up to a redshift of z = 7.5, and often far outshine their host galaxies (e.g., Bañados *et al.*, 2018; Cerruti, 2020). The AGN unified model (Figure 1) consists of a system of a supermassive black hole (SMBH) of 10^{8-9} solar masses, which accretes matter forming an accretion disk surrounded by a parsec scale obscuring dusty torus. The disk thermal emission ionizes clouds of matter orbiting the black hole; the in-falling matter is strongly heated in the inner part of the accretion disk and is assumed to be Comptonized by the hot corona, producing power-law X-ray emission (Abdo *et al*., 2010). The ionized matter then re-emits radiation, with emission lines in the optical/UV from both the broad-line region (BLR) close to the black hole at the sub-parsec scale and the narrow-line region (NLR) at much larger distances beyond the dusty torus (Cerruti, 2020). Not all AGN have observable dust tori or BLR, especially the sub-category of blazars called BL Lac objects (this will be discussed subsequently). About 10% of AGNs are radio-loud and are usually non-thermal jet-dominated AGNs (Wilson and Colbert, 1995). Only about ~10% of the radio-loud AGNs are classified as blazars. Their radio jets are closely aligned with our line of sight and are characterized by rapid variability and high luminosity (e.g., Urry and Padovani, 1995). Due to these extreme properties, the physical mechanism(s) responsible for blazar high energy emission and particle acceleration processes are still keenly debated. The multiwavelength study of the 2020 and 2021 flares of S5 1803+784 and BL Lacertae is presented in eight chapters. Chapter 1 is the introduction and contains definitions of keywords used in this thesis. Chapter 2 briefly reviews relevant background and references, and Chapters 3 and 4 discuss the research approach, materials, and methods. The results are presented in Chapter 5 and Chapter 6. Chapter 7 further discusses the implications. The conclusion and outlook are discussed in Chapter 8.

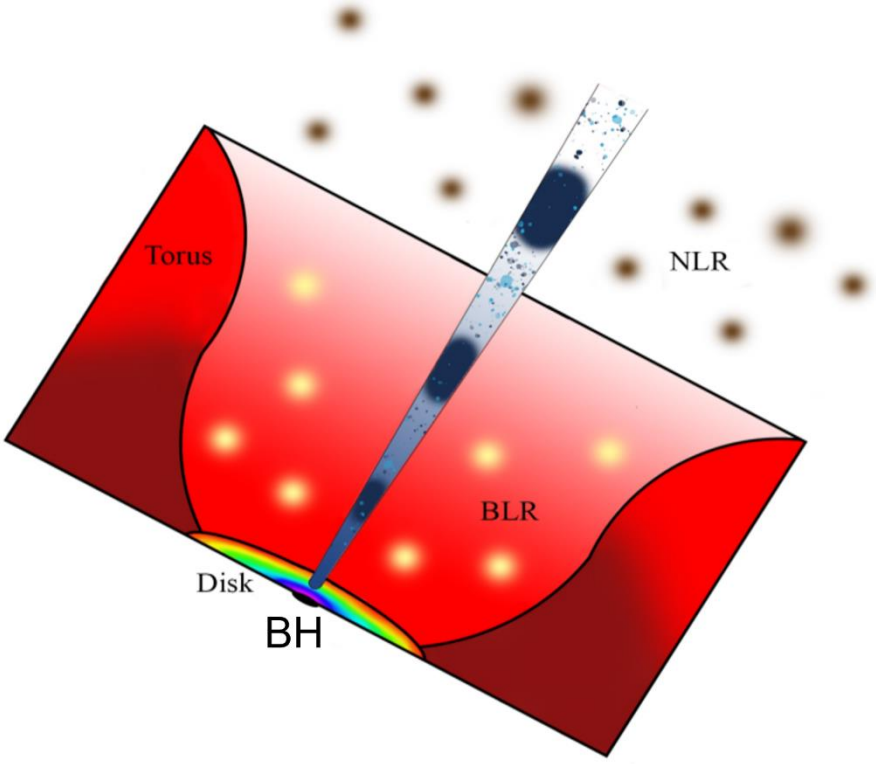


Figure 1. Schematic diagram (not to scale) describing the unified model of a radio-loud AGN (Cerruti, 2020) showing the narrow-line region (NLR), the broad line region (BLR) and the dusty torus (DT) in relation to the accretion disk and the central black hole (BH).

1.1 Blazars

Blazars are a class of active galactic nuclei (AGN) with extreme properties and jets aligned with our line of sight. They are efficient particle accelerators with time-varying emission that spans the entire electromagnetic spectrum. Blazars constitute a subclass of radio-loud (ratio of its radio (5GHz) to its optical (B-band) flux ≥ 10) AGN. The observed broadband spectra are dominated by the beamed and highly variable emission of the innermost parts of relativistic jets (e.g., Dondi and Ghisellini, 1995; Urry and Padovani, 1995).

The broadband spectral energy distribution (SED) is characterized by a double bump structure. The low energy bump results from synchrotron radiation from non-thermal relativistic electrons interacting with the magnetic field in the jet, which usually peaks between IR and the X-ray energies. The high energy bump that peaks between the X-ray and gamma-ray is believed to be due to inverse Compton scattering of either low energy synchrotron photons in the synchrotron self-Compton (SSC) scenario or photons from sources external (external Compton) to the jet (e.g., Finke, 2013) such as from the accretion disk, re-emitted ultraviolet/optical photons from the broad line region or infrared photons originating from the

dusty torus. These scenarios fall under the leptonic jet model of blazar emission (Dermer, Schlickeiser and Mastichiadis, 1992; Bloom and Marscher, 1996; Kataoka *et al.*, 1999; Dermer and Schlickeiser, 2002; Dermer *et al.*, 2009; Böttcher *et al.*, 2013).

The double bump structure in the SED could also be explained using hadronic models. The high energy bump could result from synchrotron emission from protons or secondary decay products of charged particles consisting mainly of pions (e.g., Böttcher *et al.*, 2013).

Blazars are generally flat-spectrum radio quasars (FSRQs) and BL Lacertae objects (BL Lacs). They are classified based on their optical spectra as FSRQs if they have strong emission lines and BL Lacertae objects (BL Lacs) if these lines are weak or absent (e.g., Marcha *et al.*, 1996; Landt *et al.*, 2004). FSRQs and BL Lacs are AGN with flat radio spectra hosting jets oriented at a very small angle ($\leq 15-20°$) to our line of sight. Ghisellini et *al.,* (2011) proposed a more physical criterion based on the ratio of the BLR luminosity (L_{BLR}) to the Eddington luminosity (L_{Edd}). The FSRQs have $L_{BLR}/L_{Edd} > 5 \times 10^{-4}$ and BL Lacs have $L_{BLR}/L_{Edd} < 5 \times 10^{-4}$.

The peak frequency (ν_{p}) of the synchrotron component of the spectral energy distribution can further be used to classify blazars into low synchrotron peaked (LSP) (LSP, synchrotron frequency, $\nu_{\mathrm{p}} < 10^{14}$Hz), intermediate synchrotron peaked (ISP, ν_{p} between 10^{14}Hz and 10^{15}Hz) and the high synchrotron peaked (HSP, $\nu_{\mathrm{p}} > 10^{15}$Hz) blazars. The peak frequencies of FSRQs are usually within the LSP range (Marcha and Browne, 1996; Landt *et al.*, 2004; Xue-Pin, Xiong-Wei and Yong-Gang, 2018; Padovani *et al.*, 2019). The extreme inferred isotropic luminosities, combined with the rapid high-energy variability and the radiative and particle acceleration mechanisms involved in the production of the observed radiation, provide convincing evidence that the high-energy emission from blazars originates in relativistic jets. The jet is caused by bulk relativistic motion described by the bulk Lorentz factor, Γ $\left(\text{where } \Gamma = 1/(1-\beta^2)^{1/2}, \quad \beta = v/c\right)$, in close alignment with our line of sight and the jet boosted in the direction of movement with Doppler factor $\delta = [\Gamma(1-\beta cos\theta_v)]^{-1}$ where θ_v is the viewing angle of the jet in the observer's frame. Several theories have supported the idea that jets are highly magnetized near the central engine of blazars (Zhang *et al.*, 2015, 2016; Bisnovatyi-kogan, 2019). However, their composition, magnetic field structure, topology, and particle acceleration mechanism are still subjects of intense study.

1.2 The blazar conundrum

The mechanism and processes responsible for launching, collimating, and accelerating particles in relativistic jets are not fully understood (e.g., Romero *et al.*, 2017). However, there seems to be agreement on the two most likely sources of power responsible for relativistic jets via either the gravitational energy of the accreting matter or the rotational kinetic energy of a spinning black hole (Blandford and Znajek, 1977; Ghisellini, 1996).

The structure of the relativistic jet, the matter density and particle acceleration, the magnetic field evolution, their compositions and how they interact with the accretion disk power and the black hole are needed to fully understand the physics and evolution of the gamma-ray emission region in blazar jets.

It is generally accepted that the exact location of high energy emission of blazars (also known as the blazar zone) is constrained by the distance of the emitting region from the accretion disk: If it is too close to or within the broad line emission region, then due to the intense radiation field, the produced gamma rays are absorbed in γ-γ collisions. However, the possibility of the emission region being located at large distances from the central SMBH poses a problem for explaining the observed short variability timescales in blazars (e.g., Begelman, Fabian and Rees, 2008; Saito *et al.*, 2013; Ackermann *et al.*, 2016). This problem may be avoided if there is particle acceleration enhancement close to the emission region, which could be produced by processes that involve magnetic dissipation, especially with the recent assertion of Harvey, Georganopoulos and Meyer, (2020), that powerful blazars seem to dissipate their energy far from the black hole, outside the BLR.

Space- and ground-based gamma-ray telescopes are parts of the available tools to observe high-energy radiation produced in blazar jets. The data from these telescopes allow us to constrain how particles in the jets are accelerated to relativistic speeds and the mechanism of jet emission despite their relatively poor angular and energy resolutions compared to lower-energy telescopes. In most cases, what can be measured are the photons fluxes and energies as a function of time. Here I study the time-evolving phenomenological spectral energy distribution (SED) of the jet energetics during the period of high activity (increase in photons fluxes, otherwise known as flares) and in the quiescent state of the selected blazars to explore both the acceleration mechanism and the emission processes.

1.3 Radiation loss mechanisms in blazar jets

Radiation losses in particles depend on whether they are leptons or hadrons and the presence or absence of a magnetic field. In a magnetic field, synchrotron radiation, which is of considerable importance, occurs because of the gyro-motion of relativistic electrons spiraling in a magnetic field. The second radiation loss mechanism important to blazar emission is inverse-Compton (IC) scattering, where energetic electrons up-scatter soft seed photons resulting in high-energy radiation. The inverse-Compton process can be further categorized into synchrotron self-Compton (SSC) due to inverse Compton scattering of relativistic electrons with the seed photons originating from the synchrotron process within the jet or by external Compton (EC) photons from outside the structure of the jet, especially re-emitted photons from the broad-line emission region and the dusty torus of the accreting black hole (e.g., Dermer *et al.*, 1992; Sikora, 1994; Finke, 2013; Böttcher *et al.*, 2013). The detailed treatment of the relevant radiation mechanisms is in Chapter 2 under the leptonic jet model. In the hadronic model, protons are accelerated to ultra-relativistic energies, which leads to proton-synchrotron radiation or photon-pion production and subsequent decay into high-energy photons and pairs. Here we concentrate on applying the leptonic jet model.

1.4 Particle acceleration in relativistic jets

While several analytical and numerical models have been put forward to explain particle acceleration in blazars, the physical mechanisms are not fully understood. The highly energetic radiation could imply that particles are accelerated close to or within the emitting region by mechanism(s) yet to be fully resolved using observations and numerical simulation studies. Scenarios of particle acceleration are divided into two broad categories: when the accelerated particles are predominantly electrons (leptonic model) or protons (hadronic model). Particle acceleration is the mechanism through which non-thermal particles (either leptonic or hadronic) attain relativistic energies in extragalactic sources (Bhattacharyya, Sahayanathan and Kaul, 2002).

Understanding relativistic jets in active galactic nuclei (AGN) is one of the open questions in high-energy astrophysics. It is assumed that a rotating black hole (Kerr black hole) is threaded by magnetic field lines supported by external currents flowing in an equatorial disk and generates an induced electric potential difference. The power in the form of Poynting flux is extracted from the black hole spin or the accretion disk. The jets are produced close to the centrally located supermassive black hole (SMBH) through the Blandford-Znajek mechanism

(BZ); if angular momentum and magnetic fields exist in the black hole system, the BZ mechanism will transform gravitational energy into non-thermal radiation (Blandford and Znajek, 1977). To understand this energetic phenomenon, numerous space-based gamma-ray telescopes have been built, such as the Energetic Gamma Ray Experiment Telescope (EGRET) (Nolan *et al.*, 1992), AGILE (Astro-Rivelatore Gamma a Immagini Leggero) (Pittori *et al.*, 2009), and the *Fermi* Gamma-ray Space Telescope (*Fermi*-LAT) (Abdollahi *et al.*, 2020) sensitive to gamma rays from MeV to GeV. The currently operating ground-based Imaging Atmospheric Cherenkov Telescopes (IACTs), such as the High Energy Stereoscopic System (H.E.S.S) (Aharonian *et al.*, 2006, 2007; Abdalla *et al.*, 2019), the Major Atmospheric Gamma Imaging Cherenkov (MAGIC), and Very Energetic Radiation Imaging Telescope Array System (VERITAS) (Hovatta and Lindfors, 2019), as well as the upcoming Cherenkov Telescope Array (CTA) (CTA Consortium, 2019), explore the TeV energies. The standard Blandford-Znajek mechanism cannot explain the extreme properties of the minute-scale variability of gamma-ray flares observed in some blazars (e.g., Lyutikov *et al.*, 2018). The existence of stochastic (second-order Fermi acceleration) and diffusive shock processes (first-order Fermi acceleration) of the particle acceleration close to the emission region are invoked to explain the rapid variability observed in the high and very high energy (VHE) emission in blazars (e.g., Kapanadze, Vercellone and Romano, 2020). Although various analytical and numerical models have been put forward to explain particle acceleration in blazars, the physical mechanisms are seldom fully understood.

The theoretical modelling and interpretation of multiwavelength emission in blazars are complicated by rapid variability and inconsistencies in the cross-correlation of the multi-wavelength observations. It is often difficult to reconcile the observed emission with a particular acceleration mechanism (e.g., Böttcher, 2019). It is agreed that the formation of strong shocks and efficient particle acceleration in the emitting region is consistent with a high ratio of the magnetic energy density (U_B) to the particle energy density (U_e) (otherwise called magnetic energy dominated) in the emitting region. Shocks are expected to compress the local magnetic field in the emitting region, thereby amplifying the magnetic field strength (e.g., Sironi, Petropoulou and Giannios, 2015). From this, one can infer that in blazars where $U_B/U_e > 1$ in the emitting region, shocks could be the dominant mechanism driving particle acceleration there.

It was also proposed that second-order Fermi acceleration and magnetic reconnection are direct consequences of the turbulent magnetic field in blazar jets (e.g., Marscher, 2016). Theoretical models indicate that a particle-dominated emitting region with low magnetic energy density

where $U_B/U_e < 1$ is consistent with magnetic dissipation in the emitting region of blazar jets and leads to a hard power law in the leptonic spectral slope (e.g., Guo *et al.*, 2014; Sironi, Petropoulou and Giannios, 2015; Zank *et al.*, 2015; Zhang *et al.*, 2015; Lyutikov *et al.*, 2018).

1.5 Aims and objectives

S5 1803+784 and BL Lacertae have unique emission characteristics that suggest inverse Compton scattering of soft photons from outside the gamma-ray emitting region in addition to SSC scattering of synchrotron photons. The two blazars began to flare in 2020, with the average daily fluxes from multiwavelength observations several orders of magnitude higher than previously observed. These two blazars can be used to investigate the emission process and the emitting region structure, particle acceleration, and mechanisms enhancing particle acceleration by studying their observational features in the flaring state. This research investigates the observational characteristics of the two blazars using the phenomenological multiwavelength study of the spectral energy distribution in both the quiescent and the flaring states in the framework of the leptonic jet model using both the synchrotron+SSC-only and the SSC+EC leptonic jet models with the following objectives:

- To collect and organize the multi-wavelength observational data from the NASA/IPAC Extragalactic Database (NED) archive of the selected blazars during the quiescent state and multi-wavelength data from simultaneous observations during the flaring states.
- To use the SED phenomenological characteristics and the light curve temporal characteristics to deduce the high-energy seed photon sources and suggest a possible gamma-ray emission mechanism.
- To fit the SEDs with leptonic models to constrain the physical parameters of the emission region during the blazars' flaring states and provide insight into the mechanism enhancing particle acceleration during the flares.

CHAPTER 2

2.0 The leptonic jet model

Leptonic models assume that emissions from leptons dominate the radiative output over the entire electromagnetic spectrum. The presence of protons is not considered to significantly contribute to the radiative output because the protons are not accelerated to high enough energies.

Synchrotron radiation results from charged particles, such as electrons, spiraling in a magnetic field. The synchrotron photons then undergo inverse-Compton (IC) scattering, where the energetic electrons up-scatter the synchrotron seed photons resulting in high-energy radiation, referred to as synchrotron self-Compton (SSC). When seed photons originate from outside the jet, the inverse Compton scattering process is referred to as external Compton (EC) scattering (Dermer *et al.*, 1992; Sikora, 1994; Rybicki and Lightman, 2004; Finke, 2013; Guo *et al.*, 2014; Cerruti, 2020).

2.1 Synchrotron emission

Cerruti, (2020) describes leptonic radiation processes as follows. The emitting region is assumed to be a sphere of radius *R* filled with relativistic electrons and a tangled homogenous magnetic field strength *B*. The emitting particles move with a bulk Lorentz factor of Γ along the jet and are Doppler beamed by a factor δ. All the equations in this section are considered in the rest-frame of the emitting region, and when the observer frame is referenced, the equation will be stated with a subscript referring to the observer frame as "obs". A particle with electric charge *e* and Lorentz factor $\gamma = E/mc^2$ in the emitting region will radiate a synchrotron power ($P_{syn,\nu}$) per frequency ν (in units of $\mathrm{erg\ s^{-1}Hz^{-1}}$)

$$P_{syn,\nu}(\nu,\gamma,\varphi) = \frac{\sqrt{3}\, e^3 B \sin\varphi}{mc^2}\frac{\nu}{\nu_c}\int_{\frac{\nu}{\nu_c}}^{\infty} dx\, K_{5/3}(x) \qquad 2.1$$

where φ is the pitch angle between the particle momentum and the magnetic field lines, the frequency $\nu_c = \frac{3eB}{4\pi mc^2}\gamma^2 \sin\varphi$, and $K_{5/3}(x)$ is the modified Bessel function of the second kind of order $5/3$ (Ghisellini, 2013; Cerruti, 2020). If the electron energy distribution is isotropic with a power-law with index *n*

$$N_e(\gamma_e) = N_0 {\gamma_e}^{-n} \qquad 2.2$$

where N_0 is the normalization in units of $\mathrm{cm^{-3}}$ and γ_e is the particle Lorentz factor, then the differential photon flux is also a power law with index $(n+1)/2$. Then the flux density will have an index $(n-1)/2$ and $\nu_{obs}F_{\nu_{obs}}$ will have an index of $p = (n-3)/2$. The total

synchrotron emissivity from $N_e(\gamma_e)$ is the integral of the synchrotron power over γ_e and φ

$$j_{syn,\nu}(\nu) = \frac{1}{8\pi} \int_{\gamma_{min}}^{\gamma_{max}} d\,\gamma_e\, N_e(\gamma_e) \int_0^{\pi} d\varphi\, sin\varphi\; P_{syn,\nu}(\nu,\gamma,\varphi) \quad 2.3$$

in units of $\mathrm{erg\,s^{-1}\,cm^{-3}\,Hz^{-1}sr^{-1}}$, where $\gamma_{\min}$ and $\gamma_{\max}$ are the low-energy and high-energy Lorentz factors. The flux ($\nu_{obs}F_{\nu_{obs}}$) in the observer frame is

$$\nu_{obs}F_{\nu_{obs}}(\nu) = \frac{4\pi}{3}\frac{R^3}{d_L^2}\delta^4\nu\, j_{syn,\nu}(\nu) \quad 2.4$$

where d_L is the luminosity distance of the source.

The synchrotron emission at low energies experiences synchrotron self-absorption, whereby the radiated photons are re-absorbed by the electrons themselves. The coefficient of synchrotron self-absorption can be estimated as

$$\mu_{syn}(\nu) = -\frac{1}{16\pi m\nu^2} \int_{\gamma_{min}}^{\gamma_{max}} d\gamma\, \gamma^2 \frac{d}{d\gamma}\left(\frac{N_e(\gamma_e)}{\gamma^2}\right) \int_0^{\pi} d\varphi\, sin\,\varphi\, P_{syn,\nu}(\nu,\gamma,\varphi) \quad 2.5$$

Therefore, the intensity of the synchrotron radiation in the emitting region in the presence of the above coefficient of absorption term is

$$I_{syn,\nu}(\nu) = \frac{j_{syn,\nu}(\nu)}{\mu_{syn}(\nu)}\left\{1 - \frac{2}{\tau(\nu)^2}\left[1 - e^{-\tau(\nu)}(\tau(\nu)+1)\right]\right\} \quad 2.6$$

where $\tau(\nu) = 2R\mu_{syn}(\nu)$. The radiated synchrotron spectrum experiences a change in the power-law index as a result of self-absorption at frequencies below $\nu_{self-abs}$. This implies that the emitting region is optically thick to synchrotron radiation at frequencies below the self-absorbed frequency ($\nu_{self-abs}$).

An electron radiating synchrotron photons will cool (lose energy) after a while; the stationary electron population in the jet can be estimated by computing the self-consistent electron energy distribution at equilibrium

$$\frac{\partial}{\partial t}N_e(\gamma_e,t) = \frac{\partial}{\partial\gamma_e}\left[\gamma_e \frac{N_e(\gamma_e,t)}{\tau_{syn}(\gamma_e)}\right] - \frac{N_e(\gamma_e,t)}{\tau_{cross}} + Q(\gamma_e) \quad 2.7$$

where $Q(\gamma_e)$ is the continuous time-independent injection of electrons and $\tau_{syn}(\gamma_e)$ is the synchrotron cooling time scale, while $\tau_{cross} = R/c$ is the energy-independent adiabatic timescale, also defined as the particle's time to escape or cross the boundary of the emitting region. The synchrotron cooling time scale is

$$\tau_{syn}(\gamma_e) = \frac{3m_e c}{4\sigma_T U_B}\frac{1}{\gamma_e} \quad 2.8$$

where $U_B = B^2/8\pi$ is the magnetic energy density, B is the magnetic field in Gauss (G) and σ_T is the Thomson scattering cross-section, which will be discussed in the subsequent section. The particle distribution at equilibrium can be derived by equating Equation 2.7 to zero, in which case the integral solution will be:

$$N_e(\gamma_e) = e^{-\gamma_b/\gamma_e}\frac{\gamma_b\,\tau_{cross}}{{\gamma_e}^2}\int_{\gamma_e}^{\infty} d\zeta\; Q(\zeta)e^{\gamma_b/\zeta} \quad 2.9$$

where $\gamma_b = \frac{3m_ec^2}{4\sigma_T U_B R}$ is the electron Lorentz factor when $\tau_{syn}(\gamma_e) = \tau_{cross}$ also called the turn-over energy Lorentz factor.

We can then determine a self-consistent synchrotron spectrum. The SED of the emitted photons is a broken power-law distribution. Below the self-absorbed frequency, the spectrum is proportional to $\nu^{7/2}$, while between the self-absorbed frequency and the turn-over frequency (ν_b), the spectrum is proportional to ν^{-p} where p is the low energy spectral slope; here, we may interchangeably use the spectral slope and spectral index. The spectrum above the turn-over frequency (ν_b) is proportional to $\nu^{-p+1/2}$. The characteristic frequencies of the photon spectrum are related to those of the electron spectrum as follows: the minimum frequency $\nu_{min} = \nu_0\gamma_{min}^2$, the turn-over frequency $\nu_b = \nu_0\gamma_b^2$ and the maximum frequency $\nu_{max} = \nu_0\gamma_{max}^2$, where $\nu_0 = 4.2 \times 10^6 B$ Hz, where B is the magnetic field in units of Gauss (G). The electron spectra below and above the turn-over cut-off energy Lorentz factor as measured in blazar observations are often not consistent with the synchrotron self-absorption scenario described above because of stronger turnovers (Cerruti, 2020). For this reason, it is a usual practice to consider the electron spectral indexes and the turn-over cut-off energy Lorentz factor as independent and free parameters in the SED modelling (e.g., Tavecchio *et al.*, 2010). In some cases, observations are consistent with a broken power-law distribution with a spectral turnover of unity (e.g., Tavecchio *et al.*, 2010). Cerruti, (2020) discussed extensively reasons we can observe very strong turnovers or γ-breaks in the SED, including an inadequate understanding of the number/structure of the emitting region(s), the existence of multiple acceleration fronts, a non-homogeneous magnetic field, non-linear cooling terms in the inverse Compton process, or an incomplete cooling process. Strong γ-breaks could also result from using the wrong particle injection model in the SED model.

2.2 Inverse-Compton scattering

Relativistic electrons interacting with low-energy photons otherwise referred to as seed photons or soft photons, and up-scattering them to high energies is known as inverse-Compton scattering. Inverse-Compton scattering is the reverse of the Compton scattering process whereby an energetic photon scatters an electron at rest. The inverse-Compton process is a very efficient mechanism to produce X-ray and gamma-ray photons in astrophysical sources.

Inverse-Compton scattering in most astrophysical sources is either in the Thomson or Klein-

Nishina (K-N) regime (e.g., Uzdensky, 2016; Cerruti, 2020). In the Thomson regime, the energy of the soft photons in the electron rest frame is lower than the electron rest frame energy ($m_e c^2$), while in the K-N regime it is higher. All the discussions following here are in the rest frame of the electron. Assuming a photon of energy $\varepsilon = h\nu/m_e c^2$, let the energy before scattering and after scattering be represented as ε_1 and ε_2 respectively. Then $\varepsilon_1 = h\nu_1/m_e c^2$ with electron Lorentz factor $\gamma_{e1} = E_1/m_e c^2$ and $\varepsilon_2 = h\nu_2/m_e c^2$ with electron Lorentz factor $\gamma_{e2} = E_2/m_e c^2$, where $E_1/m_e c^2 = 1$. Through energy and momentum conservation equations, it can be shown that in the electron rest frame

$$\varepsilon_2 = \frac{\varepsilon_1}{1+\varepsilon_1(1-\cos\xi)} \tag{2.10}$$

where ξ is the angle between the incoming and the scattered directions of the photons. Let the two equations describing the change from the rest frame of reference to the observer frame be represented as:

$$\varepsilon_1 = {\varepsilon_1}^{\mathrm{obs}}\gamma_e\left(1 - \frac{\mathrm{v_e}}{\mathrm{c}}\cos{\vartheta_1}^{\mathrm{obs}}\right) \tag{2.11}$$

$${\varepsilon_2}^{\mathrm{obs}} = \varepsilon_2\gamma_e\left(1 - \frac{\mathrm{v_e}}{\mathrm{c}}\cos\vartheta_2\right) \tag{2.12}$$

where ${\vartheta_1}^{obs}$is the angle between the electron and the incoming photon in the observer's reference frame, and ϑ_2 the angle of the scattered photon in the electron's rest frame with $\beta_e = \frac{v_e}{c}$. In the Thomson regime, where $h\nu_1 \ll m_e c^2$ we have

$${\varepsilon_2}^{obs} = \varepsilon_1\gamma_e(1+\beta_e\cos\vartheta_2) \cong {\varepsilon_1}^{obs}\gamma_e^2\left(1+\beta_e\cos{\vartheta_1}^{obs}\right)\varepsilon_1\gamma_e(1+\beta_e\cos\vartheta_2) \tag{2.13}$$

In the Thomson regime, the inverse-Compton cross-section is equal to $\sigma_T = \frac{8\pi}{3}r_0^2$ and r_0 is the classical electron radius. Klein and Nishina calculated the general cross-section in 1928, known as the Klein-Nishina expression

$$\sigma_{KN}(\varepsilon_1) = \frac{3}{4}\sigma_T\left[\frac{1+\varepsilon_1}{\varepsilon_1^2}\left(\frac{2(1+\varepsilon_1)}{1+2\varepsilon_1} - \frac{ln(1+2\varepsilon_1)}{\varepsilon_1}\right) + \frac{ln(1+2\varepsilon_1)}{2\varepsilon} - \frac{1+3\varepsilon_1}{(1+2\varepsilon_1)^2}\right] \tag{2.14}$$

In the Klein-Nishina regime ($\varepsilon_1 \gg 1$) the inverse-Compton cross-section drops steadily, and the approximate cross-section is

$$\sigma_{KN}(\varepsilon_1 \gg 1) \approx \frac{3}{8}\sigma_T\frac{ln2\varepsilon_1 + 1/2}{\varepsilon_1} \tag{2.15}$$

Because it is computationally taxing to calculate the inverse-Compton emissivity analytically, it is better solved numerically by performing an integration over the electron and photon distributions times the cross-section. In the case of isotropic distributions of both electrons and photons, the inverse-Compton emissivity is

$$j_{iC}(\nu) = \frac{h^2\nu}{4\pi m_e c^2} \int d\varepsilon\, N_{ph}(\varepsilon) \int d\gamma\; N_e(\gamma_e)\, C(\varepsilon, \gamma_e, \nu) \quad 2.16$$

where the last term on the right, $C(\varepsilon, \gamma_e, \nu)$ is referred to as the Jones' Compton kernel (Cerruti, 2020). The observed inverse-Compton flux ($\nu_{obs}F_{\nu_{obs}}$) is

$$\nu_{obs}F_{\nu_{obs}}(\nu) = \frac{4\pi}{3}\frac{R^3 {\varepsilon_2}^{obs}(1+z)}{d_L^2}\, j_{iC}(\nu). \quad 2.17$$

Like the synchrotron radiation, the self-consistent electron distribution at equilibrium also experiences losses due to inverse-Compton cooling. A combined inverse-Compton and synchrotron cooling time scale is

$$\tau_{cooling}(\gamma_e) = \frac{3mc}{4\sigma_T(U_B + U_{ph})}\frac{1}{\gamma_e}, \quad 2.18$$

where U_{ph} is the radiation energy density of the photon field. The effect of the cooling timescale on the electron distribution is again a broken power-law with index *n* below and *n*+1 above the turn-over energy Lorentz factor in the Thomson regime. This is the case in the K-N regime only if the inverse-Compton losses dominate over the synchrotron losses at high energies resulting in the steady-state electron distribution hardening at the highest energies. The following details of the leptonic model used for this thesis and implemented with the *JetSeT* code will further be discussed in Chapter 3, Section 3.7.

2.2.1 Synchrotron self-Compton scattering

The up-scattering of the synchrotron radiation through inverse-Compton scattering to higher energies by the same population of electrons responsible for the synchrotron radiation is called synchrotron self-Compton (SSC). It is an efficient means of transferring particle energy into a photon radiation field. In a single-zone homogeneous emitting region, SSC is responsible for most of the high-energy SED components in blazars. In some cases, a single-zone SSC model can describe the SEDs of HSP while failing to reproduce the SEDs in the LSP blazars and FSRQs (e.g., Ghisellini, 1996, 2013).

2.2.2 External inverse-Compton scattering

In the black hole environment, various sources of low-energy photons can be up-scattered to gamma-rays. The external photon field depends on the location of the emitting region and the nature of the external field. Sources of external seed photons include re-emitted disk photons by the BLR, the DT and sometimes from the cosmic microwave background (CMB) radiation. In the case of the blazar SED modeling in this work, I focus on the thermally radiated photons

from the accretion disk that are absorbed and re-emitted by either the BLR as UV/optical photons or the DT as infrared photons (e.g., Tavecchio and Ghisellini, 2008; Sikora *et al.*, 2009; Finke, 2016).

In this section, I will briefly discuss the treatment of the inverse-Compton scattering in an isotropic photon field based on earlier work (e.g., Blumenthal and Gould, 1970; Khangulyan, Aharonian and Kelner, 2014).

If we assume an isotropic photon field with black body radiation, then the number density distribution is

$$N_{ph}(\varepsilon) = [\pi^2(\hbar c)^3]^{-1}\left[\varepsilon^2/\left(e^{\varepsilon/K_BT}-1\right)\right] \quad 2.19$$

where $\hbar = h/2\pi$ is Planck's constant, K_B is the Boltzmann's constant, and T is the temperature.

The general form of the spectrum of the up-scattered photons per electron in the observer frame is

$$\frac{dN_{\gamma_e,\varepsilon}}{dtdE_1} = \frac{2\pi r_0^2 m_e c^3}{\gamma_e}\frac{N_{ph}(\varepsilon)\,d\,\varepsilon}{\varepsilon} \times \left[2q\ln q + (1+2q)(1-q) + \frac{1}{2}\frac{(\Gamma_\varepsilon\, q)}{1+\Gamma_\varepsilon q}(1-q)\right] \quad 2.20$$

where Γ_ε is a dimensionless parameter defined as $\Gamma_\varepsilon = 4\varepsilon\gamma_e/m_ec^2$, $q = E_1/\Gamma_\varepsilon(1-E_1)$, and r_0 is the classical electron radius.

If the energy of the up-scattered photons ${\varepsilon_2}^{obs} = \gamma_e m_e c^2 E_1$ in the units of the initial electron energy (electron energy before scattering), then the total inverse-Compton spectrum of the up-scattered photons is

$$dN_{tot}/dtd{\varepsilon_2}^{obs} = \iint N_e(\gamma_e)\,d\gamma_e\,\left(dN_{\gamma_e,\varepsilon}/dtd{\varepsilon_2}^{obs}\right), \quad 2.21$$

where the last term is given in Equation 2.20.

For the case of power-law electron energy distribution

$N_e(\gamma_e) = N_0{\gamma_e}^{-p},\ \gamma_0 < \gamma_e < \gamma_{max}$, where γ_0 is the lowest cut-off energy Lorentz factor of the electron distribution, Equation 2.20 can be approximated in the Thomson limit as

$$\frac{dN_{\gamma_e,\varepsilon}}{dtd{\varepsilon_2}^{obs}} = \frac{\pi r_0^2 c}{2{\gamma_e}^4}\frac{N_{ph}(\varepsilon)\,d\,\varepsilon}{\varepsilon^2}\left(2{\varepsilon_2}^{obs} ln\frac{{\varepsilon_2}^{obs}}{4{\gamma_e}^2\varepsilon} + {\varepsilon_2}^{obs} + 4{\gamma_e}^2\varepsilon - \frac{\left({\varepsilon_2}^{obs}\right)^2}{2{\gamma_e}^2\varepsilon}\right) \quad 2.22$$

In the Thomson limit, the lower limit of the cut-off Lorentz factor (γ_{min}) in the integration of Equation 2.21 over γ_e will be

$$\gamma_{min} = max\left[\frac{1}{2}({\varepsilon_2}^{obs}/\varepsilon)^{1/2}, \gamma_0\right] \quad 2.23$$

Assuming the photons have energies such that $\frac{1}{2}({\varepsilon_2}^{obs}/\varepsilon)^{1/2} > \gamma_0$ and $\frac{1}{2}({\varepsilon_2}^{obs}/\varepsilon)^{1/2} \ll \gamma_{max}$, the total inverse-Compton spectrum of the up-scattered photons in the Thomson regime is a power-law in ${\varepsilon_2}^{obs}$ (Blumenthal and Gould, 1970)

$$F_{\nu_{obs}} = (2^{p+3})\pi r_0^2 c\, N_0 \frac{p^2+4p+11}{(p+3)^2(p+1)(p+5)}\,({\varepsilon_2}^{obs})^{-(p+1)/2}\int \varepsilon^{(p-1)/2}\,N_{ph}(\varepsilon)\,d\,\varepsilon. \quad 2.24$$

As stated above, in this work, the external radiation field (soft photons) undergoing inverse-Compton scattering comes from either the BLR or the DT and is treated as an isotropic black body radiation field (e.g., Finke, 2016).

For an isotropic soft photon field from the BLR or the DT with energy density $u_{\rm ph}$ and low-energy cut-off Lorentz factor $\gamma_{min} < \gamma$, the observed inverse-Compton flux ($\nu_{obs}F_{\nu_{obs}}$) can be solved numerically using a delta-function approximation as derived in Finke, (2016)

$$\nu_{obs}F_{\nu_{obs}} = \frac{c\sigma_T\delta^3{\varepsilon_2}^{obs}(1+z)}{32\pi d_L^2}\frac{u_{\rm ph}}{{\varepsilon_1}^3} \times \frac{N_e(\gamma/\delta)}{\gamma} M_3(\varepsilon_1), \quad 2.25$$

where $M_3(\varepsilon_1)$ asymptotically approaches

$M_3(\varepsilon_1) \rightarrow \frac{1}{2}\left(\frac{{\varepsilon_1}^2}{3} - \frac{2{\varepsilon_1}^3}{9} + \frac{13{\varepsilon_1}^4}{60} - \frac{133{\varepsilon_1}^5}{600}\right)$ for $\varepsilon_1 \ll 1$ in the Thomson regime,

and $M_3(\varepsilon_1) \rightarrow \frac{\varepsilon_1}{2}\left(ln(\varepsilon_1) - \frac{1}{2}\right) + 3.114\, ln(\varepsilon_1) - \left[ln\left(\frac{\varepsilon_1}{2}\right)\right]^2 - 6.559 + \frac{2}{\varepsilon_1}(2\, ln(\varepsilon_1) + 3.249)$

for $\varepsilon_1 \gg 1$ in the Klein-Nishina regime. In the Thomson regime, Equation 2.25 is reduced to

$$\nu_{obs}F_{\nu_{obs}} \rightarrow \frac{c\sigma_T\delta^3}{6\pi d_L^2}\left(\frac{{\varepsilon_2}^{obs}(1+z)}{2\varepsilon_1}\right)^{3/2} \times N_e({\varepsilon_2}^{obs}/\varepsilon_1). \quad 2.26$$

Equation 2.26 is the numerical solution of the inverse-Compton flux of up-scattered soft photons external to the jet in the observer reference frame.

2.3 Observational tools in blazar studies

The advent of highly sophisticated space-based telescope systems and networks that enhanced the capability of ground-based telescopes has opened the era of multiwavelength and multi-messenger observations in astronomy and astrophysics. Observational tools discussed below have helped to open the vista of knowledge that forms the basis of our understanding of active galactic nuclei, especially that of blazars.

2.3.1 Multiwavelength observations

Blazars shine in all bands of the electromagnetic spectrum. Coordinated multiwavelength observations have been a critical tool for blazar studies. In the 1990s, with the launch of the Compton Gamma-ray Observatory and Rossi X-ray Timing Explorer telescopes, the first multiwavelength campaigns, including X-ray and gamma-ray observations, were organized (Hartman *et al.,* 2001). They typically consisted of quasi-simultaneous data from radio, near-IR, optical, X-rays, and γ-rays with a duration of weeks to months. These observations revealed that in many sources, the spectral energy distribution (νF_ν) of blazars was found to be strongly Compton-dominated (e.g., Abdo *et al.*, 2010). The ability of the *Fermi*-LAT γ-ray telescope to

detect gamma-ray sources revolutionized our understanding of AGN and the gamma-ray view of the Universe. The 4FGL catalog of *Fermi*-LAT has more than 5000 detected point sources (Abdollahi *et al.,* 2020) that offer a robust database for blazar study. The current generation Imaging Air Cherenkov Telescopes (IACTs), such as the High Energy Stereoscopic System (H.E.S.S), detect cosmic γ-rays in the energy range from GeV to TeV energy bands. The Major Atmospheric Gamma Imaging Cherenkov (MAGIC), the Very Energetic Radiation Imaging Telescope Array System (VERITAS) and the High-Altitude Water Cheronkov Gamma-ray (HAWC) observatories have increased the number of detected blazars in the VHE regime significantly. The upcoming Cherenkov Telescope Array (CTA) will complement the existing telescopes in the VHE regime (e.g., IceCube Collaboration *et al.*, 2018; Hovatta and Lindfors, 2019; Falanga *et al.*, 2021; Prince, Khatoon and Agarwal, 2021; Rajput and Pandey, 2021).

2.3.1.1 Spectral energy distributions

Multiwavelength spectral energy distributions (SEDs) have been useful for blazar studies since the early days of gamma-ray observations (Abdo *et al.,* 2010). Extensive multiwavelength campaigns have been organized to collect simultaneous data from radio to gamma-ray bands since the Compton Gamma-ray Observatory (CGRO) (Hartman *et al.,* 2001). Since the launch of *Fermi*-LAT, the SEDs of some bright blazars have been persistently studied using telescopes at all wavelengths including Mrk 421 and Mrk 501 (Abdo *et al.,* 2011). Time-resolved and self-consistent SEDs have recently provided insight into blazar acceleration and emission mechanisms (e.g., Lucchini *et al.,* 2019).

The single-zone SSC model has been able to explain the observed SED in high synchrotron peak (HSP) BL Lacs. In the model, if synchrotron photons are the main source of low-energy radiation, then, due to pair-production opacity, the emitting zone in such a model depends on its size and Doppler factor, and on the density of lower-energy photons (Abeysekara *et al.*, 2018). Otherwise, if an external photon field dominates the low-energy radiation, there will be substantial γ-γ absorption, requiring the emitting region to be far away from the black hole or beyond the broad-line region (BLR) to account for the gamma-ray observations.

2.3.1.2 Intra-day and long-term light curves

The observation of minutes-scale variability from Mrk 501, Mrk 421, and PKS 2155-304 (Gaidos *et al.*, 1996; Aharonian *et al.*, 2006; Singh *et al.*, 2017) have put a tight constraint on

the size and nature of the emitting region. The short variability time scale supports the idea of magnetic dissipation as a viable alternative particle acceleration mechanism to shocks between colliding blobs in the jet (Böttcher, 2019). *Fermi*-LAT has already collected more than 12 years of data. Combined with existing radio and optical data provides an extensive data set to study polarization and long-term variability. There have been many monitoring programs; for example, the Owens Valley Radio Observatory (OVRO) 40-m monitoring program obtained 15 GHz light curves of nearly 2000 sources since 2008 (Richards *et al*., 2011), the MOJAVE observatory (Monitoring of Jets in Active Galactic Nuclei with VLBA Experiment) (Homan *et al.*, 2009; Lister *et al.*, 2009) and the Tracking Active Galactic Nuclei with Austral Milliarcsecond Interferometry[1](TANAMI). All have supported the *Fermi*-LAT mission in understanding the cross-correlation between the radio and the gamma-ray emission in blazars (Max-Moerbeck *et al.*, 2014).

2.3.2 Very long baseline interferometry (VLBI)

Radio and millimeter wavelengths provide the only means yet to spatially resolve the jets of blazars (Thompson, Moran and Swenson, 2017). To spatially resolve the emission in the blazar zone on parsec scales, corresponding to an angular resolution of milliarcseconds, very long baseline interferometry (VLBI) is required. In the VLBI approach, radio telescopes worldwide simultaneously observe the same targets, forming an interferometer with an angular resolution determined by the distance between the telescopes and the observing frequency. Angular resolutions ranging from tens of micro-arcseconds to milliarcseconds can be achieved using this method (Hovatta and Lindfors, 2019).

2.3.3 Multi-messenger observations

The discovery of ultra-high-energy neutrinos in 2013 by the IceCube neutrino observatory ushered in fully the era of multi-messenger astrophysical study (Aartsen *et al.*, 2013). Although the origin of the detected neutrinos is still debated, the detection of high-energy neutrino IC-170922A with good angular resolution coincides with the flaring blazar TXS 0506+056 (Aartsen *et al.*, 2018; IceCube Collaboration *et al.,* 2018). The suggestion that blazars could be the source of ultra-high-energy neutrinos has triggered a renewed interest in the hadronic emission model of blazars. Since supermassive black holes are thought to be the driver of active galactic nuclei, blazars could also be an interesting source of gravitational wave study

[1] Pulsar.sternwarte.uni-erlangen.de/tanami/

with a space-based laser interferometer (Sillanpaa *et al.*, 1988; Hovatta and Lindfors, 2019).

2.4 Magnetic energy dissipation through reconnecting field lines

The minute scale variability observed in some blazars is often tricky to explain in terms of shock acceleration. This short variability time scale makes particle acceleration through magnetic energy dissipation in the reconnecting magnetic field lines a viable alternative to the shock acceleration model. Magnetic reconnection is a rapid rearrangement of magnetic field lines corresponding to a change in the topology of the magnetic field. It is a fundamental process in plasma that allows magnetic energy to be converted to plasma kinetic energy (Zenitani and Hoshino, 2007; Guo *et al.*, 2014; Lyutikov *et al.*, 2018; Werner, Philippov and Uzdensky, 2019). According to Uzdensky (2016), magnetic reconnection is responsible for flares and bursts of high-energy radiation observed in the Universe. However, how this process evolves and unfolds in astrophysical plasma is still under intense scrutiny. Radiative reconnection is a reconnection process in which radiation "back reaction" affects the reconnection dynamics, energetics, and particle acceleration (Uzdensky, 2016).

The properties of the emitting region are related to the bulk motion of the jet in a way that could provide a diagnostic view of the dissipative process. In shocks, the magnetic field is compressed, and its strength is thus increased: the magnetic energy per particle is larger in the emitting region than in the bulk of the jet. In contrast to shocks, magnetic reconnection dissipates magnetic energy; therefore, the emitting blob is less magnetized than the bulk of the jet upstream. The more efficient magnetic reconnection is in accelerating particles, the more particle-dominated the emitting region becomes (Sironi, Petropoulou and Giannios, 2015). The ratio of the magnetic energy density ($\mathrm{U_B}$) to the particle energy density ($\mathrm{U_e}$) in the emitting region of the blazars using the model discussed in this thesis is used to study the consistency of each flare with magnetic dissipation in the emitting region. The choice of whether the magnetic dissipation through reconnecting magnetic field lines or shock acceleration is the mechanism driving particle acceleration in the downstream emitting region is often related to the energy densities ratio $\mathrm{U}_B/\mathrm{U}_e$, where a ratio less than one ($\mathrm{U}_B/\mathrm{U}_e < 1$) signifies a particle-dominated emitting region consistent with magnetic dissipation, while a ratio greater than one ($\mathrm{U}_B/\mathrm{U}_e > 1$) is consistent with a magnetic-dominated emitting region where shocks are the most likely driver of particle acceleration (Sironi, Petropoulou and Giannios, 2015).

2.5 The photon seed factor

The photon seed factor (PSF), calculated from observational parameters of the broadband SED, is used to predict the source(s) of the seed photons of the external inverse Compton scattering in individual blazar jets (Harvey, Georganopoulos and Meyer, 2020). It is derived based on the assumption that the external Compton process is involved in the high energy emission process. Each up-scattered photon population has a unique value.

The PSF is defined as

$$\mathrm{PSF} = \log_{10}\left[3.22 \times 10^{4}\left(k_1^{1/2}\nu_{\mathrm{sync},13}/\nu_{\mathrm{IC},22}\right)\right], \quad 2.27$$

where k_1 is the ratio of the inverse Compton peak luminosity to the synchrotron peak luminosity, $\nu_{\mathrm{sync},13}$ is the peak frequency of the synchrotron peak in units of 10^{13}Hz, and $\nu_{\mathrm{IC},22}$ is the peak frequency of the inverse Compton component in units of 10^{22}Hz.

It is possible to compare the PSF of a blazar with that of the broad line region (BLR) and the dusty torus (DT) since both the BLR and DT are considered to have constant energy density across all sources (Ghisellini and Tavecchio, 2009; Kishimoto *et al.*, 2011). The expected seed factor for the BLR and the DT torus is estimated to be $\mathrm{PSF_{BLR}} = 3.29 \pm 0.11$ and $\mathrm{PSF_{DT}} = 3.92 \pm 0.11$ respectively (Harvey, Georganopoulos and Meyer, 2020).

Predicting the source population using the photon seed factor is only valid in a statistical sense and should not be used to determine the source of the seed photons for a single blazar, even though it uses observational features such as the peak fluxes, peak frequencies and peak luminosities of both the synchrotron and the inverse-Compton components of the SED. In this work, the seed photon populations predicted by the PSF in Equation 2.27 (BLR or DT) were combined with other observational features and compared with the result of the SED model. I will discuss this further in Chapter 4, Section 4.4.

2.6 Blazar phenomenological (sequence) trends

Observed phenomenological trends of the blazar emission tend to distinguish FSRQs from the BL Lacs as first suggested by Fossati et al. (1998)and discussed in detail by e.g., Ghisellini and Tavecchio, 2009; Ghisellini *et al.*, 2010; Abdo *et al.*, 2010; and Cha *et al.*, 2014. Some of these parameters, such as synchrotron peak luminosity, inverse Compton peak luminosity, and peak frequencies, have unique characteristics that form the blazar divide. However, some of these blazar sequences had been claimed to be due to observational bias, for example, by Giommi, Padovani and Polenta, (2013). At the same time, Meyer *et al.* (2011) suggested that instead of the blazar sequence, blazar subclasses are formed due to misalignment of the Fanaroff-Riley I

(FRI) and FRII radio galaxies in what they described as an envelope scenario. It was observed that LSP sources have a very broad second peak of the SED and do not follow these trends expected from the blazar sequence and the envelope scenarios (Hovatta and Lindfors, 2019). With the availability of more robust multiwavelength data, some of the divides are becoming blurred; for example, the discovery of both a broad hydrogen line (Hα) and the sub-hour variability in the VHE emission in BL Lacertae has extensively strained the standard model of the blazar sequence (e.g., Corbett *et al.,* 2006; Acciari *et al.,* 2019).

2.7 Examples of previous studies of BL Lacetae and S5 1803+784

The two blazars studied in this work are S5 1803+784, with coordinates Right Ascension (J2000) = 270.1891° and Declination (J2000) = + 78.4678° and redshift z = 0.684 (Gattano, Lambert and Le Bail, 2018), and BL Lacertae with coordinates R.A = 330. 68° and Declination = + 42.2778° and redshift z = 0.0686 (Miller and Hawley, 1977) (see Table 2.1). They are important for blazar studies due to their unique characteristics and flux variability. Several recent observations have been carried out on them, and various suggestions and models have been used to explain their emission characteristics. For example, BL Lacertae has been studied by several authors using both observations and numerical simulations due to its very short flux variability time scale (e.g., Ravasio *et al.*, 2002; Raiteri *et al.*, 2009; Acciari *et al.*, 2019; Morris *et al.*, 2019).

The SED of BL Lacertae was fitted with a single-zone homogenous SSC model; however, it was noted that modelling the high energy portion of the spectrum required external seed photons for the inverse Compton scattering (Ghisellini and Tavecchio, 2009; Ravasio *et al.*, 2002) and ever since, the SED of BL Lacertae has been consistently modelled with external seed photons for the inverse Compton process (Böttcher *et al.*, 2013).

Different leptonic jet models have been used to explain the observed emission from BL Lacertae, the prototype BL Lac object. For example, Raiteri et al. (2009) used the Whole Earth Blazar Telescope (WEBT) and the XMM-Newton satellite between July and December 2007 and January 2008 to study the emission properties of BL Lacertae in the optical to X-ray energy range. Their simultaneous radio-to-X-ray SED suggested a synchrotron peak in the near-infrared band with a significant UV excess besides a slight soft-X-ray excess. In their work, they ascribe the UV excess to accretion disk thermal emission and the other broadband features to the presence of two synchrotron components with the corresponding SSC emission. Their SED model returned a disk temperature $\geq$ 20000K and a luminosity $\geq 6 \times 10^{44} \mathrm{erg\ s^{-1}}$.

A single-zone SSC model was recently used to fit the VERITAS observed fast flare of 2016 from BL Lacertae through the numerical simulation of a time-evolving reconnecting plasmoid whose radius and velocity evolve as it travels through the reconnection layer. The model can reproduce the light curve but over-produce the synchrotron part of the SED significantly (Morris *et al.*, 2019). Due to the complexity of the BL Lacertae emission, a two-zone emitting region model and star interaction model were proposed in which the HE portion originates from the VLBI observed 43 GHz radio core and the VHE emission with a very fast variability time scale from a very small component in the jet structure, as well as a third scenario in which a star interacts with the jet. To avoid significant γ-γ absorption, the VHE gamma-ray emission region must be located near the outer boundary of the BLR or beyond it. The BLR in BL Lacertae is assumed to be too weak to absorb the VHE gamma-rays, but can provide additional seed photons to the inverse Compton scattering (Acciari *et al.*, 2019). The three models in Acciari *et al*. (2019) can all reproduce the observed SED during the flare of June 15, 2015, though with some caveats. Therefore, settling on a preferred model for their results is difficult. In the recent multiwavelength analysis of Nesci et al. (2021), the multiwavelength light curves of S5 1803+784 over a long period from August 2008 until December 2018 were studied to check for cross-correlation between radio, optical, and gamma-ray wavebands, including X-ray data obtained from *Swift* during the 2015 flare of S5 1803+784. Their results showed no clear correlation between the radio and gamma-ray light curves and detected no periodicity in the optical and the gamma-ray light curves. The optical spectral index of S5 1803+784 was constant in the period studied. The X-ray and the gamma-ray showed no significant spectral variations, even in the period of higher fluxes. They concluded that the absence of spectral evolution in S5 1803+784 could mean that the location of the gamma-ray emitting region in the flaring state is beyond the broad line region. Previously Nesci et al. (2002) reported six years of observations of S5 1803+784 in optical (BVRI) and radio (8.4 GHz) and found no correlation between the radio and the optical wavebands studied. Recently, Priya et al. (2022) reported a multiwavelength analysis of S5 1803+784; they did not use simultaneous X-ray data as has been done here for the flare period corresponding to the flare analyzed in this work.

Table 2.1: List of blazars studied and their characteristics.

4FGL catalog name	Associated name	Redshift	Types	Coordinates
4FGL J2202.7+4216	BL Lacertae	0.0686	LSP (BL Lac)	RA: 330.68°
				DEC: 42.28°
4FGL J1800.6+7828	S5 1803+784	0.684	LSP (BL Lac)	RA: 270.19°
				DEC: 78.47°

CHAPTER 3

3.0 Blazar observations, analysis methods, and SED modelling

Multiwavelength flaring activity was observed in S5 1803+784 from MJD 58942-589318 (Venters, Angioni and Ojha, 2020) (4FGL J1800.6+7828 in the *Fermi*-LAT 4FGL catalog (Abdollahi *et al.*, 2020)) and in BL Lacertae (4FGL J2202.7+4216 in the *Fermi*-LAT 4FGL catalog (Abdollahi *et al.*, 2020)) from MJD 59124-MJD 59435 (Cheung, 2020; Mereu, 2020). Altogether, 13 flares (Table 3.1 and Figure 3.2) from 2020 and 2021 were used for this study. The average flux states shown in Table 3.2 are taken from the 4FGL-DR2 catalog

3.1 Observation of blazar jets with the *Fermi* Large Area Telescope

Fermi-LAT has allowed several authors and researchers to access robust high-energy data across gamma-ray energies to study relativistic jets and AGN. The availability of over 12 years of observational data from the *Fermi* space telescope has made studying high-energy point sources relatively easy. The variability, time-resolved spectral energy distributions, and luminosity of blazar jets have been explored in unprecedented detail towards a good understanding of the extragalactic sources of highly energetic photons directed to our line of sight, from the most luminous long-lived objects in the Universe, the active galactic nuclei (AGN) (e.g., Abdo *et al.*, 2010; Abdo *et al.*, 2011; Saito *et al.*, 2013; Ackermann *et al.*, 2016; Marscher, 2016).

3.1.1 *Fermi* Large Area Telescope

The Large Area Telescope (*Fermi*-LAT) is the main instrument onboard the Fermi Gamma-ray Space Telescope. *Fermi*-LAT is an imaging, wide field-of-view, high-energy gamma-ray telescope, covering the energy range from below 20 MeV to more than 300 GeV (Atwood *et al.*, 2009). *Fermi*-LAT has a low-earth orbit with a period of about 95 minutes. Its normal mode of operation is to keep its orientation with the instruments facing away from earth. A rocking motion allows for equal sky coverage with the field of view (fov) of the instruments sweeping across most of the sky approximately 16 times per day since LAT has a 70° half angle fov which provides 30 minutes of on-time on each point in the sky every two orbits.

3.1.2 *Fermi*-LAT data analysis

The *Fermi*-LAT data and analysis software are available publicly as LAT photons files and spacecraft files at http://fermi.gsfc.nasa.gov/cgi-bin/ssc/LAT/LATDataQuery.cgi and analysis

software at: http://fermi.gsfc.nasa.gov/ssc/data/analysis/software/.

The *Fermi*-LAT data analysis in this thesis was performed using *Fermi* Science tools version 1.2.23 and Fermipy version 0.20, a python package that facilitates the analysis of LAT data. The Fermipy package (https://fermipy.readthedocs.io/en/latest/) is built on the pyLikelihood interface of the *Fermi* Science Tools. Fermipy provides a set of high-level tools for performing standard analysis tasks (Wood *et al*., 2017), such as:

- Data and model preparation with `gtselect`, `gtmktime`, etc.
- Extracting a spectral energy distribution (SED) of a source.
- Finding new source candidates.
- Localizing a source or fitting its spatial extension.

3.1.3 *Fermi*-LAT analysis procedure

The gamma-ray data S5 1803+784 and BL Lacertae (Abdollahi *et al.*, 2020) were analyzed using the reprocessed Pass 8 data sets with P8R3_SOURCE_V2 instrument response functions following the standard procedures (Atwood *et al.*, 2009, 2013; Abdo *et al.*, 2010, Atwood *et al.*, 2013) implemented in the *Fermi* ScienceTools (ver. 1.2.23) software package using Fermipy (0.20.0) analysis (Wood *et al.*, 2017). Only SOURCE class events (event class = 128 and event type = 3) within a circular region of interest (ROI) of 10° radius centered at the position of the blazars with good time intervals selected using "(DATA_QUAL > 0) && (LAT_CONFIG==1)" and maximum zenith angle ≥ 90° were selected for the analysis to reduce the contamination from the Earth limb gamma-ray. We have included all 4FGL-DR2 (fourth *Fermi*-LAT 10-year source catalog) `gll_psc_v26.xml` point sources within 15° from the ROI center, Galactic diffuse model `gll_iem_v07` and extragalactic isotropic emission templates (`iso_P8R3_SOURCE_V2_v1.txt`) in the source model file for the background subtraction. The spectral shape of all the sources in the model file within 3° and the associated spectral parameters have been kept free to vary during the analysis. The target sources are modelled using a log parabola spectral shape. The statistical significance of the HE γ-ray signal in the energy range 0.1-300 GeV is determined from the maximum likelihood ratio test statistic (TS) (Mattox *et al.*, 1996) using the following energy bins in MeV: (100-316.23), (316.23-1000), (1000-3162.28), (3162.28-10000), (10000-31622.78), (31622.78-100000) and (100000-316227.77). Energy bins with TS ≥ 9 (Abdollahi *et al.*, 2020) were used to build the SEDs.

3.1.4 *Fermi*-LAT Gamma-ray emission spectra

The gamma-ray spectra were analyzed following the standard procedure in Fermipy. The SEDs were fitted with three spectral models, namely the power law (PL) (Equation 3.3), the broken power law (BPL) (Equation 3.4), and the log parabola (LP) (Equation 3.5).

$$\frac{dN}{dE} = N_0(E/E_b)^{-k} \quad 3.3$$

$$\frac{dN}{dE} = \begin{cases} N_0(E/E_b)^{-\alpha_1}, & E < E_b \\ N_0(E/E_b)^{-\alpha_2}, & E \geq E_b \end{cases} \quad 3.4$$

The photon index is represented as k in the PL, while for the BPL, the two photon indices are α_1 and α_2. The gamma-ray SEDs of the blazars are well represented by the log parabola spectral distribution (Chapters 5 and 6) given in Equation 3.5 (Nolan *et al.*, 2012), with better statistics justifying the extra parameter.

$$\frac{dN}{dE} = N_0(E/E_b)^{-\alpha-\beta\log(E/E_b)}, \quad 3.5$$

where N_0 is the normalization constant (the pre-factor) shortened as 'norm' in this work, α is the photon index at energy E_b (scaling factor) and β is the spectral curvature.

3.2 Flare definition and description

Nalewajko, (2013) defines a flare as a continuous period associated with a given flux peak, during which the flux exceeds half the peak value, where the lower limit is attained twice, once at the beginning and once at the end of the flare. We adopt this definition and use Bayesian blocks[2] (Figure 3.2) analysis to define the flare intervals (Scargle *et al.*, 2013). The Bayesian blocks implementation provides an objective way to detect significant variations in the light curve (Meyer, Scargle and Blandford, 2019).

The flare period (Figure 3.2 and Table 3.1) was further identified using the description of Meyer *et al.,* (2019) that starting with a block higher than the previous and the subsequent blocks, the flare period proceeds downward from the peak in both directions.

Both blazars recorded the highest daily fluxes observed by *Fermi*-LAT during this period (Figure 3.1).

[2] https://github.com/tburnett

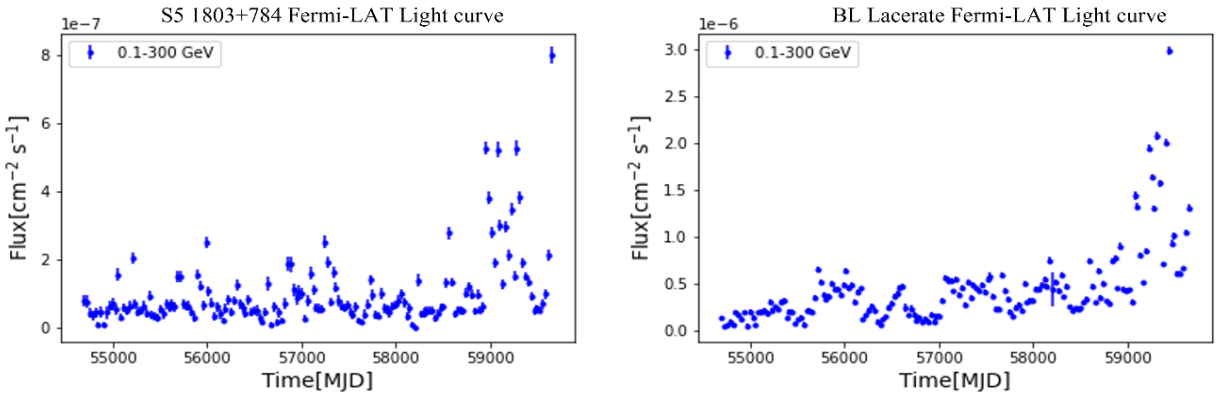


Figure 3.1: (Left panel) The 30-day binned *Fermi*-LAT light curve of S5 1803+784. (Right panel) The 30-day binned *Fermi*-LAT light curve of BL Lacertae. The light curves are from 2008-08-04 to 2022-03-30 (MJD 54682-MJD 59668).

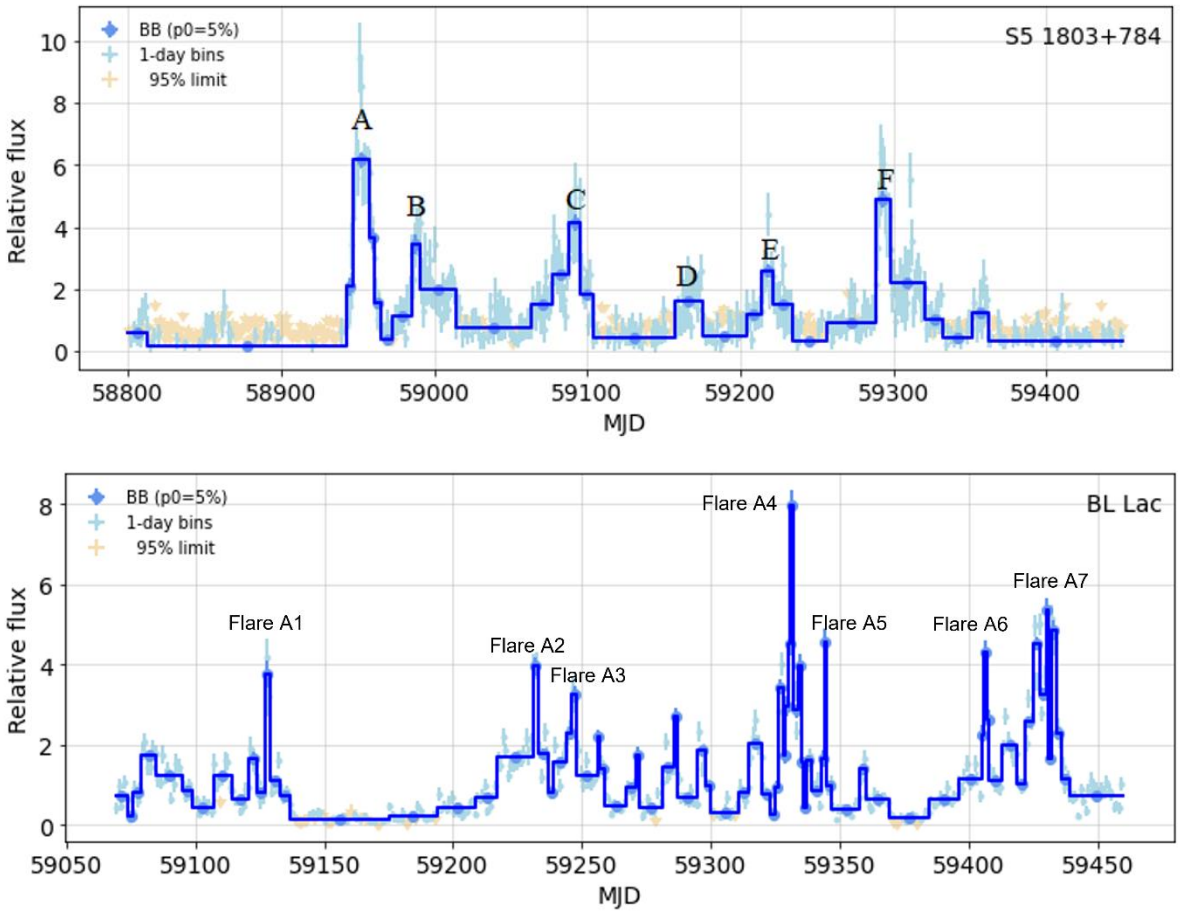


Figure 3.2: (Upper panel) The Bayesian blocks of S5 1803+784. (Lower panel) The Bayesian blocks of BL Lacertae. Note: The nomenclature was chosen to avoid confusion between the flares from the two sources.

Table 3.1: (a) The flaring period of S5 1803+784 and their labels used in this work.

Blazar	Flare label	Flare time in MJD	The time range in YYYY/MM/DD
S5 1803+784	Flare A	58942-58962	2020/04/03-2020/04/23
	Flare B	58983-59014	2020/05/14-2020/06/14
	Flare C	59072-59104	2020//08/11-2020/09/12
	Flare D	59158-59178	2020/11/05-2020/11/25
	Flare E	59207-59228	2020/12/24-2021/01/14
	Flare F	59287-59318	2021/03/14-2021/04/14

Table 3.1: (b) The flaring period of BL Lacertae and their labels used in this work.

BL Lacertae	Flare A1	59124-59135	2020/10/02-2020/10/13
	Flare A2	59225-59235	2021/01/11-2021/01/21
	Flare A3	59240-59251	2021/01/26-2021/02/06
	Flare A4	59328-59334	2021/04/24-2021/04/30
	Flare A5	59341-59349	2021/05/07-2021/05/15
	Flare A6	59400-59411	2021/07/05-2021/07/16
	Flare A7	59424-59435	2021/07/29-2021/07/09

Table 3.2: 4FGL-DR2 catalog 10-year average flux.

Blazar	Flux ($10^{-7}\mathrm{cm}^{-2}\mathrm{s}^{-1}$)
S5 1803+784	1.025±0.033
BL Lacertae	5.403 ±0.089

The quiescent fluxes in Table 3.2 are used as the baseline fluxes in Equation 3.1 to estimate the flares' rise and decay times. All the brightest flares from these sources during the flaring period with peak flux $F_{peak} \geq 3.0 \times 10^{-6}\mathrm{cm}^{-2}\mathrm{s}^{-1}$ were selected for the analysis.

The flare symmetry is estimated with the relation $\varepsilon = (t_r - t_f)/(t_r + t_f)$ with values ranging between -1 and 1 (Abdo *et al.*, 2010) where t_r is the rise time of the flare and t_f is the fall time (decay time). The duration of the flare ($\mathrm{t_d}$) for symmetric flares corresponds to the time the flux reduces to 20% of its peak value. The value of ε can provide a useful indication of the

physical evolution of the flare. Those with asymmetric profiles can be explored as a fast injection of accelerated particles and a slower radiative cooling or particle escape from the active emitting region. Symmetric flares, with or without a long-standing plateau, can be related to the crossing time of radiation (or particles) through the emitting region or can result from the superposition of several episodic flares of short duration. The ε parameter is used to define three different classes of flares: (1) symmetric flares where $-0.3 < \varepsilon < 0.3$, (2) moderately asymmetric flares when $-0.7 < \varepsilon < -0.3$ or $0.3 < \varepsilon < 0.7$, (3) markedly asymmetric flares when $-1.0 < \varepsilon < -0.7$ or $0.7 < \varepsilon < 1.0$.

The parameters t_0, t_r, t_f, of each flare in the *Fermi*-LAT detected gamma-ray light curves were determined by fitting to the function

$$F(t) = F_c + F_0\left(e^{-(t_0 - t/t_r)} + e^{-(t - t_0/t_f)}\right)^{-1} \quad 3.1$$

where t_0 is the time of the highest flux (F_0) and F_c and F_0 are the flux at the beginning of the flare and peak, respectively.

The time of the maximum of a flare (t_0) is

$t_0 = t_c + t_r t_f/(t_r + t_f)\ \ln(t_f/t_r)$ (Abdo *et al.*, 2010) and the duration of the flare (t_d) in the observer frame $t_d \cong 2(t_r + t_f)$.

The intrinsic duration of the flare in the source frame (t_s) is estimated through the observed frame transformation $t_s = t_d(\delta/(1+z))$.

The flux variability and timescale are important parameters to constrain the emitting region size and understand the nature of flares in blazars. The variability timescale constrains the size of the emitting region (e.g., Rajput *et al.,* 2020).

The flux doubling (T_b) time is

$$T_b = \frac{\ln 2(t_2 - t_1)}{ln\,[F(t_2)] - ln\,[F(t_1)]} \quad 3.2$$

where $F(t_1)$ and $F(t_2)$ are the fluxes measured at times t_1 and t_2 respectively.

If we take T_{fd} to be the fastest doubling time (T_b) during the flare, then the variability time $t_{var} = T_{fd}\, ln\, 2$. Thus, it gives the upper limit to the size scale of the emitting region as $R \leq ct_{var}(\delta/1+z)$ where z is the redshift, t_{var} is the minimum variability timescale (this can also be the shortest time scale between t_r and t_f) and δ is the Doppler factor.

In this work, the lambda cold dark matter (ΛCDM) cosmology, H_0= 71 km s^{-1} Mpc^{-1}, $\Omega_m = 0.27$, $\Omega_\Lambda = 0.73$ was used throughout (Larson *et al.*, 2011; Ade *et al.,* 2016).

3.3 Archival data

Archival data from multiwavelength observations of the blazars from radio to X-ray were obtained from the NASA/IPAC Extragalactic Database (NED)[3] and combined with the *Fermi*-LAT 4FGL-DR2 10-year catalog average νF_ν, were used to analyze the quiescent SEDs.

3.4 Radio data

Radio data obtained from the 15 GHz OVRO (Owens Valley Radio Observatory 40m Telescope) (Richards *et al.*, 2011) archive was used for the S5 1803+784 SED in the radio band, while Metsähovi Radio Observatory 14-m 37 GHz radio telescope data was obtained upon request was used for the SEDs of BL Lacertae. The previous studies have shown no clear correlation between the simultaneous radio and the gamma-ray emission of the two blazars studied in this work (Max-Moerbeck *et al.*, 2014; Nesci *et al.*, 2021); this is confirmed by our analysis shown in Figures 3.3 and 3.4 for the flare period.

3.4.1 Metsähovi Radio Observatory

The radio data were obtained from the Aalto University Metsähovi Radio Observatory 37GHz radio telescope.

Table 3.3: BL Lacertae 37 GHz radio data for October 2020 flare.

MJD	Flux (Jy)	uncertainty	Date (yyyy/mm/dd)
59124	3.05	0.12	2020/10/02
59125	3.39	0.18	2020/10/03
59126	3.16	0.18	2020/10/04
59127	3.16	0.13	2020/10/05
29134	2.88	0.25	2020/10/12

In order to determine if there is any correlation between the radio and the γ-ray light curves, the local cross-correlation function (LCCF) in Figures 3.3 and 3.4 was computed using the python code provided by Robertson *et al.* (2015). The cross-correlation significances of the two blazars are 1.53σ and 2.29σ for S5 1803+784 and BL Lacertae, respectively. These values are far less than 3σ level of significance required for cross-correlation significance between the radio and the gamma-ray energies defined in Max-Moerbeck *et al.*, (2014). The lack of clear

[3] http://ned.ipac.caltech.edu

correlation in the two blazars suggest either the radio source is embedded deep in the emitting region and being absorbed or the radio source and the γ-ray are from different part of the emitting region.

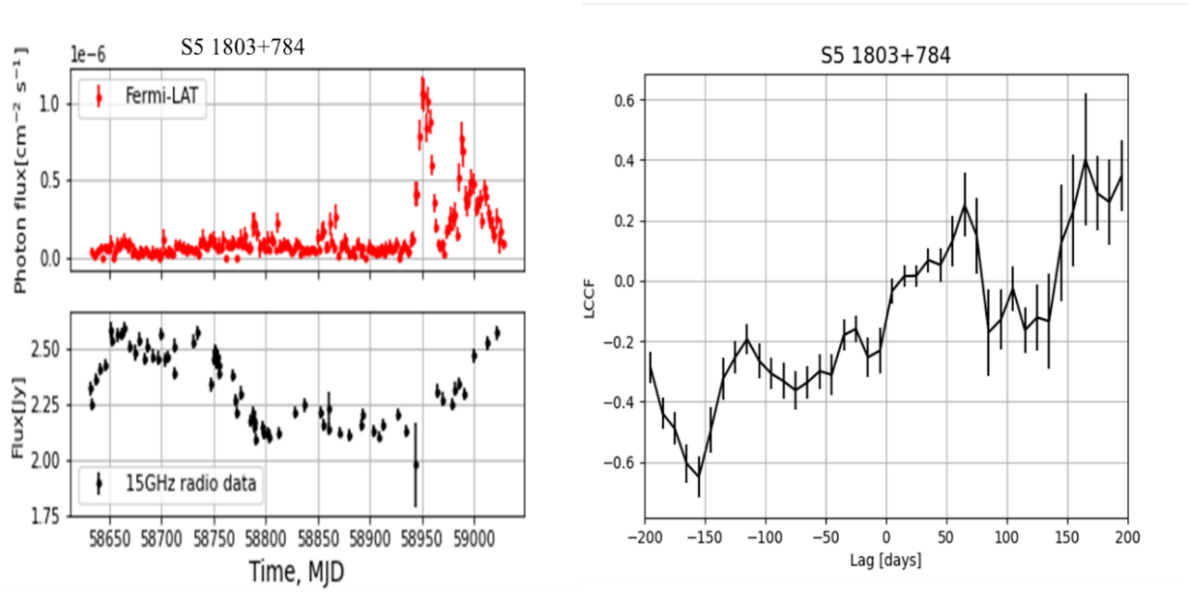


Figure 3.3: S5 1803+784 gamma-ray light curve (upper left), radio light curve (lower left) and the LCCF (right panel) (2019-05-30 to 2020-06-30) (Edelson and Krolik, 1988; Max-Moerbeck *et al.*, 2014; Robertson *et al.*, 2015).

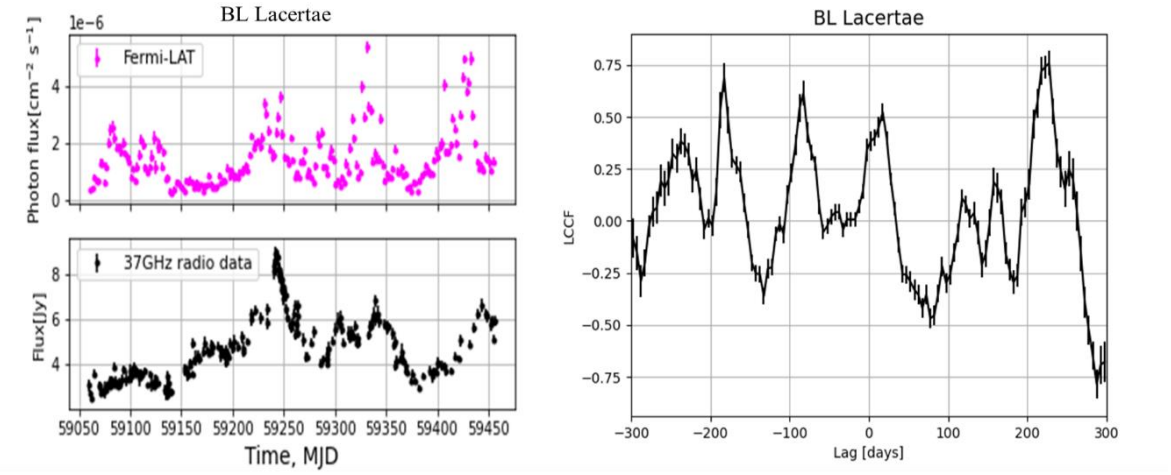


Figure 3.4: BL Lacertae gamma-ray light curve (upper left), radio light curve (lower left) and the LCCF (right panel) of the flare period (2020-07-30 to 2021-08-30) (Edelson and Krolik, 1988; Max-Moerbeck *et al.*, 2014; Robertson *et al.*, 2015).

3.5 Swift Telescope data

Filippo D'Ammando analyzed the Swift/XRT data, NuSTAR and NICER data in this Section and Section 3.6 while the Swift/UVOT and the ATLAS data were analysed by me. The Neil Gehrels Swift Observatory (Gehrels *et al.*, 2004) is a multiwavelength, rapid response space observatory launched on 2004 November 20. It has three instruments on board: the Burst Alert Telescope (BAT; Barthelmy *et al.*, 2005), sensitive in the 15-150 keV band; the X-Ray Telescope (XRT; Burrows et al. 2005), sensitive in the 0.3–10.0 keV band, and the UV and Optical Telescope (170–600 nm, UVOT; Roming *et al.*, 2005).

3.5.1 S5 1803+784 Swift/XRT/UVOT data

Swift (Gehrels *et al.*, 2004) observed S5 1803+784 twice in the period considered here, 2020, April 15 and 18 (MJD 58954 and 58957), with XRT and UVOT.

The XRT observations were performed in photon counting (PC) mode. The XRT spectra were generated with the Swift/XRT data products generator tool at the UK Swift Science Data Centre[4] (Evans *et al.*, 2009). The X-ray spectra in the 0.3-10 keV energy range are fitted by an absorbed power-law model using the photoelectric absorption model *tbabs* (Wilms, Allen and McCray, 2000) with a HI column density consistent with the Galactic value in the direction of the source as reported in Bekhti *et al.*, (2016), i.e., $n_H = 3.23\times 10^{20}\mathrm{cm}^{-2}$. We grouped the obtained spectra using the task *grppha* to have at least one count per bin, and we performed the fit with the Cash statistics (Cash, 1979). We used the spectral redistribution matrices in the Calibration database maintained by HEASARC. Spectra were fitted using XSPEC 12.9.1 (Arnaud, 1996). The uncertainties are estimated at the 90% confidence level. The X-ray spectra collected on 2020 April 15 and 18 can be fitted with a photon index of 1.66 ± 0.17 and 1.92 ± 0.20, respectively. The related observed 0.3-10 keV fluxes are $(4.73\pm0.45)\times 10^{-12}$ and $(3.31\pm0.35)\times 10^{-12}$ erg cm^{-2} s^{-1}, respectively. As a comparison, during the Swift observations performed in 2009 - 2015, the 0.3-10 keV X-ray flux varied between 2.36 and 4.36×10^{-12} erg cm^{-2} s^{-1} (Nesci *et al.*, 2021), indicating that the peak X-ray flux was observed on 2020 April 15. The photon index observed on 2020 April 15 is harder than the value observed on April 18 but is consistent with the values observed during the previous X-ray flares in 2009 and 2011, i.e., 1.4 - 1.5 (Nesci *et al.,* 2021).

The UVOT instrument observed the source on 2020 April 15 and 18 in its UV (m2 and w2) photometric bands (Breeveld *et al.*, 2010). UVOT data in the m2 and w2 filters were analyzed

[4] http://www.swift.ac.uk/user_objects

with the *uvotsource* task included in the HEASoft package (v6.29) and the 20211108 CALDB-UVOTA release. Source counts were extracted from a circular region of a 5 arcsec radius centered on the source, while background counts were derived from a circular region within a 20 arcsec radius in a nearby source-free region. The observed magnitudes are m2 = 14.33 ± 0.05 and w2 = 14.65±0.05 on 2020 April 15 and 18, respectively.

3.5.2 BL Lacertae Swift/XRT/UVOT data

Swift/XRT data were taken from 2020 October 2 to 2020 October 12 (Table 3.4) in Photon Counting mode for a net exposure of about 1.0, 1.0, 0.2, and 1.0 ksec, respectively (D'Ammando, 2020, 2022; Prince, Khatoon and Agarwal, 2021). Taking into consideration the Swift/XRT observations performed during 2005-2020, the source on 2020 October 6 reached the highest count rate in the 0.3-10 keV energy range (D'Ammando, 2022) with a factor of 3.5 higher than the flux observed on 2020 October 5, thereby reaching the historical maximum in X-rays (see Table 3.5). The UVOT data (Tables 3.5, 3.6, 3.7) were corrected for reddening and galactic extinction by applying the relationship of the dust emission derived reddening (Schlafly and Finkbeiner, 2011) for the three optical filters V, B, and U bands with extinction correction of 0.901, 1.192, and 1.425 magnitudes respectively.

Table 3.4: BL Lacertae Swift/XRT data simultaneous with Flare A1.

MJD	Flux $\times 10^{-11}$erg cm^{-2}s^{-1}	Uncertainty $\times 10^{-11}$erg cm^{-2}s^{-1}	Date (yyyy/mm/dd)
59124.7307	9.99	0.7	2020/10/02
59125.6557	1.76	0.23	2020/10/03
59126.5976	1.90	0.74	2020/10/04
59127.6383	16.90	1.26	2020/10/05
59128.1827	65.28	1.16	2020/10/06
59128.9421	17.14	0.87	2020/10/06
59129.9068	3.38	0.56	2020/10/07
59130.9076	3.60	0.25	2020/10/08
59131.9009	6.83	0.53	2020/10/09
59132.8915	5.35	0.31	2020/10/10
59133.8509	1.19	0.12	2020/10/11
59134.8915	1.70	0.26	2020/10/12

Table 3.5: V-band BL Lacertae data simultaneous with Flare A1.

MJD	Mag	uncertainty	Date (yyyy/mm/dd)
59124.7308	12.72	0.04	2020/10/02
59126.5976	13.23	0.07	2020/10/04
59127.6383	12.39	0.04	2020/10/05
59128.1827	12.62	0.04	2020/10/06
59128.9421	12.85	0.04	2020/10/06
59130.9076	13.22	0.04	2020/10/08
59131.9009	12.91	0.04	2020/10/09
59132.8915	13.00	0.04	2020/10/10
59133.8509	13.32	0.04	2020/10/11
59135.8352	13.12	0.04	2020/10/13

Table 3.6: B-band BL Lacertae data simultaneous with Flare A1.

MJD	Mag	uncertainty	Date (yyyy/mm/dd)
59124.7307	13.46	0.04	2020/10/02
59125.6557	13.87	0.04	2020/10/03
59126.5976	13.99	0.07	2020/10/04
59127.6383	13.14	0.05	2020/10/05
59128.1827	13.30	0.05	2020/10/06
59128.9421	13.62	0.05	2020/10/06
59130.9076	13.99	0.04	2020/10/08
59131.9009	13.61	0.04	2020/10/09
59132.8915	13.74	0.04	2020/10/10
59133.8509	14.10	0.04	2020/10/11
59134.8915	14.01	0.06	2020/10/13

Table 3.7: U-band BL Lacertae data simultaneous with Flare A1.

MJD	Mag	uncertainty	Date (yyyy/mm/dd)
59124.7307	12.97	0.05	2020/10/02
59125.6557	13.42	0.05	2020/10/03
59126.5976	13.53	0.07	2020/10/04
59127.6383	12.56	0.05	2020/10/05
59128.1827	12.72	0.05	2020/10/06
59128.9421	13.10	0.05	2020/10/06
59129.9068	13.32	0.06	2020/10/07
59130.9076	13.47	0.05	2020/10/08
59131.9009	13.14	0.05	2020/10/09
59132.8915	13.19	0.05	2020/10/10
59133.8509	13.63	0.05	2020/10/11
59134.8915	13.54	0.05	2020/10/12
59135.8352	13.46	0.05	2020/10/13

3.6 Other optical and X-ray data used in the SED model

3.6.1 ATLAS data

Asteroid Terrestrial-impact Last Alert System[5](ATLAS) consists of a network of four telescopes operated by the University of Hawaii Institute of Astronomy. Although the system was designed for asteroid discovery, it has data spinoffs in the optical band useful in photometry and blazar SED studies. The B-band (Table 3.8) and the R-band (Table 3.9) data, which correspond to the o-filter and the c-filter, respectively, obtained for S5 1803+784, were corrected for reddening and galactic extinction by applying the relationship of the dust emission derived reddening of 0.113 and 0.190 magnitude respectively (Schlafly and Finkbeiner, 2011) and used to build the simultaneous broadband SED of S5 1803+784.

Table 3.8: S5 1803+784 ATLAS c-filter of the B-band data simultaneous with Flare A.

MJD	B-band (mag)	uncertainty	Date (yyyy/mm/dd)
58960.532327	15.125	0.007	2020/04/21
58960.53279	15.125	0.006	2020/04/21
58960.536677	15.099	0.007	2020/04/21
58960.537137	15.104	0.006	2020/04/21
58960.541608	15.112	0.007	2020/04/21
58960.542558	15.106	0.006	2020/04/21
58960.554375	15.103	0.006	2020/04/21
58960.554833	15.109	0.007	2020/04/21
58964.538342	15.393	0.009	2020/04/25
58964.541129	15.387	0.011	2020/04/25
58964.546619	15.369	0.015	2020/04/25
58964.561438	15.59	0.148	2020/04/25

[5] https://www.fallingstar.com/home.php

Table 3.9: S5 1803+784 ATLAS o-filter of the R-band data simultaneous with Flare A.

MJD	R-band (mag)	uncertainty	Date (yyyy/mm/dd)
58942.618748	15.216	0.012	2020/04/03
58942.62228	15.223	0.016	2020/04/03
58942.627211	15.229	0.009	2020/04/03
58942.637091	15.199	0.013	2020/04/03
58946.527256	14.398	0.007	2020/04/07
58946.531341	14.423	0.007	2020/04/07
58946.538288	14.381	0.007	2020/04/07
58946.554349	14.405	0.007	2020/04/07
58950.499322	13.875	0.004	2020/04/11
58950.502114	13.864	0.004	2020/04/11
58950.50846	13.866	0.004	2020/04/11
58950.518371	13.866	0.004	2020/04/11
58956.554168	14.271	0.004	2020/04/17
58956.557388	14.271	0.005	2020/04/17
58956.562908	14.274	0.005	2020/04/17
58956.574684	14.304	0.005	2020/04/17
58956.596628	14.284	0.005	2020/04/17
58956.600587	14.282	0.005	2020/04/17
58956.607286	14.284	0.005	2020/04/17
58956.613553	14.285	0.004	2020/04/17
58962.503552	14.924	0.007	2020/04/23
58962.5071	14.927	0.007	2020/04/23
58962.514161	14.944	0.007	2020/04/23
58962.529975	14.937	0.008	2020/04/23

3.6.2 NuSTAR and NICER X-ray data observations from BL Lacertae

The Nuclear Spectroscopic Telescope Array (NuSTAR) (Table 3.10) observed BL Lac on 2020, October 11-12 at 3-79 keV, and the Neutron star Interior Composition Explorer (NICER) data were obtained from D'Ammando, (2022). The NICER flux corrected for galactic extinction in the 0.3-10 keV/0.4-5.0 keV bands are $(1.62 \pm 0.01) \times 10^{-11}$ and $(1.13 \pm 0.01) \times 10^{-12}$ erg $\mathrm{cm}^{-2}\mathrm{s}^{-1}$ from 2020 October 11 17:35:04 UTC (MJD 59133.58760417) to 2020 October 12 (MJD 59134.30288194). The X-ray data used in this work are extensively discussed in D'Ammando, (2022).

Table 3.10: NuSTAR orbit-by orbit observations of BL Lacertae 2020 October 11-12 (3-79 keV).

Flux $\times 10^{-11}\mathrm{erg\,m^{-2}s^{-1}}$	Uncertainty $\times 10^{-11}\mathrm{erg\,m^{-2}s^{-1}}$
3.19	0.30
2.55	0.23
2.71	0.25
2.80	0.24
2.86	0.24
3.10	0.36
2.99	0.30
3.47	0.30
3.85	0.42
3.77	0.37
2.16	0.30

3.7 *JetSeT* code implementation of the leptonic jet model

JetSeT (version 1.1.2)[6] is an open-source software package based on the C/Python framework. It is a numerical modeling and SED fitting tool for relativistic jets (Tramacere, 2020). It is useful to reproduce radiative and accelerative processes, allowing for a phenomenological study of jets. It is efficient in using observational data to constrain jet models. It implements the fitting of multiwavelength SEDs using the Minuit model minimizer, least square-bound (LSB), and Bayesian Markov chain Monte Carlo (MCMC) sampling (Massaro *et al.*, 2006; Tramacere *et al.*, 2009; Tramacere, Massaro and Taylor, 2011; Tramacere, 2020). In the phenomenological spectral fit, the *JetSeT* code Minuit minimizer, the MCMC sampler, and the observational data binned at 0.1 bin width in logarithmic frequency space are used to obtain the best-fit model parameters in this work.

3.7.1 Synchrotron and SSC model

Phenomenological fits can be used to put constraints on the physics of the emitting region and

[6] https://jetset.readthedocs.io/en/latest/

the acceleration mechanism driving the high energy emission in blazars. The synchrotron SED from the radio up to the optical and X-rays cannot be modelled with a single emitting region due to synchrotron self-absorption in the radio band, and the radio emission is usually considered to be from the extended radio portion of the jet. In this work, we do not model the extended radio emission. The synchrotron model consists of nine free parameters, i.e., three parameters for the emitting region (i.e. the magnetic field (B), the size of the emitting region (R), and the Doppler factor (δ)), and six for the particle distribution (i.e. the particle density (N), the low-energy cut-off Lorentz factor (γ_{min}), the turn-over energy Lorentz factor (γ_b) the high-energy cut-off Lorentz factor (γ_{max}), the low energy spectral slope (p) and the high energy spectral slope (p_1)). The process whereby the synchrotron photons are up-scattered by the same population of electrons that produced them is termed synchrotron self-Compton (SSC).

3.7.2 External inverse-Compton model

The black hole environment in Figure 3.5 shows that there are various sources of the photon field for the inverse-Compton scattering apart from the synchrotron seed photons in the jet. The radiative process in which external seed photons undergo inverse-Compton scattering is called external-inverse-Compton (EC). The likely sources of the external soft seed photons are thermal photons from the black hole accretion disk, optical/UV photons from the broad line region (BLR), and infrared photons from the dusty torus. Also, an important source of seed photons we do not consider in this work is the cosmic microwave background (CMB), which becomes relevant only when the emitting region is very far from the supermassive black hole (SMBH), where BLR and DT are absent. Using the SSC+EC model increases the number of free parameters with respect to the intrinsic jet parameters (SSC-only) discussed in Section 3.7.3. Additional parameters include the accretion disk luminosity (L_{Disk}), the fraction of disk luminosity that is assumed to be inverse-Compton scattered and re-emitted in the BLR (τ_{BLR}) and the dusty torus (τ_{DT}) respectively, the disk temperature (T_{Disk}), the temperature of the dusty torus (T_{DT}), and the sizes of the BLR and DT. These parameters are shown in Figure 3.5.

3.7.3 Electron distributions and the radiating particle model

The emitting region is assumed to be a sphere of radius R (Figure 3.6) with leptonic injection luminosity L_e (power), magnetic field B and particle Doppler (beaming) factor δ comoving with the bulk Lorentz factor Γ in the jet. A broken power-law function describes the energy spectrum of the relativistic electrons in the emission region (assuming more than one

acceleration mechanism in the jet), and the differential electron distribution per unit volume is as given below:

$$Q(\gamma)d\gamma = \begin{cases} Q_0\gamma^{-p}d\gamma, & \gamma_{min} < \gamma < \gamma_b \\ Q_0\,\gamma_b^{(p_1-p)}\gamma^{-p_1}d\gamma, & \gamma_b < \gamma < \gamma_{max} \end{cases} \quad 3.6$$

where γ_{max} and γ_{min} are the maximum and minimum electron Lorentz factors, p_1 is the high energy spectral slope, p is the low energy spectral slope, γ_b is the gamma break, γ is the Lorentz factor of electrons and positrons in the blob rest frame, and Q_0 is the normalization constant. The total power in the injected electrons is determined by $\int Q(\gamma)\gamma m_e\, c^2 d\gamma = L_e/V$, where $V = (4\pi/3)R^3$ is the volume of the spherical emitting zone (Figure 3.6), with radius R, m_e is the electron rest mass, and c is the speed of light. The steady-state energy spectrum of the emitting particles is:

$$N(\gamma) = Q(\gamma)\ \min\{t_{cross}, t_{IC}\} \quad 3.7$$

where $t_{cross} = R/c$ is the particle escape timescale in the emitting region and the cooling time (t_{IC}) is the time it takes the radiating particles to lose their energy (γ_{cool}).

The high-energy emission in blazars, especially in some BL Lacs that seem to have obscured emission lines and are therefore called masquerading BL Lacs, can originate from inverse Compton scattering of seed photons sources outside the jet (Giommi, Padovani and Polenta, 2013). The leptonic particle to cold proton particle ratio is assumed to be 10:1 in the model. The multiwavelength SEDs in this work are modelled with the synchrotron + SSC only and SSC + EC leptonic models; the goodness of fit and best-fit parameters are reported in Chapters 5 and 6.

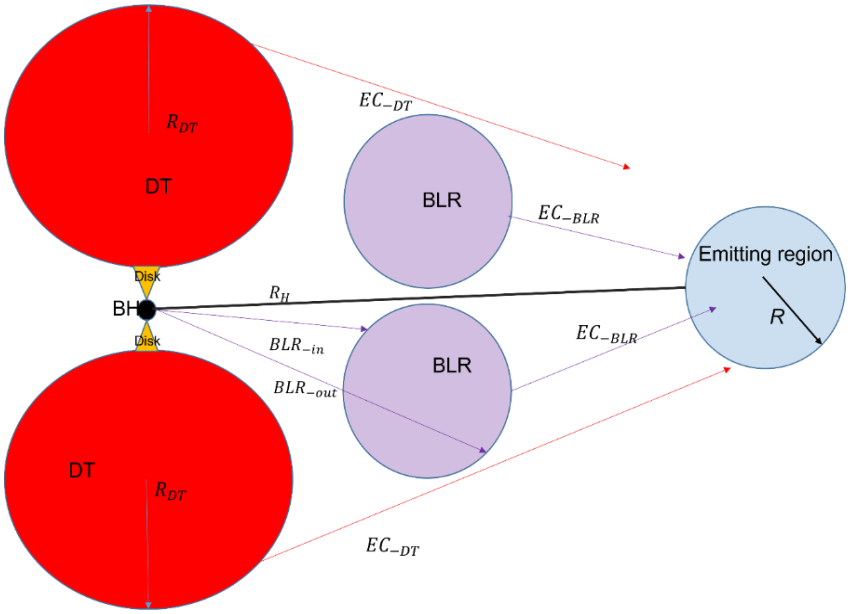


Figure 3.5: Leptonic jet model and parameters used in *JetSeT* (not to scale).

In this work, the emitting region (Figure 3.6), when considering the SSC+EC model, is assumed to be located outside the broad-line region (BLR), as described in Figure 3.5, where photons contributed from either the BLR or the dusty torus (DT) or both are expected (e.g., Arsioli and Chang, 2018; Harvey, Georganopoulos and Meyer, 2020).

3.7.4 Emitting region energy densities

The emitting region in Figure 3.6 has energy densities which are estimated using the relations below:

The electron distribution energy density (U_e) is given as

$$U_e = m_e c^2 \int Q(\gamma)\, d\gamma \qquad 3.11$$

The energy density of internal radiation synchrotron produced in the emission region that can be readily up-scattered through synchrotron self-Compton (SSC) is,

$U_{sync} = 4/9\,[nR\sigma_T\langle\gamma^2\rangle]U_B$, where n is the number density of the emitting particles. The energy density of high-energy photons that are produced through the inverse Compton process (IC) is, $U_{IC} = 4/9\,[nR\sigma_T\langle\gamma^2\rangle]U_{ph}$, where U_{ph} is the energy density of the up-scattered soft photons.

The total jet power (L_{jet}) in erg s^{-1} can be expressed as the sum of the various energy densities $L_{jet} = 2\pi R^2 c\Gamma^2\left(U_B + U_e + U_{ph}\right)$ The factor of 2 accounts for the existence of two-sided jets.

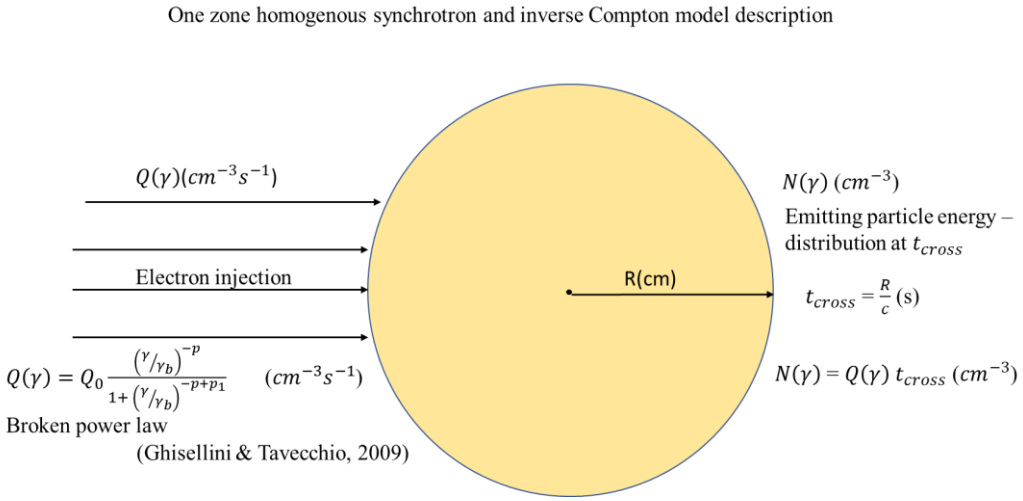


Figure 3.6: Emitting region model description (not to scale).

The total energy density, $U_i = U_{BLR}(\gamma) + U_{DT}(\gamma) + U_{sync}(\gamma) + U_{IC}(\gamma)$. U_{BLR} comprises the fraction of the external photons (EC) re-emitted from the broad-line region and U_{DT} is the portion of the infrared photons re-emitted/reprocessed from the dusty torus (Figure 3.3), each

of which is approximated as black body radiation, while U_{sync} comes from the synchrotron photons intrinsic to the emitting zone. The magnetic field energy density $U_B = B^2/8\pi$ while the energy density (U_{BLR}) of the broad-line region (BLR) and energy density (U_{DT}) of the dusty torus (DT) thermal emission in the blob rest frame as a function of emitting region distance (R_H) from the black hole (Ghisellini and Tavecchio, 2009; Hayashida *et al.*, 2012) are

$$U_{BLR}(\gamma) \approx (\tau_{BLR} L_{Disk} \Gamma^2 / 12\pi c R_{BLR}^2) k_1, \quad R_H \gg R_{BLR}, \tag{3.8}$$

$$k_1 = 1 - 2(1 + R_{BLR}^2/R_H^2)^{-3/2} + (1 + R_{BLR}^2/R_H^2)^{3/2} \text{ and}$$

$$U_{DT}(\gamma) \approx (\tau_{DT} L_{Disk} \Gamma^2 / 12\pi c R_{DT}^2) k_2, \quad R_H \gg R_{DT} \tag{3.9}$$

$$k_2 = 1 - 2(1 + R_{DT}^2/R_H^2)^{-3/2} + (1 + R_{DT}^2/R_H^2)^{3/2}$$

In the situation where the dissipation distance from the black hole (R_H) is less than the size of DT, the re-emitted photons from the dusty torus are the predominant source of the photon radiation field for external inverse Compton scattering, and the infrared energy density of the dusty torus becomes

$$U_{DT}(\gamma) = f_{DT} L_{Disk} \Gamma^2 / 4\pi c R_{DT}^2 \ , \quad R_H < R_{DT}, \tag{3.10}$$

where L_{Disk} is the accretion disk luminosity in which an equivalent τ_{BLR} of disk luminosity (L_{Disk}) is the fraction assumed to be inverse Compton scattered and re-emitted in the BLR and τ_{DT} that of the dusty torus, respectively.

3.7.5 *JetSeT*

3.7.5.1 Phenomenological spectral fits and model minimizers

The multiwavelength SED of the blazars during the flares observed in 2020 and 2021 and their redshifts are used as input to the Minuit model minimizer to constrain their physical parameters. *JetSeT* has two other model minimizers, least square (LB) and least square-bound (LSB), that can also be used. A broken power law parameterizes the electron injection spectrum. The energy bins of 1/10 of a decade were used as input for the spectral fits.

The phenomenological spectral fit modules in *JetSeT* are *jetset.test_data_helper*, *jetset.data_loader*, and *jetset.plot_sedfit*. In the SSC+EC model, we include the big blue bump (BBB) model and the infrared band cut-off frequency of the accretion disk without the galactic template of the host galaxy (see Appendix). These set the values of the physical features of the blazar jet based on the observed spectral energy distribution. The intrinsic jet parameters are mostly left as free parameters and are constrained with the minuit model minimizer until the values of the parameters converge. Then, the result of the minimizer is compared with the Markov Chain Monte Carlo (MCMC) sampling best-fit values of the intrinsic parameters of

the emitting region. The two-zone SED model in Chapter 7 was achieved using the composite model capability and Sherpa plug-in in *JetSeT* version 1.2.2.

3.7.5.2 Markov chain Monte Carlo (MCMC) sampling

JetSeT uses the Markov Chain Monte Carlo (MCMC) (Foreman-Mackey *et al.*, 2013) sampling method to find the confidence intervals of the free parameters based on the probability density function and obtain the 16th and 84th percentile of the upper and lower bounds of those parameters which are intrinsic to the emitting region. MCMC sampling may not be necessary if the values of the parameters converge well with the minimizer. The MCMC sampling and the code are shown in the Appendix.

3.8 Minimum Doppler factor

The minimum Doppler factor (δ_{min}) during the flares of each blazar can be estimated using

$$\delta_{min} = \left[\frac{\sigma_T d_L^2 (1+z)^{2\alpha} f_X E_\gamma}{t_{var} m_e c^4}\right]^{1/4+2\alpha} \quad \text{(e.g., Dondi and Ghisellini, 1995)} \qquad 3.12$$

Assuming the optical depth (τ) of the highest energy photons to γ-γ interactions is 1, then the minimum Doppler factor expressed in Equation 3.12 can be estimated as

$$\delta_{min} = \left[\frac{\sigma_T d_L^2 (1+z)^{2} f_X E_\gamma}{t_{var} m_e c^4}\right]^{0.167} \qquad 3.13$$

Here f_X is the X-ray flux, E_γ is the highest energy photon during the flare, and d_L is the luminosity distance. The highest-energy photon (E_γ) for S5 1803+784 is 11.77 GeV, while for BL Lacertae it is 14.09 GeV. The luminosity distance for S5 1803+784 d_L =4.46 Gpc ($1.38 \times 10^{28} cm$) and that of BL Lacertae is 0.31 Gpc (9.43×10^{26}cm). For the X-ray flux for S5 1803+784 f_X we used the X-ray flux observed by Swift/XRT on 2020 April 15, which is $(4.73 \pm 0.45) \times 10^{-12}$ erg cm^{-2} s^{-1} while for BL Lacertae it is $(65.28 \pm 1.16) \times 10^{-11}$ erg cm^{-2} s^{-1} (0.3-10 keV) as observed by Swift/XRT 2020 on October 6. The minimum Doppler factor (δ_{min}) estimated for S5 1803+784 is 5.89; this is smaller than the value of 12.2 calculated from VLBI observations (Hovatta *et al.*, 2009). In the case of BL Lacertae, we estimate δ_{min} to be 6.92, which is also smaller than the 7.3 estimated from VLBI observations by Hovatta *et al.*, (2009) and the average of 11 by Liodakis *et al.*, (2018).

3.9 BL Lacertae multiwavelength flux doubling timescale

The multiwavelength data in Sections 3.4 and 3.5 are used to calculate the flux doubling timescale in Table 3.11 using Equation 3.2.

Table: 3.11: BL Lacertae multiwavelength flux doubling timescale.

	$F(t_1)$ 10^{-11}erg cm^{-2}s^{-1}	$F(t_2)$ 10^{-11}erg cm^{-2}s^{-1}	t_1(MJD)	t_2(MJD)	T_b(days)
X-ray	16.90	65.28	59127.6383	59128.1827	0.24
Optical band					
V	23.16	50.20	59126.5976	59127.6383	0.93
B	21.04	46.03	59126.5976	59127.6383	0.92
U	21.63	52.84	59126.5976	59127.6383	0.81
Radio					
37 GHz	0.113	0.125	59124	59125	9.43

The flux doubling timescale is less than a day in all wavebands except the radio, which has a flux doubling time of 9.43 days. I will discuss the implications of Table 3.11 for the structure of the emitting region of BL Lacertae in Chapter 7.

The gamma-ray flux variability time scale is discussed in Chapters 5 and 6 for S5 1803+784 and BL Lacertae, respectively. It is used in building the single-zone multiwavelength leptonic jet models in Chapters 5 and 6, while the flux variability amplitude is discussed in Chapter 4.

CHAPTER 4

4.0 Multiwavelength flux variability and inverse Compton external seed photons

4.1 Gamma-ray flux variability

The fractional variability amplitude (F_{var}) is used to quantify the intrinsic variations in the two blazars' light curves during the flares. F_{var} is useful to determine the flux variability properties of the two blazars during the entire period of the flares studied in this work. F_{var} is defined as

$$F_{var} = \sqrt{\frac{S^2 - \bar{\sigma}_{err}^2}{\bar{x}^2}} \quad 4.1$$

where the sample variance (S^2) is defined as

$$S^2 = \frac{1}{N-1}\sum_{i=1}^{N}(x_i - \bar{x})^2 \quad 4.2$$

Here N is the number of flux points x_i, $\bar{x}$ is the arithmetic mean, and the mean square error ($\bar{\sigma}_{err}^2$) is:

$$\bar{\sigma}_{err}^2 = \frac{1}{N}\sum_{i=1}^{N}\sigma_{err,i}^2 \quad 4.3$$

The fractional variability amplitude uncertainty, $err(F_{var}) = \sqrt{\left(\sqrt{\frac{1}{2N}}\,\frac{\bar{\sigma}_{err}^2}{\bar{x}^2 F_{var}}\right)^2 + \left(\sqrt{\frac{\bar{\sigma}_{err}^2}{N}}\,\frac{1}{\bar{x}^2}\right)^2}$

where $F_{var} > 3err(F_{var})$ provides strong evidence for flux variability (Vaughan et al., 2003; Wani and Gaur, 2020; Rajput and Pandey, 2021).

Table 4.1: S5 1803+784 fractional variability amplitudes for Flare A and the entire duration of the Fermi-LAT observations up to 2022-03-30.

S5 1803+784	Flare A (1-day binned)	Flare period (7-day binned)	Long-term light curve (30-day binned)
Time range in MJD YYYY/MM/DD	58942-58962 2020/04/03-2020/04/23	58942-59318 2020/04/03-2021/04/14	54682-59668 2008/08/04-2022/03/30
S^2	1.06×10^{-13}	5.14×10^{-14}	1.13×10^{-14}
$\bar{\sigma}_{err}^2$	1.47×10^{-14}	1.42×10^{-15}	2.13×10^{-16}
$\bar{x}$	7.76×10^{-7}	3.18×10^{-7}	9.96×10^{-8}
F_{var}	0.39	0.70	1.06
$err(F_{var})$	0.19	0.10	0.19
N	18	53	166

The flux variability of S5 1803+784 is not well resolved in the daily binned light curve during

Flare A, as shown in Table 4.1. The 7-day binned light curve of the flare period (2020-2021) and the 30-day binned 13-year-long light curves have significant fractional variability amplitude (Table 4.1).

Table 4.2: BL Lacertae fractional variability amplitudes estimation for Flare A1 and the entire duration of the Fermi-LAT observations up to 2022-03-30.

BL Lacertae	Flare A1 (1-day binned)	Flare period (1-day binned)	Long-term light curve (30-day binned)
Time range in MJD	59124-59135	59124-59435	54682-59668
YYYY/MM/DD	2020/10/02-2020/10/13	2020/10/02-2021/07/09	2008/08/04-2022/03/30
S^2	1.09×10^{-12}	8.04×10^{-13}	1.67×10^{-13}
$\bar{\sigma}_{err}^2$	3.51×10^{-16}	4.92×10^{-17}	7.70×10^{-18}
$\bar{x}$	1.25×10^{-6}	1.16×10^{-6}	4.36×10^{-7}
F_{var}	0.838	0.774	0.935
$err(F_{var})$	0.004	0.0009	0.0006
N	16	668	166

BL Lacertae (Flare A1) shows a less than a day variability time scale during the outburst of October 6, 2020, and a significant fractional variability amplitude of 0.838 ± 0.004 (Table 4.2). From 2020 to 2021, the flares have a variability amplitude of 0.774 ± 0.0009. The 30-day binned 13-year long light curve shows a significant fractional variability amplitude of 0.935 ± 0.006 (column 4 of Table 4.2). The gamma-ray flux variability in the blazars could be attributed to the distribution of the relativistic electrons intrinsic to the emitting region of the jets that are accelerated to a very high Lorentz factor and are responsible for the non-thermal emission through synchrotron radiation and synchrotron self-Compton scattering processes.

The very short time scale gamma-ray flux variability in BL Lacertae suggests that the emission comes from a compact region within the jet; this scenario is consistent with the jet-in-jet model in which the mini-jets generated within the jet can have a large bulk Lorentz factor and can produce gamma-ray flux variability on short time scales (Rajput and Pandey, 2021). The short timescale variability could also come from the relativistic outflow from magnetic reconnection sites.

4.2 BL-Lacertae X-ray flux variability

The X-ray flux variability amplitude of BL Lacertae is highest during Flare A1, with a value of 1.650 ± 0.0011 (Table 4.3 and Figure 4.1).

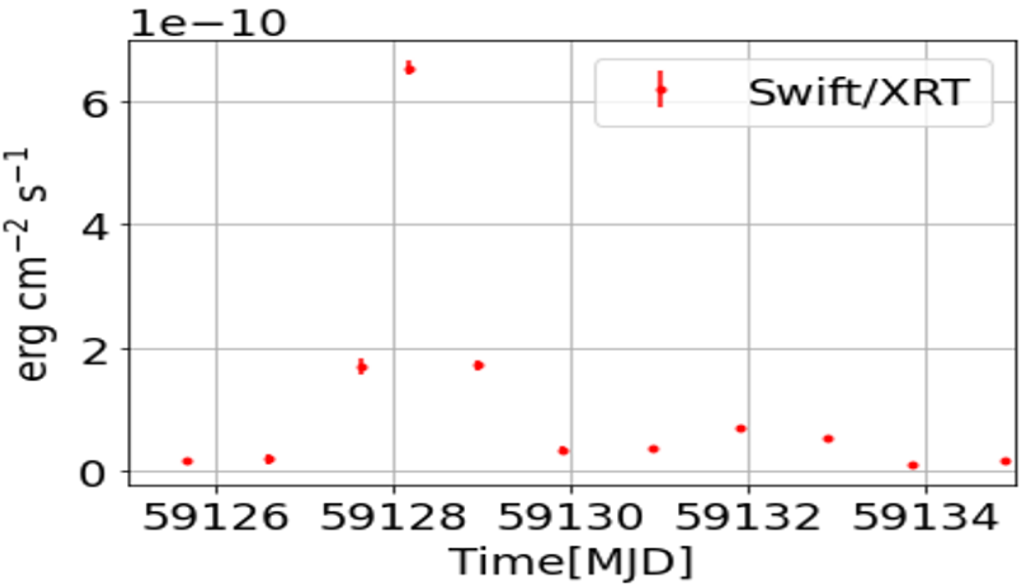


Figure 4.1: Flare A1 Swift/XRT 0.3-10 keV light curve.

Table 4.3: Flare A1 X-ray flux variability amplitude.

BL Lacertae The time range in MJD YYYY/MM/DD	Flare A1 period 59125-59135 2020/10/02-2021/07/09
S^2	3.013×10^{-20}
$\bar{\sigma}_{err}^2$	1.731×10^{-25}
$\bar{x}$	1.052×10^{-10}
F_{var}	1.650
$err(F_{var})$	0.0011
N	13

4.3 BL-Lacertae radio flux variability

There is no clear flux variability in the 37GHz radio observation during the period of Flare A1. Still, over the entire period, there is a significant radio flux variability with a variability amplitude of 0.313 ± 0.0005 (Table 4.4 and Figure 4.2).

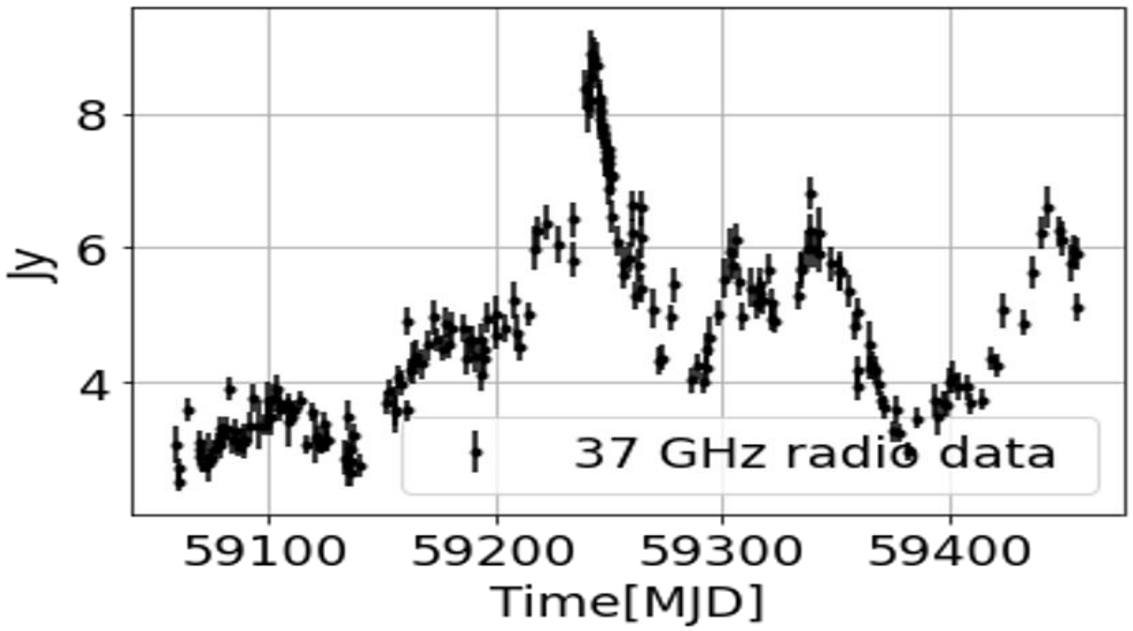


Figure 4.2: Flare period 37 GHz radio light curve.

Table 4.4: Flare-period radio flux variability amplitude.

BL Lacertae The time range in MJD YYYY/MM/DD	Flare period 59060-59456 2020/10/02-2021/07/09
S^2	2.248
$\bar{\sigma}_{err}^2$	2.692×10^{-4}
$\bar{x}$	4.791
F_{var}	0.313
$err(F_{var})$	0.0005
N	214

BL Lacertae shows significant multiwavelength flux variability during the flare period.

4.4 Flaring period photon seed factor

The photons seed factor (PSF) is unique to the photon population being up-scattered; it can serve as a diagnostic tool to understand the time evolution of the gamma-ray emission mechanism using purely observationally derived data (Harvey, Georganopoulos and Meyer, 2020). Following the derivation of Harvey et al. given in Equation 2.27 and restated below, the photon seed factors of the flares (Table 4.7) are estimated using the observational data listed in

Table 4.6.

$$\text{PSF} = \log_{10}\left[3.22 \times 10^{4}\left(k_1^{1/2}\nu_{\text{sync},13}/\nu_{\text{IC},22}\right)\right],$$

where k_1 is the ratio of the inverse Compton peak luminosity to the synchrotron peak luminosity in units of 10, $\nu_{\text{sync},13}$ is the peak frequency of the synchrotron peak in units of 10^{13} Hz, and $\nu_{\text{IC},22}$ is the peak frequency of the inverse Compton component in units of 10^{22} Hz. The peak fluxes and frequencies of both the synchrotron radiation and the inverse Compton radiation (Table 4.5) were determined in *JetSeT* by fitting the SEDs (Figures 4.3, 4.4, 4.5, and 4.6) to the third-degree polynomial function in Equation 4.4 (Kubo *et al.*, 1998; Abdo *et al.*, 2010).

$$\nu F_\nu = a\nu^3 + b\nu^2 + c\nu + d \qquad 4.4$$

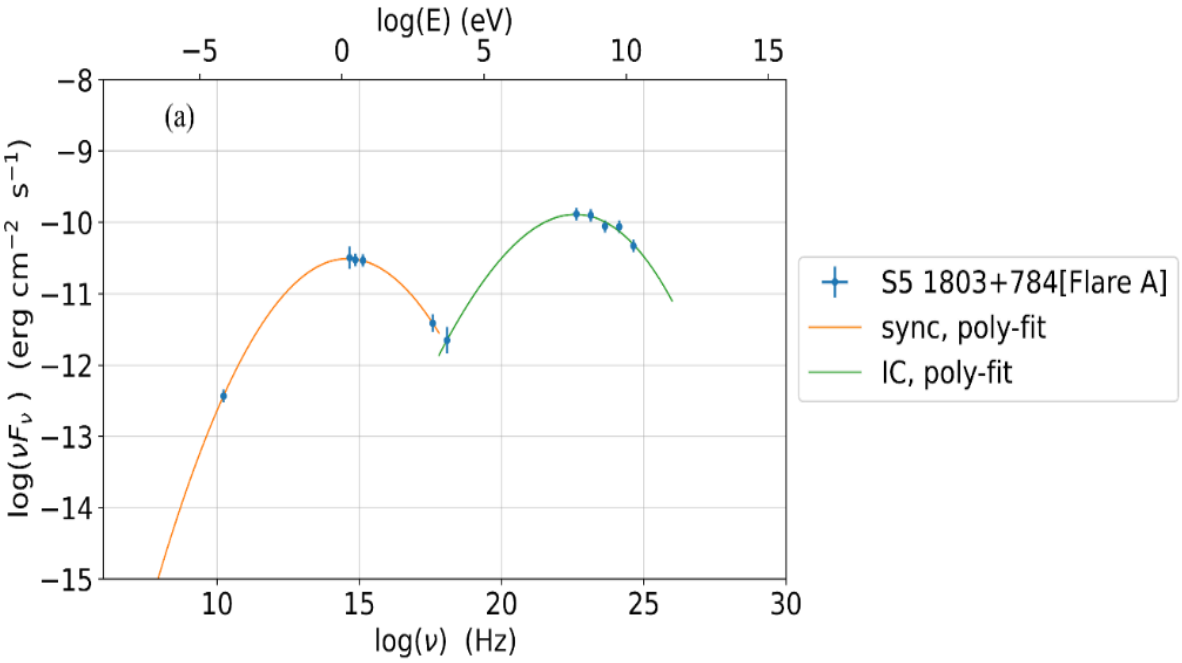


Figure 4.3: (a) S5 1803+784 polynomial fit to determine the peak fluxes and frequencies (Flare A1).

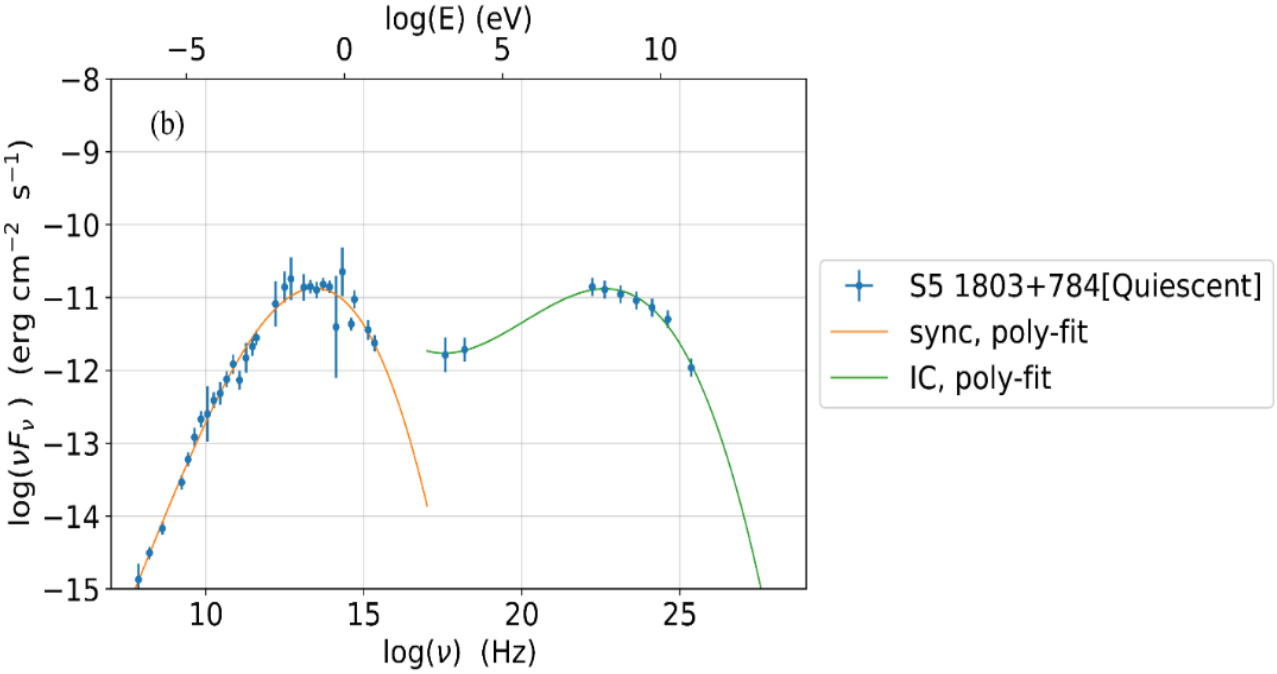


Figure 4.4: (b) S5 1803+784 polynomial fit to determine the peak fluxes and frequencies (Quiescent state).

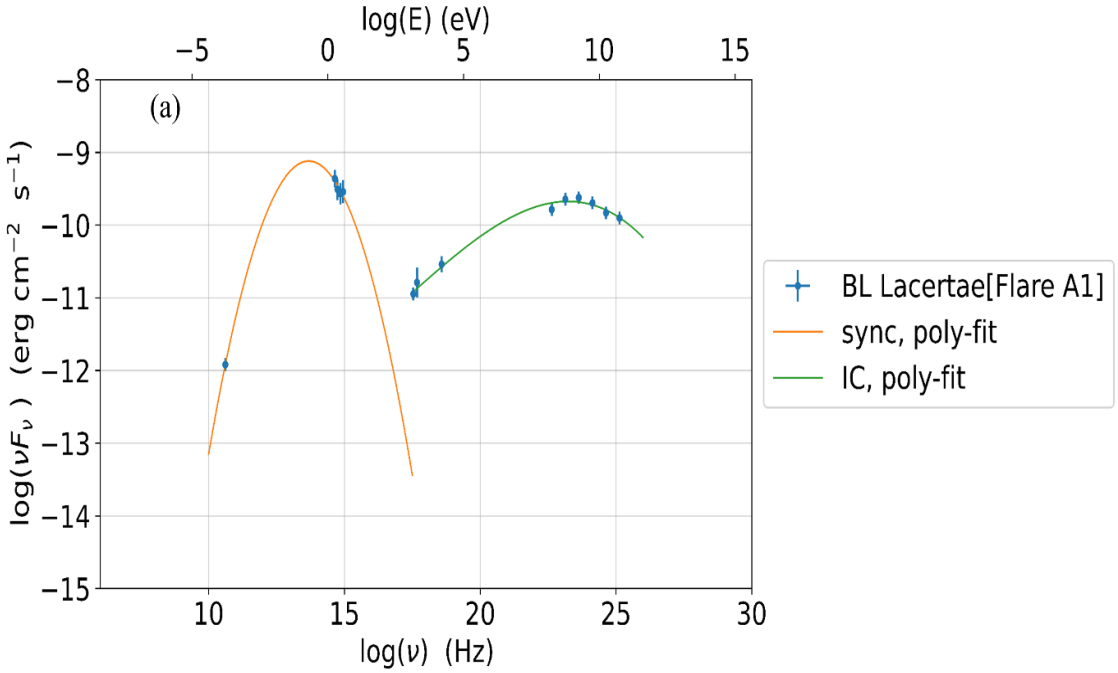


Figure 4.5: (a) BL Lacertae polynomial fit to determine the peak fluxes and frequencies (Flare A1).

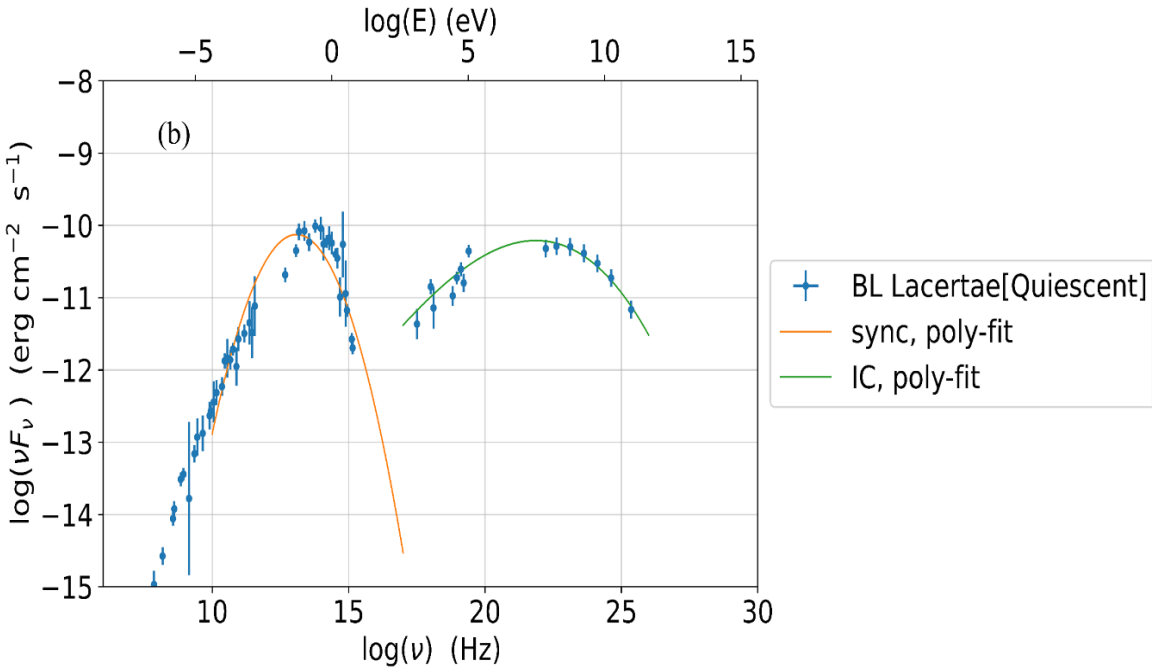


Figure 4.6: (b) BL Lacertae polynomial fit to determine the peak fluxes and frequencies (Quiescent state).

Table 4.5: Summary of the peak fluxes and frequencies of the flares.

Blazar Flare Labels	Peak inverse Compton Frequency Log (ν_{IC}) (Hz)	Peak IC Flux Log ($\nu_{IC}F_{\nu_{IC}}$) erg cm^{-2}s^{-1}	Peak synchrotron Frequency Log (ν_{sync}) (Hz)	Peak synchrotron Flux Log ($\nu_{sync}F_{sync}$) erg cm^{-2}s^{-1}	Time of peak flux (MJD)
S5 1803+784 Flare A	22.60±0.60	-9.89±0.06	14.59±0.15	-10.52±0.15	58951
BL Lacertae Flare A1	23.23±0.36	-9.68±0.05	14.03±0.05	-9.24±0.39	59128

Table 4.6: Summary of the peak fluxes and frequencies of the quiescent states.

	Peak inverse Compton Frequency Log (ν_{IC}) (Hz)	Peak IC Flux Log ($\nu_{IC}F_{\nu_{IC}}$) erg cm^{-2}s^{-1}	Peak synchrotron Frequency Log (ν_{sync}) (Hz)	Peak synchrotron Flux Log ($\nu_{sync}F_{sync}$) erg cm^{-2}s^{-1}
S5 1803+784	22.63±0.20	-10.88±0.03	13.46±0.05	-10.87±0.04
BL Lacertae	21.87±0.23	-10.21±0.05	13.31±0.02	-10.12±0.04

Table 4.7: Observer frame (obs) synchrotron and inverse Compton peak luminosities, and the photon seed factor during the flares.

	Flares Label	Inverse Compton peak luminosity (L_{IC-obs})	Synchrotron peak luminosity ($L_{sync-obs}$)	PSF
S5 1803+784		$(L_{IC}) \times 10^{47}\text{erg s}^{-1}$	$(L_{sync})\times 10^{46}\text{erg s}^{-1}$	4.36±0.11
	Flare A	3.07±0.06	7.21±0.20	
BL Lacertae		$(L_{IC})\times 10^{45}\text{erg s}^{-1}$	$(L_{sync})\times 10^{45}\text{erg s}^{-1}$	3.80±0.11
	Flare A1	2.34±0.05	6.43±0.39	

The flare-time PSF of S5 1803+784 in Table 4.7 above compared with the values obtained for the BLR and the DT (Harvey, Georganopoulos and Meyer, 2020), $\text{PSF}_{\text{BLR}} = 3.29 \pm 0.11$ and $\text{PSF}_{\text{DT}} = 3.92 \pm 0.11$, suggests that the seed photons for the inverse Compton process in the emitting region of this blazar during Flare A are probably re-emitted photons from the DT.

In the case of BL Lacertae, the PSF in Table 4.7 also agrees with the assumption in this work that the emitting region of BL Lacertae during Flare A1 is beyond the BLR but within the region of influence of the BLR UV/optical photons. The BLR can still be the source of the external seed photons for inverse Compton scattering. This is likely to be the case in BL Lacertae since VHE emission has been detected (e.g., Acciari *et al.*, 2019).

Table 4.8: Observer frame synchrotron and inverse Compton peak luminosities in the quiescent states.

	Inverse Compton peak luminosity (L_{IC-obs})	Synchrotron peak luminosity ($L_{sync-obs}$)
S5 1803+784 Quiescent	$(L_{IC}) \times 10^{46}\text{erg s}^{-1}$	$(L_{sync})\times 10^{46}\text{erg s}^{-1}$
	3.15±0.03	3.22±0.04
BL Lacertae Quiescent	$(L_{IC})\times 10^{44}\text{erg s}^{-1}$	$(L_{sync})\times 10^{44}\text{erg s}^{-1}$
	6.89±0.05	8.48±0.04

The peak luminosities (L) of both the synchrotron radiation ($L_{sync-obs}$) and the inverse Compton scattering (L_{IC-obs}) (Table 4.5) were estimated using the relation $L = 4\pi d_L^2 \nu f_\nu^{peak}$ (e.g., Arsioli and Chang, 2018), where d_L is the luminosity distance, and νf_ν^{peak} is the peak flux density. ΛCDM cosmology, as stated in Section 3.1, is used to calculate the photon seed factors PSFs in column 5 of Table 4.7.

S5 1803+784 shows inverse Compton dominance during the flare, with peak luminosity in the range of $\times 10^{47} \mathrm{erg\ s^{-1}}$ (Table 4.5), while BL Lacertae is near equipartition due to UV/optical photons that dominate the synchrotron radiation; this could be interpreted as the emitting region moving outside the BLR, where cooling becomes inefficient (e.g., Ghisellini *et al.*, 2013; Hovatta and Lindfors, 2019).

The inverse Compton dominance in S5 1803+784 suggests that the emitting region during this flare is closer to an external photon radiation field for the inverse Compton scattering while that of BL Lacertae is further beyond the BLR.

CHAPTER 5

5.0 S5 1803+784 (4FGL J1800.6+7828)

5.1 S5 1803+784 flares of 2020 April to 2021 April

S5 1803+784 is a low synchrotron peak (LSP) BL Lac object. Evidence abounds in the literature that most LSP blazars are not well fit by a single-zone SSC model without contributions of soft photons from external sources for the observed gamma-ray flares (e.g., Hervet, Boisson and Sol, 2015; Arsioli and Chang, 2018). Here we fit leptonic models to multiwavelength data from observations taken during Flare A of S5 1803+784 using the single-zone synchrotron+SSC-only and SSC+EC models discussed in Chapter 3. The temporal characteristics and the gamma-ray spectra of the flare are also discussed in this Chapter.

Fermi-LAT observed gamma-ray flaring activity from S5 1803+784 was first reported in ATel #13633 (Venters, Angioni and Ojha, 2020). The flares took place from MJD 58942 to MJD 59318, one of the longest and brightest flaring periods observed from this source since the beginning of the *Fermi*-LAT observations. The flaring period shows six identifiable flares from the daily binned light curve and the profile of the Bayesian blocks (Figure 5.1). The gamma-ray emission model and the *Fermi*-LAT analysis results are discussed in the next section.

Figure 5.1is the daily binned light curve of S5 1803+784 (0.1-300 GeV).

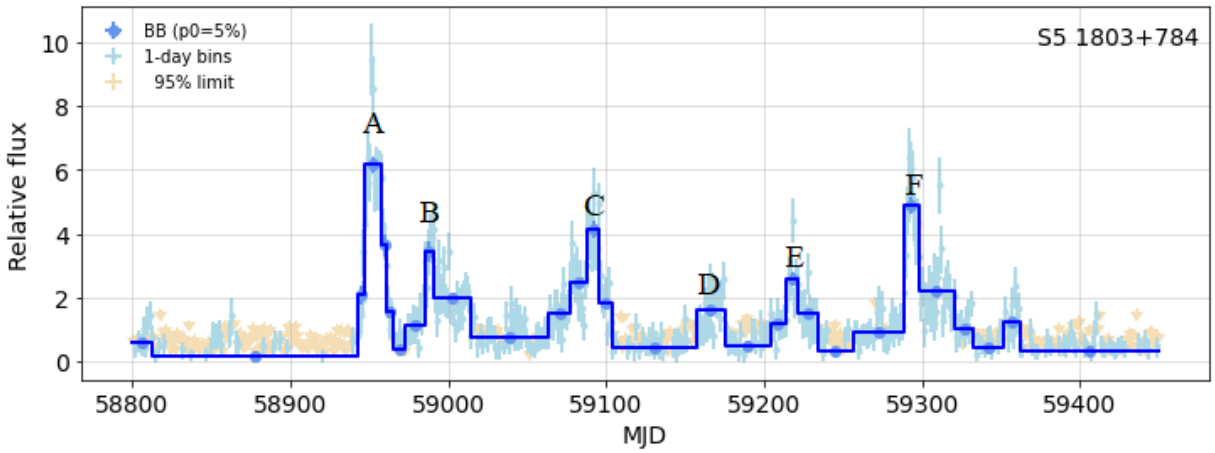


Figure 5.1: S5 1803+784 Bayesian blocks showing the period of the flares and the flare epochs in a daily binned light curve (0.1-300 GeV).

5.1.1 S5 1803+784 gamma-ray emission model and characteristics

The gamma-ray spectrum of this blazar is well-described by a log parabola distribution function. Table 5.1 shows the log parabola distribution (LP) compared with the power-law (PL) and the broken power-law (BPL) models. The spectra for each flare using the three spectral models are presented in Figure 5.1. All the flares show similar features and shapes except Flare B, with a higher spectral curvature than the other flares, and Flare E, which shows a similar spectrum to the previous flares but with a lower curvature and a spectrum that extends to ~126GeV. The spectral characteristics of the flares are shown in Table 5.2.

Table 5.1: Comparison of the gamma-ray spectral models for S5 1803+784.

Label	TS(PL)	TS (LP)	TS(BPL)	TS_{curve}
Flare A	3093.46	3123.66	3089.42	30.20
Flare B	2139.43	2196.85	2160.46	57.42
Flare C	2417.21	2471.79	2410.98	54.58
Flare D	956.63	977.15	970.43	20.52
Flare E	1491.38	1561.17	1509.14	69.79
Flare F	2277.65	2320.89	2270.48	43.24

$TS_{curve} = 2\sum_i\left(logL_{LP,i} - logL_{PL,i}\right)$ (Mattox *et al.*, 2006; Nolan *et al.*, 2016)
is statistically significant ($> 4\sigma$) for all the flares. It is clear from Table 5.2 that the LP model best describes the gamma-ray spectra of S5 1803+784.

Table 5.2: Spectral characteristics of the gamma-ray spectrum of S5 1803+784 during the flares using the log-parabola model.

	Label	Peak Flux (10^{-7}cm^{-2}s^{-1})	α	β	Norm (10^{-11}MeV^{-1} cm^{-2}s^{-1})	E_b (MeV)	TS
S5 1803+784	Flare A	14.00 ±1.68	2.14±0.03	0.057±0.02	17.08±0.75	673.6	3123.66
	Flare B	8.76±1.51	2.18±0.04	0.096±0.03	8.84±0.45	673.6	2196.85
	Flare C	10.91 ± 1.64	2.29±0.03	0.025±0.02	9.24±0.45	673.6	2471.79
	Flare D	5.79±1.06	2.24±0.05	0.081±0.04	6.74±0.49	673.6	977.15
	Flare E	7.39±1.10	2.24±0.04	0.018±0.03	7.44±0.48	673.6	1561.17
	Flare F	12.43±1.61	2.26±0.03	0.030±0.02	11.34±0.56	673.6	2320.89

Table 5.3: Comparison of the gamma-ray spectra parameters of the log parabola (LP) distribution function for the two blazars. LT is the long-term SED from 2008/08/04-2022/03/30; FT is the 2020-2021 flare period, and Flare A is defined in the text.

	MJD	α	β	N_0 (10^{-11}MeV^{-1} cm^{-2}s^{-1})	E_b (MeV)	TS
S5 1803+784	54682-59668 (LT)	2.18±0.01	0.047±0.02	2.1±0.02	673.6	36192.14
	58942-59318 (FT)	2.23±0.01	0.040±0.01	6.09±0.08	673.6	14956.26
	Flare A	2.14±0.03	0.057±0.02	17.08±0.75	673.6	3123.66

The spectral features of S5 1803+784 in Table 5.3 do not show any significant differences between the photon indices and spectral curvatures in the long term (LT) and during the 2020-2021 flares, except that Flare A has a slightly higher spectral curvature.

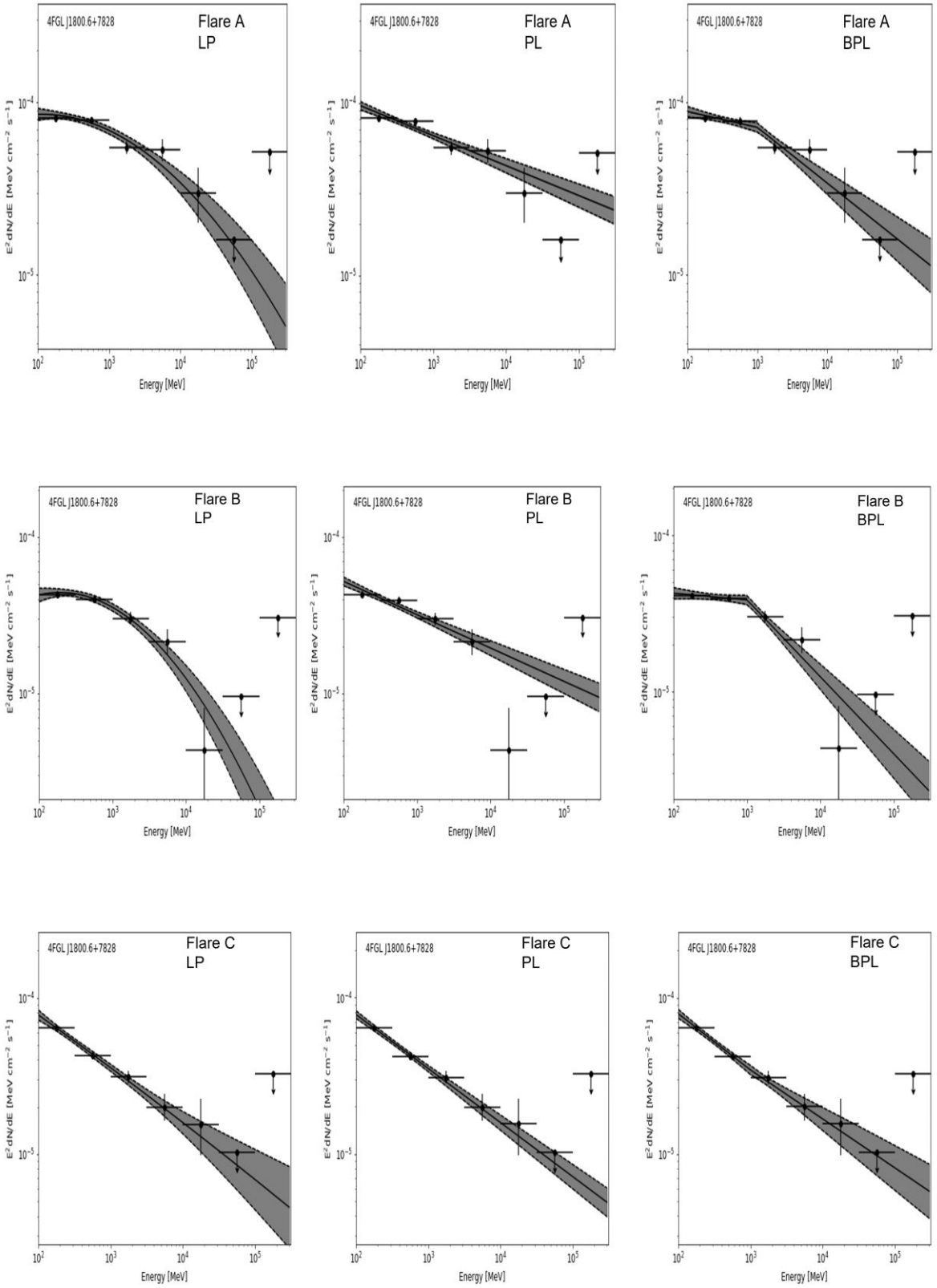


Figure 5.2: The gamma-ray spectra of the six flares of S5 1803+784 fitted with three spectral models (continued on the next page).

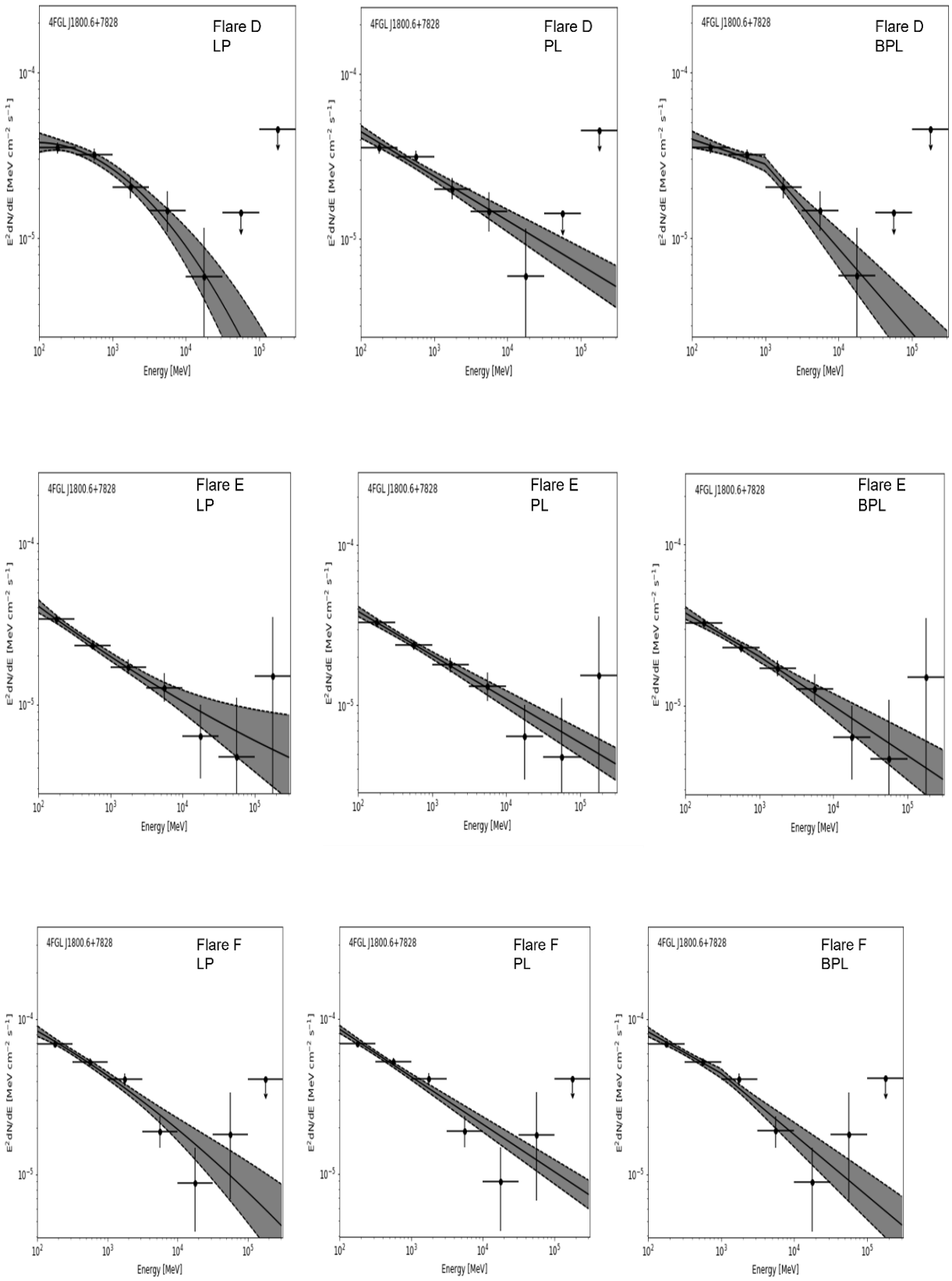


Figure 5.2: The gamma-ray spectra of the six flares of S5 1803+784 fitted with three spectral models.

5.1.2 Temporal profiles of S5 1803+784 flares and broadband spectral fits

The temporal profile of the flares in Table 5.4 shows the flare rise time (t_r), and the flare decay time (t_f). The duration of the flares (t_d) in the observer frame in days is discussed below.

The duration of Flares A, B, C, D, E, and F in the observer frame $t_d \cong 2(t_r + t_f)$ = 20.5 days, 17.36 days, 21.26 days, 32.60 days, 24.98 days, and 16.08 days. According to the symmetry factor: $\varepsilon = (t_r - t_f)/(t_r + t_f)$, Flares A, C, D and E, with $\varepsilon_{\text{Flare A}}$ = -0.22, $\varepsilon_{\text{Flare C}}$ = -0.14, $\varepsilon_{\text{Flare D}}$ = -0.02, and $\varepsilon_{\text{Flare E}}$= 0.04, respectively, have symmetric flare profiles according to the definition in Abdo *et al.* (2010), while Flare B with $\varepsilon_{\text{Flare B}}$ = -0.72 and Flare F with $\varepsilon_{\text{Flare F}}$= -0.41 are flares with asymmetric profiles.

The shortest flare duration is Flare F, while the longest flare is Flare D.

Figure 5.3 shows the temporal profiles of the flares where each flare is fitted with the flare profile function $F(t) = F_c + F_0\left(e^{-(t_0 - t/t_r)} + e^{-(t - t_0/t_f)}\right)^{-1}$ to determine the parameters in Table 5.4.

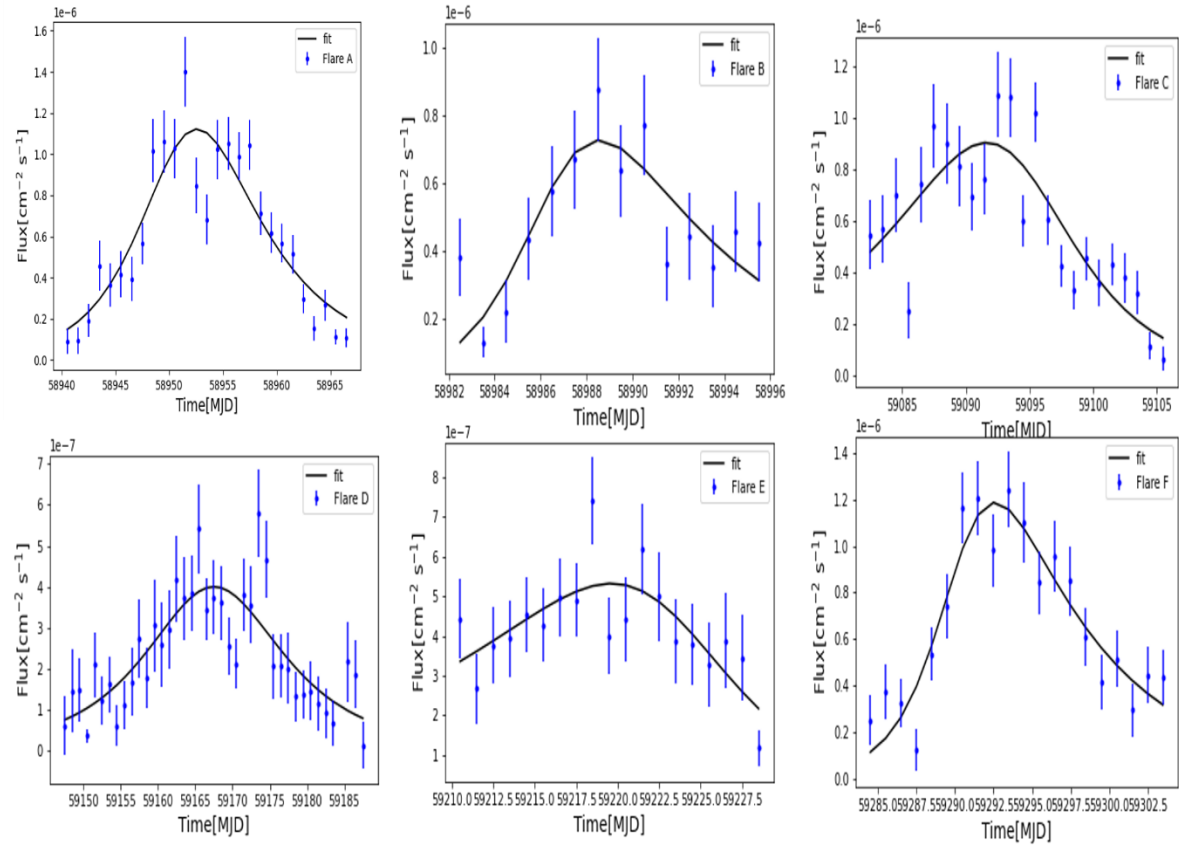


Figure 5.3: Temporal profiles of the flares, each fitted with the function in Equation 3.6.

Table 5.4: Temporal characteristics of S5 1803+784 during the flares.

Label	t_r (day)	t_{f} (day)	t_0 (MJD of peak flux)	$F_c(\times 10^{-7}\ \mathrm{cm^{-2}s^{-1}})$	$F_0(\times 10^{-7}\ \mathrm{cm^{-2}s^{-1}})$
Flare A	3.99	6.26	58951	1.92 ±0.80	14.00 ±1.68
Flare B	1.23	7.45	58988	1.30 ±0.45	8.76±1.51
Flare C	4.56	6.07	59092	2.51±1.08	10.91 ± 1.64
Flare D	8.01	8.29	59173	0.78 ±0.74	5.79±1.06
Flare E	6.52	5.97	59218	2.67±0.61	7.39±1.10
Flare F	2.37	5.67	59293	2.50±1.05	12.43±1.61

The duration, symmetry, and the rise time of Flare A suggest a superposition of rapid episodic flares and radiating particles being injected into the emitting region. Asymmetric flares B and F with the fastest rise time suggest a fast injection of relativistic electrons into the emitting region. The rapid variability observed in these flares is consistent with magnetic dissipation in reconnecting field lines as the mechanism enhancing particle acceleration during the flares (e.g., Christie *et al.*, 2019).

5.1.3 Multiwavelength SED of S5 1803+784

In the SED modelling of Flare A, we used the decay time to estimate the size of the emitting region. Flare A has a rise time (t_r) of 3.99 days and decay time (t_{f}) of 6.26 days (Table 5.4); if we assume the Doppler factor (δ) of 12.2 from VLBI observations of S5 1803+784 (Hovatta *et al.*, 2009), then the size of the emitting region $R < c\delta t_{var}/(1+z) = 5.20 \times 10^{16}$cm where $t_{var} = t_r\, ln\, 2$. But in the SED modelling, $R = 3.42 \times 10^{16}$ cm produced the best fit. Furthermore, the distance of the emitting region from the black hole (R_H) can be constrained, reducing the number of degrees of freedom in modeling the SED, using the relation $R_H \sim 2c\Gamma^2\, t_{var}/(1+z)$, where we used $\Gamma = 9.45$ for the bulk Lorentz factor. (Hovatta *et al.*, 2009; Savolainen *et al.,* 2010). The distance of the emitting region from the black hole is then $R_H = 5.00 \times 10^{17}$cm.

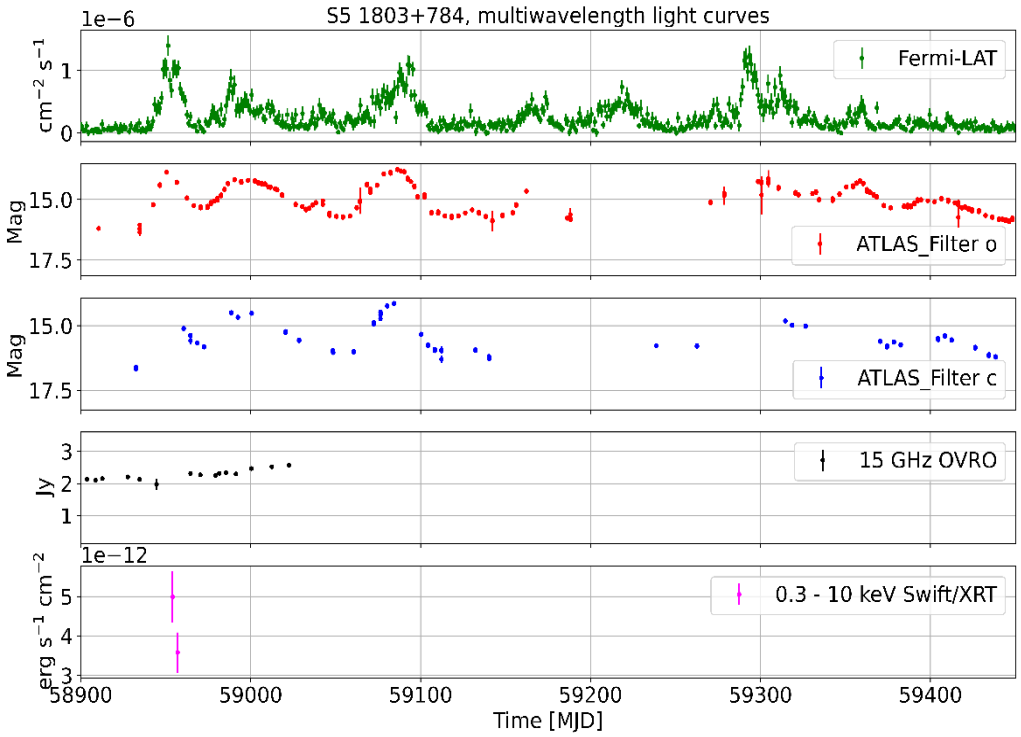


Figure 5.4: Multiwavelength light curve of S5 1803+784.

The SED of S5 1803+784 was modelled with a leptonic jet model with synchrotron+SSC-only components and SSC+EC components, assuming the EC are disk photons re-emitted by the dusty torus, to test whether S5 1803+784 is a masquerading BL Lac (Giommi, Padovani and Polenta, 2013), even though there is as yet no consistent observational evidence for the existence of a dusty torus in BL Lacs (Hovatta and Lindfors, 2019). The goodness of fit of the two models for the quiescent state SEDs were compared using the F-test. The models were fit to both the quiescent state SED and that of Flare A, which coincides with the first gamma-ray peak in the multiwavelength light curves in Figure 5.4. According to both models, the X-ray flares of April 15 and 18 are dominated by the upper tail of the synchrotron emission, which has not been previously observed in this blazar. The SEDs and model fit results for the two leptonic models in the two different states of S5 1803+784 are reported in Tables 5.5, 5.6, and 5.7 and Figures 5.5, 5.7, 5.9, and 5.11 are the fits using the Minuit minimizer while Figures 5.6,5.8, 5.10, and 5.12 are the fits using the MCMC sampling.

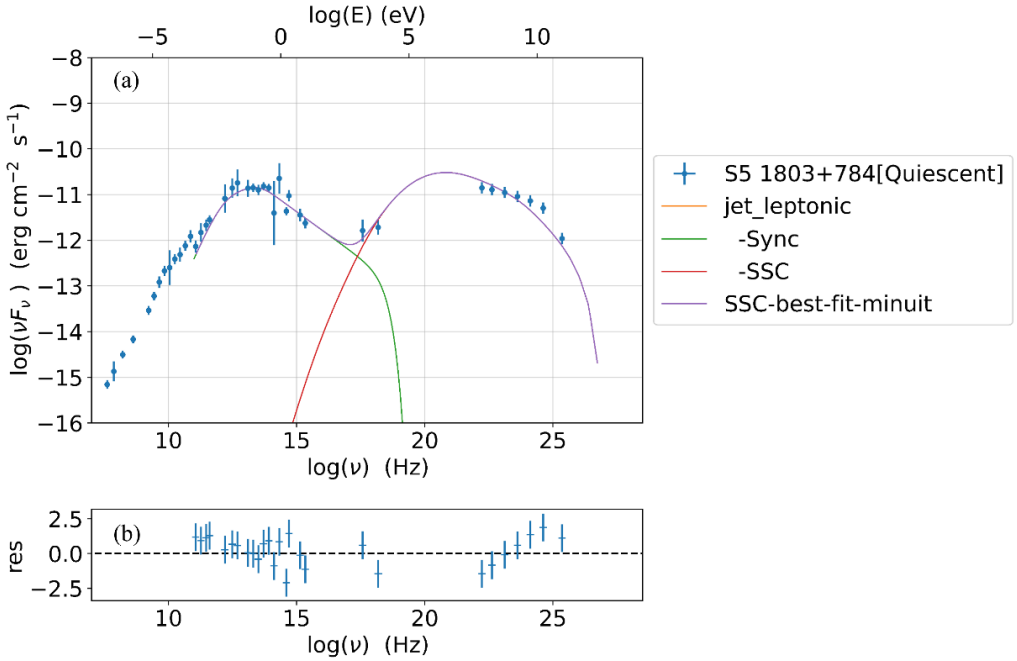


Figure 5.5: (a) S5 1803+784 broadband SED (Quiescent state, best-fit SSC model); (b) Residual of the fit.

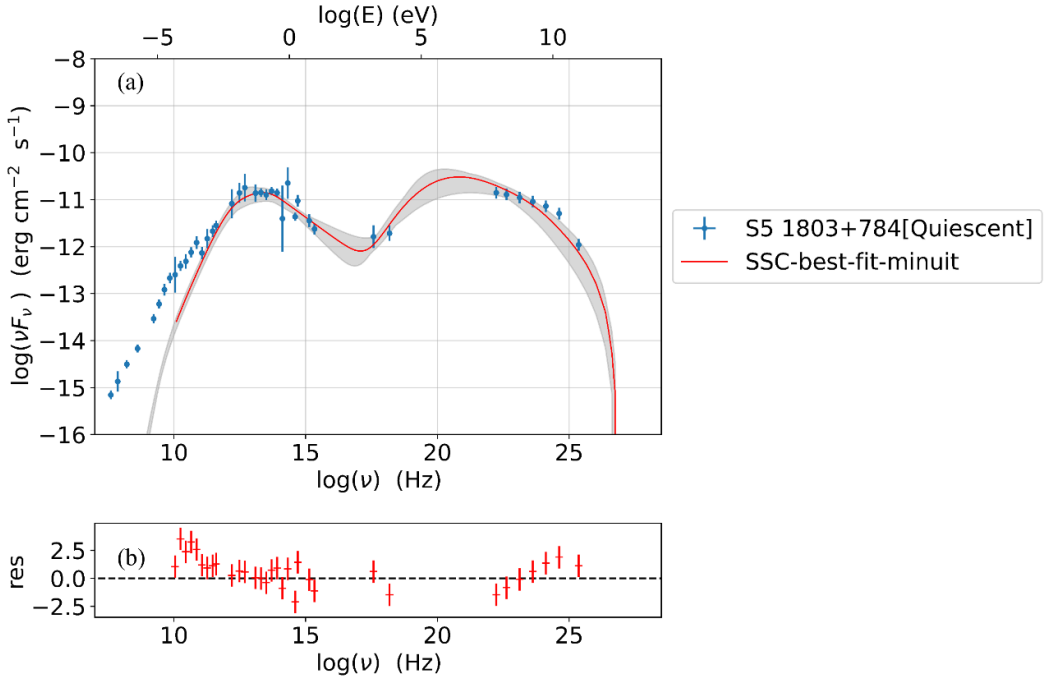


Figure 5.6: (a) S5 1803+784 broadband SED (Quiescent state, best-fit SSC model), where the shaded area is the upper and the lower bounds of the MCMC sampling; (b) Residual of the fit.

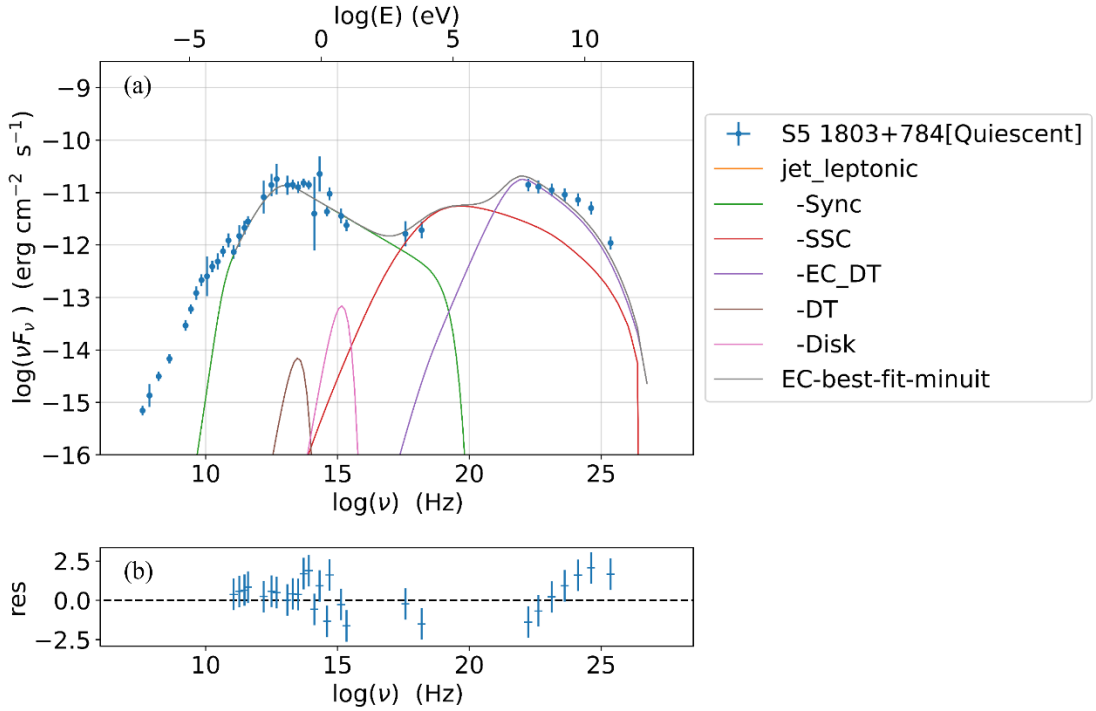


Figure 5.7: (a) S5 1803+784 broadband SED (Quiescent state, best-fit SSC+EC model); (b) Residual of the fit.

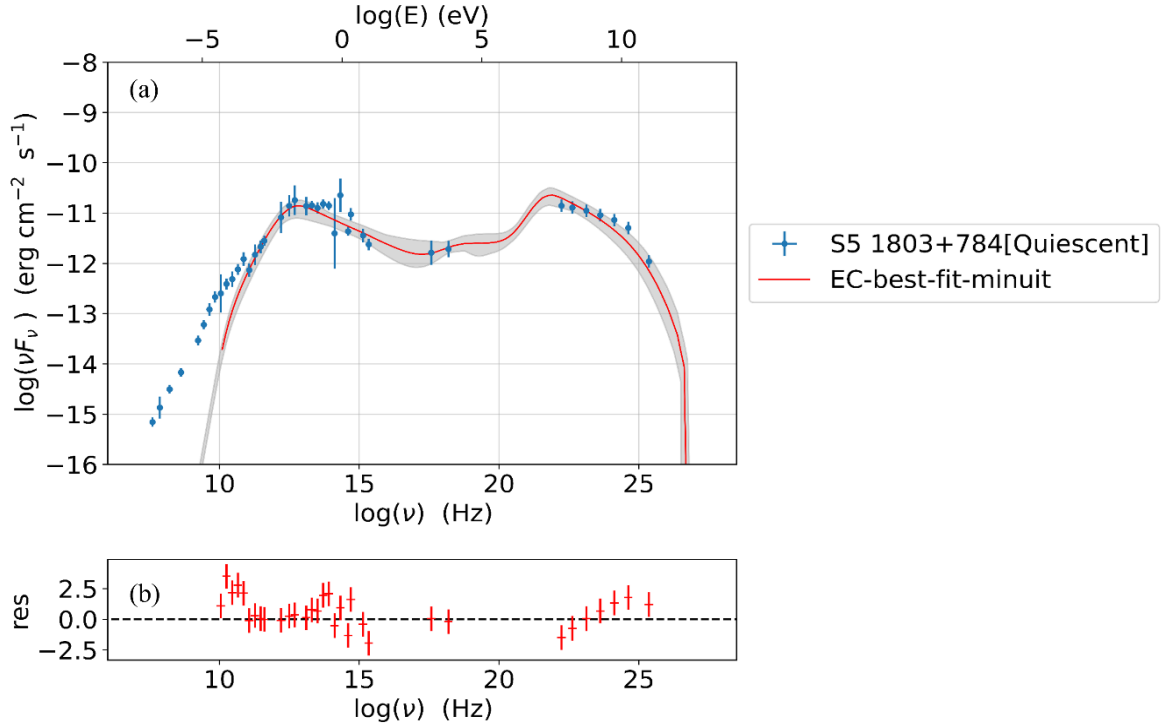


Figure 5.8: S5 1803+784 broadband SED (Quiescent state, best-fit SSC+EC model), where the shaded area is the upper and the lower bounds of the MCMC sampling; (b)Residual.

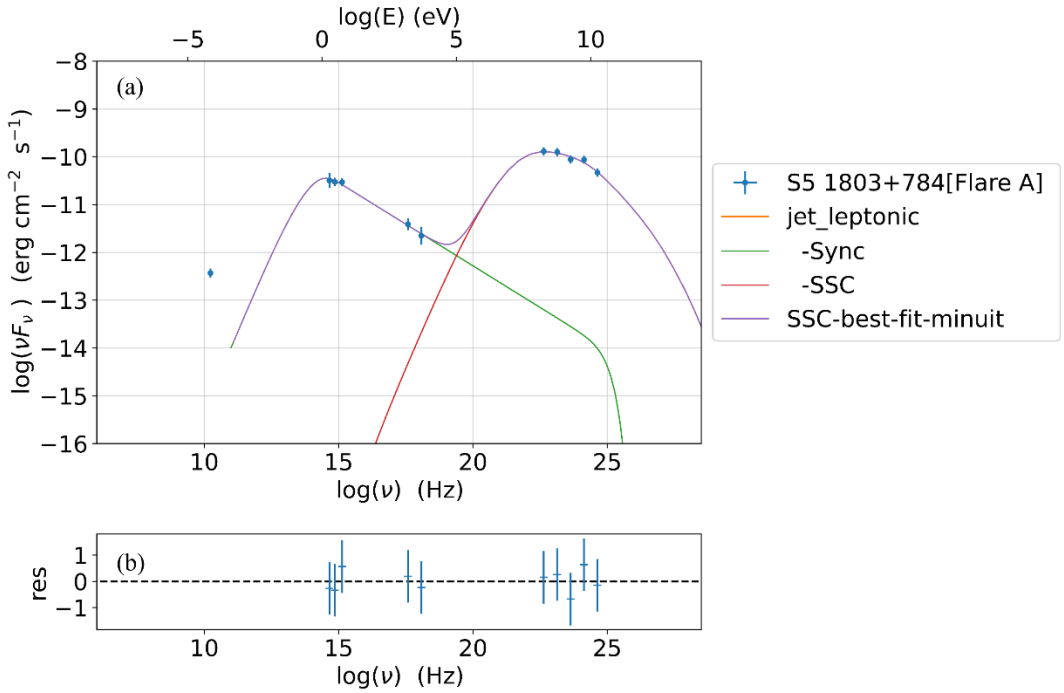


Figure 5.9: (a) S5 1803+784 broadband SED (Flare A, best-fit SSC model); (b) Residual of the fit.

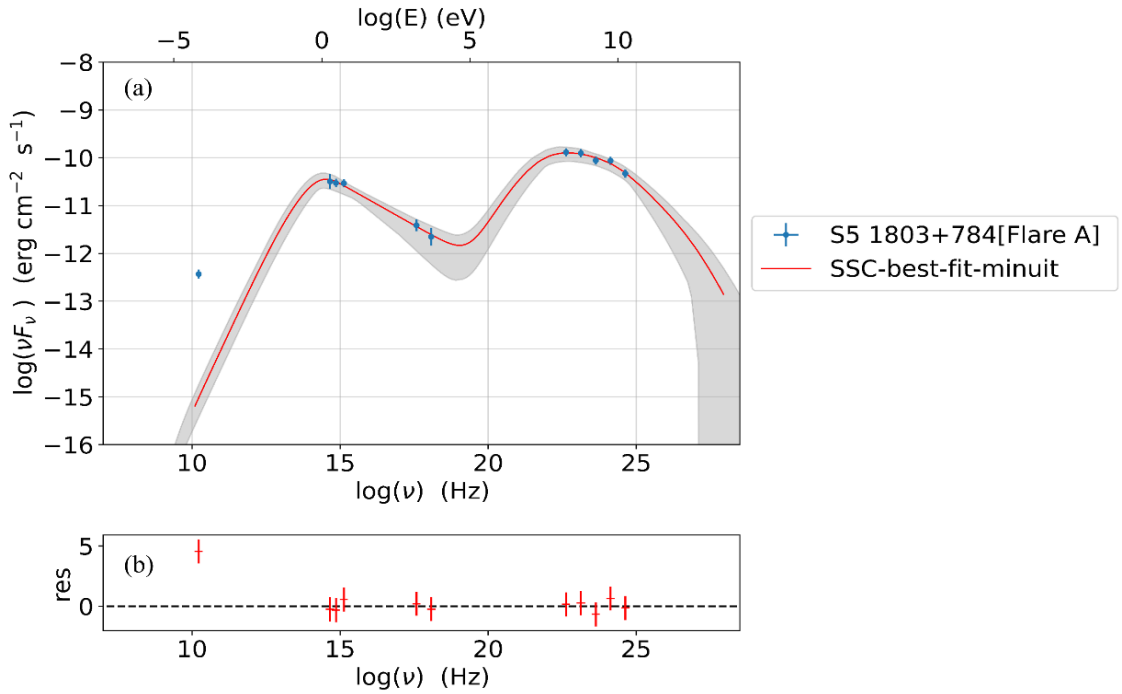


Figure 5.10: (a) S5 1803+784 broadband SED (Flare A, best-fit SSC model), where the shaded area is the upper and the lower bounds of the MCMC sampling; (b) Residual of the fit.

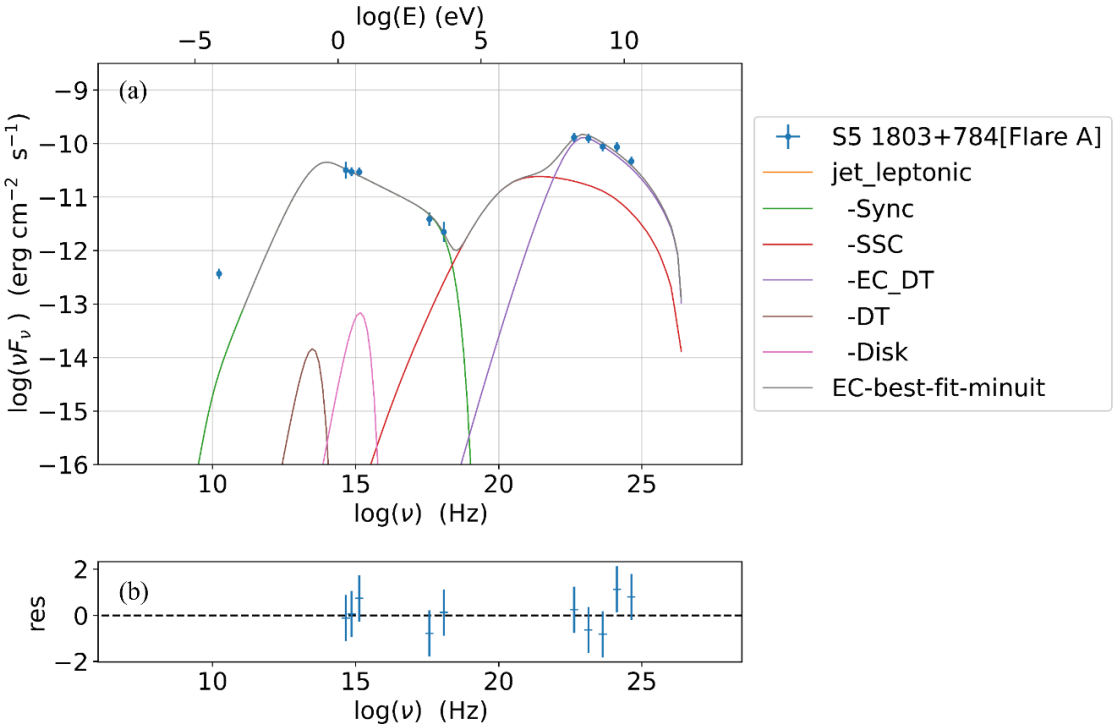


Figure 5.11: (a) S5 1803+784 broadband SED (Flare A, best-fit SSC+EC model); (b) Residual of the fit.

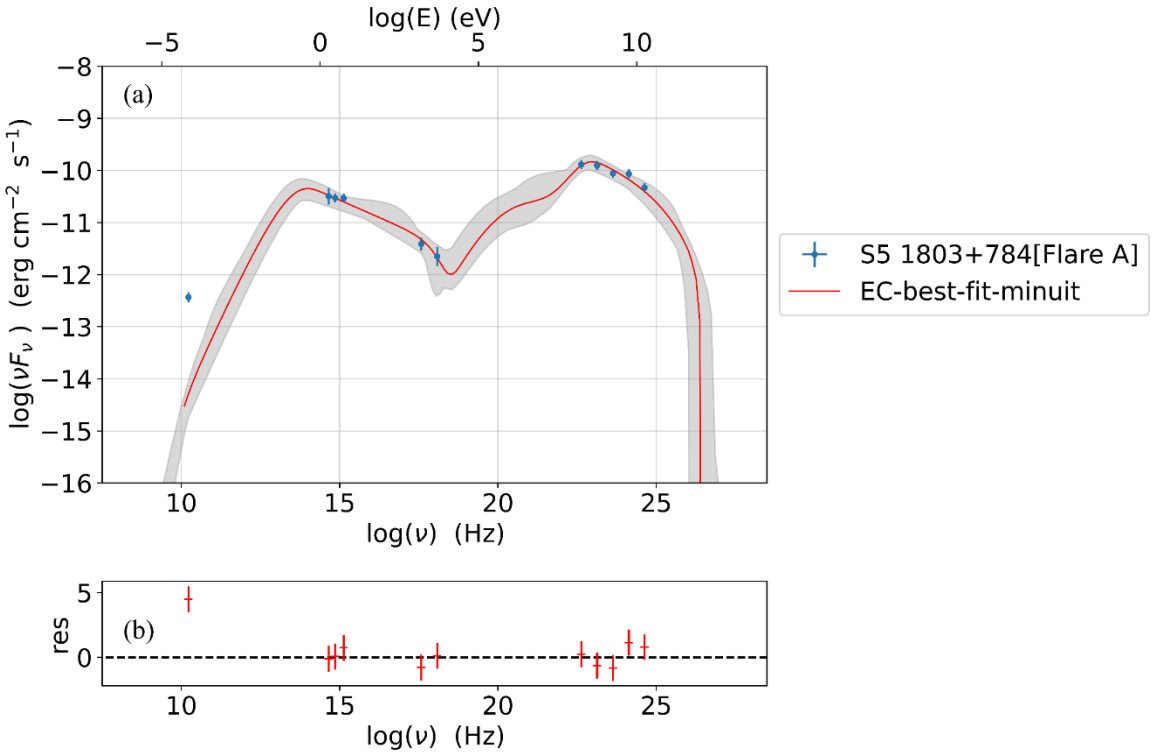


Figure 5.12: (a) S5 1803+784 broadband SED (Flare A, best-fit SSC+EC model), where the shaded area is the upper and the lower bounds of the MCMC sampling; (b) Residual of the fit.

Table 5.5: SSC+EC leptonic model parameters fixed in the quiescent state.

Symbol (unit)	Description	Value
$R_H \times 10^{17}$cm	Emitting region distance from the BH	5.00
$L_{Disk} \times 10^{44}$ erg/s	Disk luminosity	2.12
$R_{DT} \times 10^{18}$ cm	Radius of the dusty torus	1.15
$T_{Disk} \times 10^{4}$ K	Disk temperature	3.02
τ_{DT}	Fraction of disk photons re-emitted from the DT	0.1
T_{DT}(K)	Temperature of the dusty torus	655

Table 5.6: Best fit parameters of S5 1803+784 for the quiescent state, SSC only and SSC+EC model.

Symbol (unit)	Description	Quiescent (SSC)	Quiescent (SSC+EC)
$\gamma_b \times 10^3$	Turn-over-energy Lorentz factor	$0.87^{+0.07}_{-0.07}$	$0.72^{+0.06}_{-0.05}$
p	Low energy spectral slope	$2.28^{+0.11}_{-0.24}$	$1.62^{+0.11}_{-0.12}$
p_1	High energy spectral slope	$3.77^{+0.11}_{-0.13}$	$3.58^{+0.13}_{-0.11}$
γ_{min}	Low-energy-cut-off Lorentz factor	$13.38^{+0.89}_{-1.00}$	$14.74^{+0.89}_{-0.82}$
$\gamma_{max} \times 10^5$	High-energy-cut-off Lorentz factor	$9.07\ ^{+0.25}_{-0.68}$	$8.26\ ^{+0.19}_{-0.13}$
R (cm) $\times 10^{16}$	Emitting region size	$31.62\ ^{+0.40}_{-1.13}$	$10.39\ ^{+1.81}_{-1.64}$
δ	Doppler factor	$12.20^{+0.00}_{-0.00}$	$12.20^{+0.00}_{-0.00}$
B (G)	Magnetic field	$0.26^{+0.01}_{-0.01}$	$0.36^{+0.03}_{-0.03}$
N (cm^{-3})	Emitter density	$3.08^{+0.39}_{-0.25}$	$5.10^{+0.32}_{-0.29}$
χ^2/dof	Chi-square/degrees of freedom	29.03/19	29.69/18

As stated earlier, the SED low energy hump is due to synchrotron radiation. The high-energy hump is due to inverse Compton scattering, either SSC or SSC+EC. The SSC model requires $\gamma_{max} = 9.3 \times 10^8$ during Flare A, which is physically implausible. Therefore, the additional EC component of the SSC+EC model is necessary to describe the emission process during the flare and, therefore, in the quiescent state.

Both models showed an increase in the Doppler factors to more than twice the quiescent state value.

Table 5.7: Best fit parameters of S5 1803+784 SSC only and SSC+EC leptonic model.

Symbol (unit)	Description	Flare A (SSC)	Flare A (SSC+EC)
$\gamma_b \times 10^3$	Turn-over-energy Lorentz factor	$4.65^{+0.59}_{-0.38}$	$1.36^{+0.03}_{-0.03}$
p	Low energy spectral slope	$1.71^{+0.08}_{-0.09}$	$1.87^{+0.08}_{-0.08}$
p_1	High energy spectral slope	$3.61^{+0.15}_{-0.11}$	$3.54^{+0.10}_{-0.09}$
γ_{min}	Low-energy-cut-off Lorentz factor	$867.85^{+1.93}_{-3.78}$	$32.31^{+1.93}_{-3.78}$
$\gamma_{max} \times 10^5$	High-energy-cut-off Lorentz factor	$9306.56\ ^{+1575.43}_{-1763.35}$	$9.56\ ^{+0.37}_{-1.20}$
R (cm) $\times 10^{16}$	Emitting region size	$3.42\ ^{+0.00}_{-0.00}$	$3.42\ ^{+0.00}_{-0.00}$
δ	Doppler factor	$25.70^{+2.41}_{-1.91}$	$26.07^{+2.41}_{-1.91}$
B (G)	Magnetic field	$0.13^{+0.01}_{-0.01}$	$0.37^{+0.01}_{-0.01}$
N (cm^{-3})	Emitter density	$8.16^{+1.01}_{-1.03}$	$11.59^{+3.35}_{-2.64}$
χ^2/dof	Chi-square/degrees of freedom	$1.56/2$	$4.21/2$

The Doppler factors of the two models are within the same range and just a bit higher than previously observed from this blazar (Liodakis et al., 2018). The best fit magnetic field of the SSC model in both states (flare and quiescent) is between 0.13G and 0.26 G, and that of the EC+ SSC model is between 0.36 G and 0.37 G. There is an increase in the minimum (γ_{min}) and the maximum (γ_{max}) energies of the electrons during the flare. The increase in γ_{min} is more pronounced in both models, increasing by a factor > 2 in the SSC+EC even though the SSC model has a higher γ_{min} than the SSC+EC model in both states; this is usually the case with the SSC models of most LSPs (Cerruti, 2020). The emission can be modelled as synchrotron+SSC-only but requires unusually high Lorentz factors. An external Compton component produces more physically plausible parameters.

5.1.4 Phenomenological spectral best fits of S5 1803+784

We perform MCMC sampling of the best-fit parameters to obtain the 16th and 84th percentile upper and lower bounds of those parameters. The best-fit parameters using the Minuit minimizer and the MCMC sampler agree, as reported in Figures 5.6,5.8, 5.10, and 5.12.

The F-test is calculated for the quiescent state SEDs of both models using the relation below:

$$F = \frac{\left(\chi^2_{\mathrm{SSC+EC}} - \chi^2_{\mathrm{SSC-only}}\right)/\left(\mathrm{dof}_{\mathrm{SSC-only}} - \mathrm{dof}_{\mathrm{SSC+EC}}\right)}{\chi^2_{\mathrm{SSC-only}}/\mathrm{dof}_{\mathrm{SSC-only}}}$$

The F-value is 6.65, corresponding to a p-value of 7.18×10^{-5}; therefore, the improvement in the fit to the SSC+EC model is well above what would be expected solely due to the additional parameters.

5.2 Gamma-ray emission and acceleration processes in S5 1803+784

The SED of S5 1803+784 is well-fit by the SSC+EC leptonic model. Under this assumption, the X-ray emission comes from the upper tail of the synchrotron emission during the flare. In contrast, the X-ray emission is dominated by the low-energy end of the inverse Compton component during the quiescent state. This flare is the first time such a scenario has been reported from S5 1803+784. The SSC-only leptonic model was able to fit the SED without requiring external photons from the dusty torus for the gamma-ray emission during previous flares (e.g., Priya *et al.*, 2022). Aside from the EC component, the parameters of the SED model of the flares in Table 5.6 are comparable with previous models (Tavecchio *et al.*, 2010). The day scale variability and the very high broadband radiation observed from the source both in X-ray and gamma-ray on April 12, 2020, are features consistent with enhanced particle acceleration through magnetic dissipation in which reconnection occurs during the flares (e.g., Sironi, Petropoulou and Giannios, 2015). The hard power law in the low-energy spectral slope of the SED model is consistent with magnetic reconnection (e.g., Guo *et al.*, 2014).

The energy densities in the rest frame of the emitting region of the blazar are estimated in the SED modeling.

Here, U_e, and U_B are the energy densities of the leptonic particles and the magnetic field in the emitting region rest frame, respectively (Table 5.8).

Table 5.8: Emitting region energy densities of S5 1803+784 during Flare A.

$U_e \times 10^{-2}$ erg cm^{-3}	$U_B \times 10^{-3}$erg cm^{-3}
1.346	5.672

The emitting region is particle-dominated in this flare, with $\mathrm{U}_B/\mathrm{U}_e = 0.42$. Here most of the magnetic energy has been dissipated into particle kinetic energy.

CHAPTER 6

6.0 Recent flares of BL Lacertae (4FGL J2202.7+4216)

BL Lacertae has been classified as both a low-synchrotron peaked (LSP) (synchrotron frequency peak $\nu_{syn} < 10^{14}$Hz) (Nilsson *et al.*, 2018) and an ISP (Ackermann *et al.*, 2011) BL Lac object because the synchrotron peak frequency (ν_p) falls between 10^{14}Hz and 10^{15}Hz. BL Lacertae has been a target of several multi-wavelength studies because of its variability in a wide energy range. It is the only BL Lac detected in sub-hour variability, which challenges existing standard models of blazar variability (Acciari *et al.*, 2019). BL Lacertae SED has been modelled with external photons reprocessed from the BLR (Böttcher *et al.*, 2013). Several theoretical models can be used to explain the complicated flux variability observed from BL Lacertae and to fit the SED of the blazar (Acciari *et al.*, 2019). Here we present phenomenological spectral fits to the observed fluxes during the recent outburst from 2020 August to 2021August in the framework of the leptonic jet model.

6.1 BL Lacertae flares of 2020 August to 2021 August

Fermi-LAT observed gamma-ray flaring activity from BL Lacertae (Abdollahi *et al.*, 2020) starting from August 14 (MJD 59075). The highest daily flux peak yet observed from BL Lacertae was observed on October 6, 2020 (MJD 59128) (Cheung, 2020; Mereu, 2020), and the flux continued to increase to $(64.86 \pm 3.16) \times 10^{-7}$ cm^{-2}s^{-1} on April 27, 2021 (MJD 59331). The daily binned light curve and the Bayesian blocks used to define the flares are shown in Figure 6.1 and compared with 12-hourly binned in Figure 6.2.

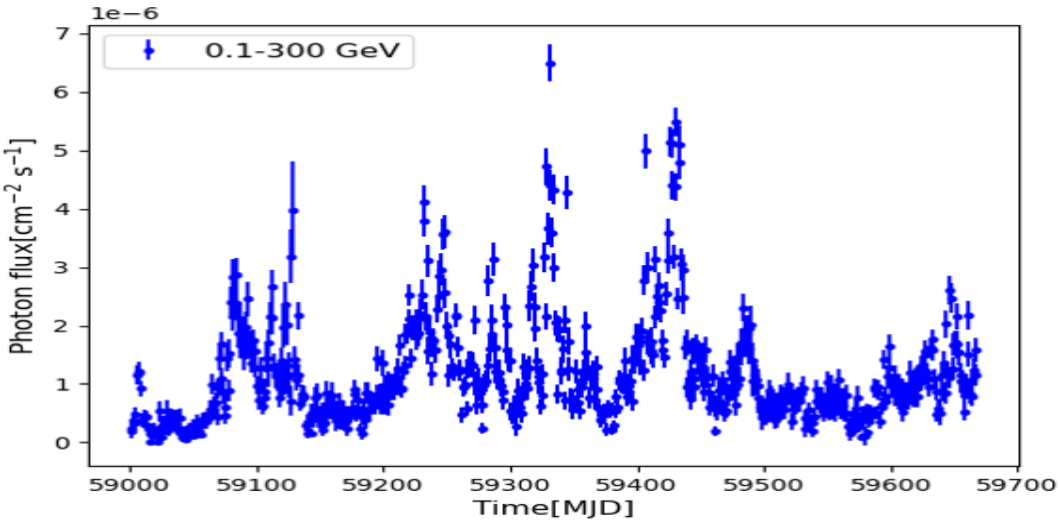


Figure 6.1: The daily binned light curve of BL Lacertae at 0.1-300 GeV during the flare.

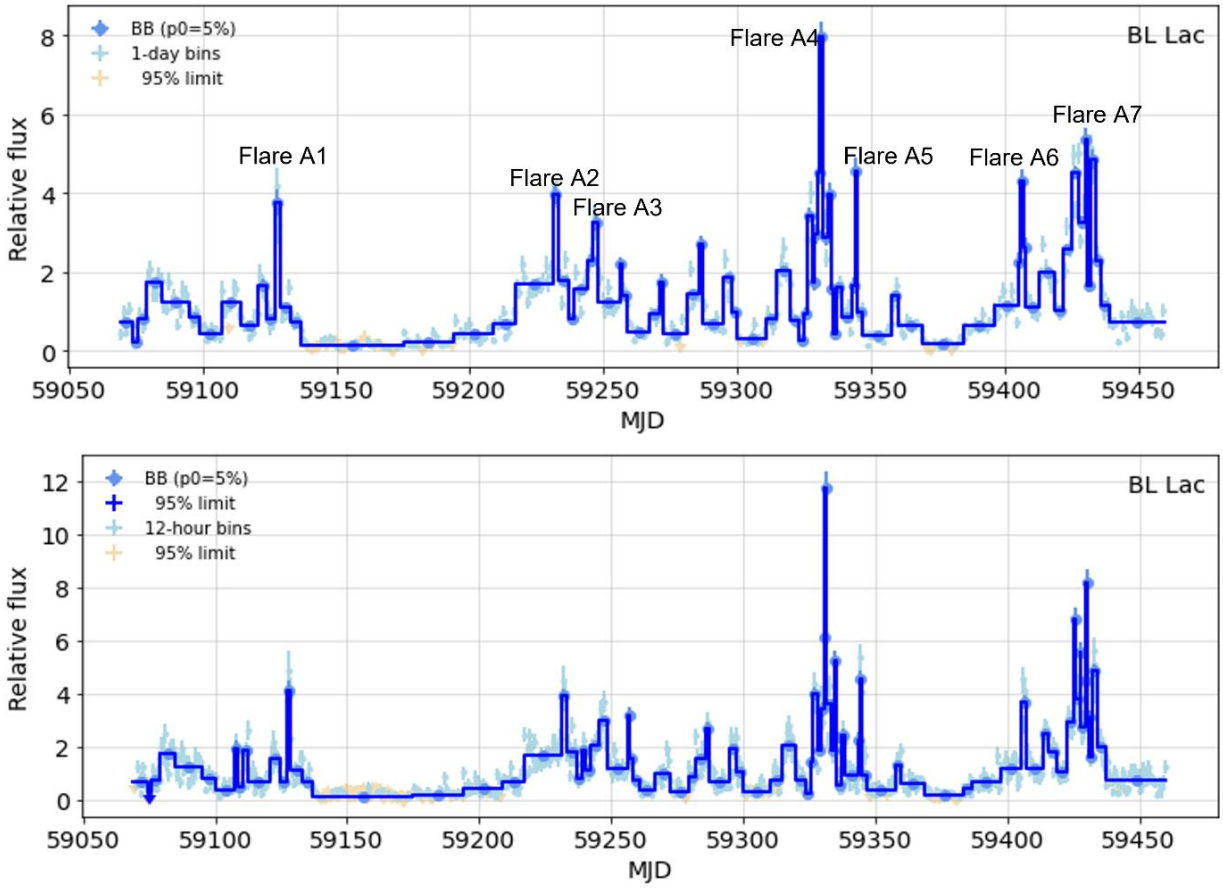


Figure 6.2: Bayesian blocks light curve (LC) (0.1-300 GeV) of BL Lacertae during the 2020 and 2021 flares in daily bins (upper panel) compared with 12-hourly binned *Fermi*-LAT light curve (lower panel).

For Flare A1, simultaneous (July 30, 2020, to August 30, 2021) radio data was obtained upon request from Aalto University Metsähovi Radio Observatory 37GHz radio telescope, and simultaneous UV/optical and X-ray data from Swift/UVOT and the Swift/XRT (D'Ammando, 2020, 2022) were used to build the broadband SED.

6.1.1. BL Lacertae gamma-ray spectra and characteristics during the 2020 to 2021 flares

All the flares are well described with the log parabola (LP) spectrum (see Tables 6.2 and 6.3 for the test statistics comparison with the power-law (PL) and broken power law (BPL) spectral models). The seven flares (A1, A2, A3, A4, A5, A6, and A7) have similar gamma-ray spectra except for Flare A6, which is the least curved. The gamma-ray spectra of the flares are plotted in Figure 6.3, and their characteristics are shown in Table 6.1, with Flare A5 having a harder gamma-ray spectral index.

Table 6.1: Spectral characteristics of the gamma-ray spectra during the flares using the log parabolic distribution.

BL Lacertae Flares	Label	Peak Flux (10^{-7} cm^{-2}s^{-1})	α	β	N_0 (10^{-11}MeV^{-1} cm^{-2}s^{-1})	E_b (MeV)	TS
	Flare A1	39.77 ±8.35	1.92±0.03	0.069±0.02	27.60±0.98	726.7	3258.81
	Flare A2	41.23±2.83	1.93±0.02	0.052±0.01	44.32±0.83	726.7	12258.42
	Flare A3	36.07±2.89	1.93±0.02	0.032±0.01	50.20±1.49	726.7	5305.03
	Flare A4	64.86± 3.16	1.92±0.02	0.034±0.01	99.40±2.54	726.7	7710.40
	Flare A5	42.78±2.91	1.88±0.04	0.054±0.03	61.90±5.02	726.7	1621.41
	Flare A6	49.84±2.99	1.98±0.03	0.015±0.01	43.00±1.39	726.7	4333.99
	Flare A7	54.76±2.46	1.98±0.01	0.035±0.01	89.70±1.56	726.7	14704.97

Table 6.2: Comparison of the gamma-ray spectra models for BL Lacertae.

Flare Label	TS(BPL)	TS (LP)	TS(PL)	TS_{curve}
Flare A1	3255.41	3258.81	3206.89	51.92
Flare A2	11900.05	12258.42	11827.25	431.17
Flare A3	5224.84	5305.03	5182.28	122.75
Flare A4	7415.50	7710.40	7248.54	461.86
Flare A5	1621.19	1621.41	1617.71	3.70
Flare A6	4295.93	4333.99	4190.42	143.57
Flare A7	14704.97	14770.72	14387.32	383.40

The TS_{curve} of all the flares show a statistical significance $> 4\sigma$ (Mattox *et al.,* 2006; Nolan *et al.,* 2016) except for Flare A5, for which the additional parameters beyond the power-law (PL) do not provide a statistically significant improvement (Table 6.2). The highly curved spectra are probably due to the Klein-Nishina effect on the inverse Compton up-scattered re-emitted disk photons from the BLR by the relativistic electrons in the jet (Rajput and Pandey, 2021). The curvature could also be due to the intrinsic energy distribution of the emitting leptonic particles (e.g., Tramacere *et al.*, 2009).

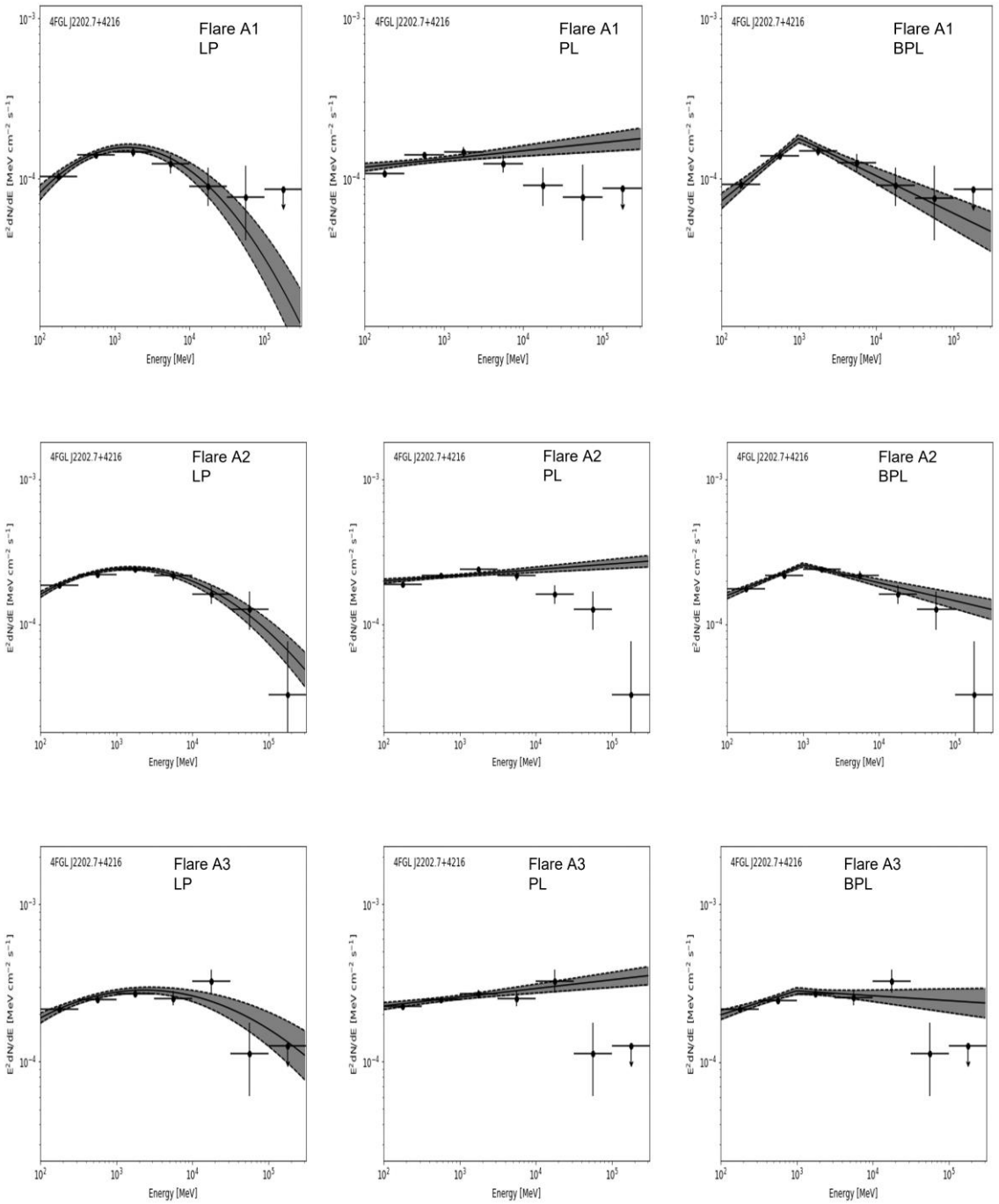


Figure 6.3: The gamma-ray spectra of the BL Lacertae flares fitted with three spectral models (continued on the next page).

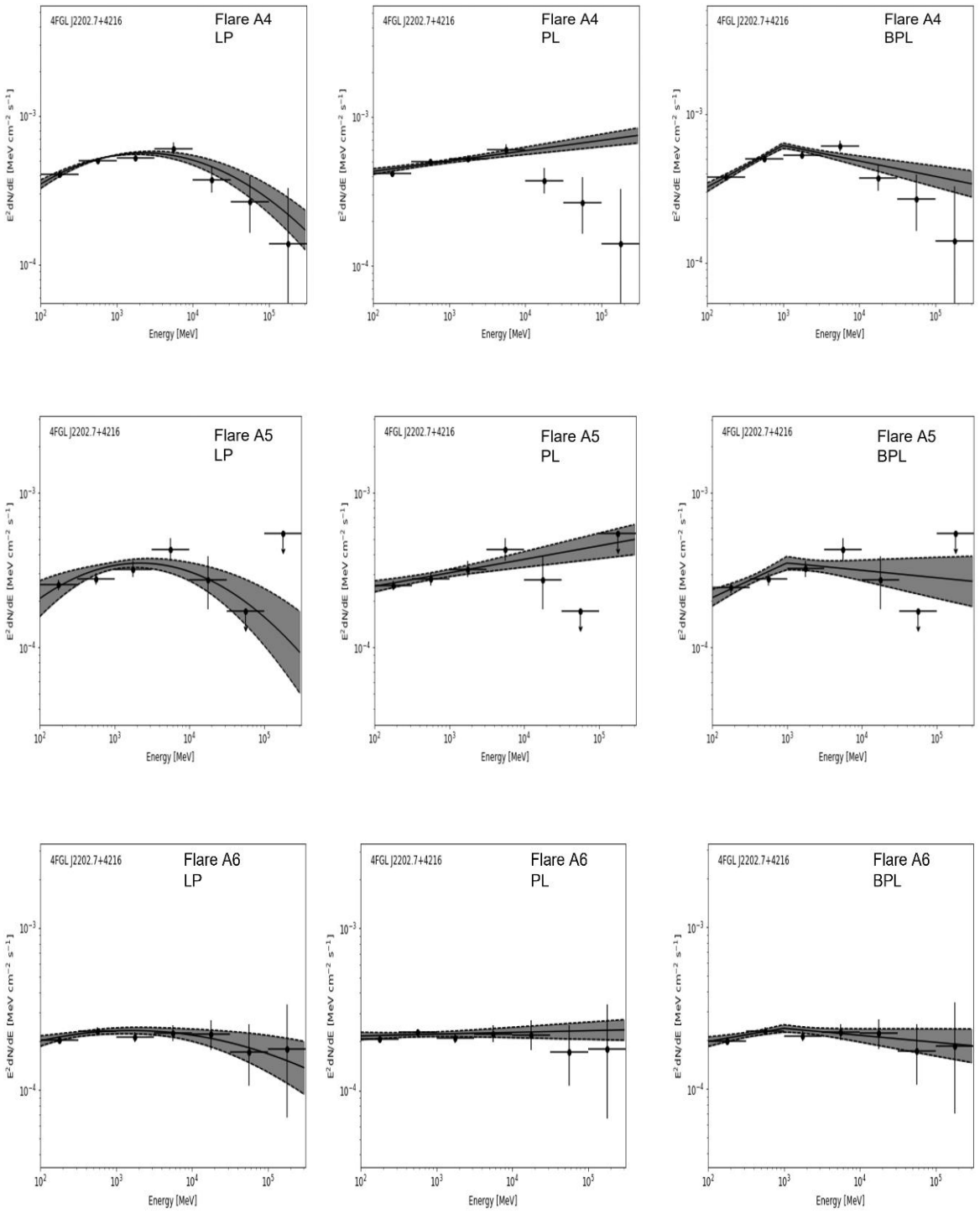


Figure 6.3: The gamma-ray spectra of the BL Lacertae flares fitted with three spectral models (continued on the next page).

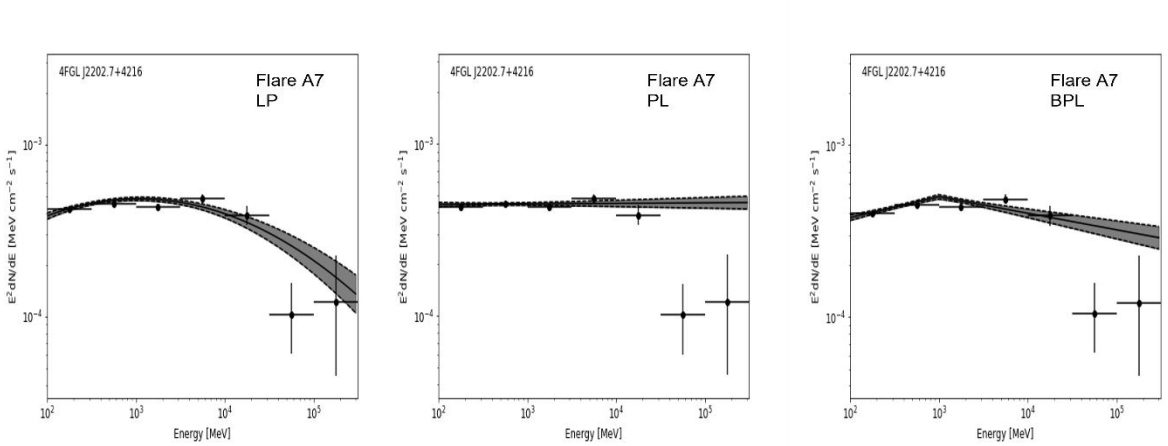


Figure 6.3: The gamma-ray spectra of the BL Lacertae flares. The data points are fitted with three spectral models.

Table 6.3: Comparison of the gamma-ray spectral parameters of the log parabola (LP) distribution function for the two blazars. LT is the long-term SED from 2008/08/04-2022/03/30; FT is the 2020-2021 flare period, and Flare A1 is defined previously.

MJD	α	β	N_0 (10^{-11}MeV^{-1} cm^{-2}s^{-1})	E_b (MeV)	TS
54682-59668 (LT)	2.08±0.01	0.040±0.01	8.78±0.04	726.7	194523.3
59124-59435 (FT)	2.00±0.01	0.040±0.01	23.86±0.14	726.7	123157.1
Flare A1	1.92±0.03	0.069±0.02	27.60±0.98	726.7	3258.81

BL Lacertae has a harder spectrum and a higher spectral curvature during Flare A1.

6.1.2 Temporal characteristics of BL Lacertae during the 2020 and 2021 flares

The durations of Flares A1, A2, A3, A4, A5, A6, and A7 in the observer frame $t_d \cong 2(t_r + t_f)$ are ~4.5 days, ~9.2 days, ~12.28 days, ~5.7 days, ~2.1 days, ~5.6 days, and ~25.5 days, respectively (Table 6.4 and Figure 6.4). The flares were also tested for symmetry; the symmetric profiles are ε_{A1} = -0.80, ε_{A2} = 0.69, ε_{A3} = 0.63, ε_{A4} = 0.15, ε_{A5} = -0.81, ε_{A6} = -0.76, and ε_{A7} = -0.63; all the flares have asymmetric profiles except Flare A4, which is symmetric according to the definition in Abdo *et al.* (2010). Flare A5 has the shortest duration in the observer frame. Flare A1 has a fast rise time and is highly asymmetric, consistent with a sudden injection of accelerated particles in the emitting region during the flare resulting in the

outburst observed on October 6, 2020, across the observed electromagnetic spectrum.

Table 6.4: Temporal characteristics of BL Lacertae during the 2020 and 2021 flares.

Label	t_r (day)	t_f (day)	t_0 (MJD of peak flux)	$F_c(\times 10^{-7}$ cm^{-2}s$^{-1})$	$F_0(\times 10^{-7}$ cm^{-2}s$^{-1})$
Flare A1	0.22	2.01	59128	11.58±3.88	39.77 ±8.35
Flare A2	3.87	0.72	59233	18.06±2.15	41.23±2.83
Flare A3	4.99	1.15	59248	15.75±1.97	36.07±2.89
Flare A4	1.62	1.21	59331	21.55±2.20	64.86± 3.16
Flare A5	0.10	0.94	59343	7.16±1.58	42.78±2.91
Flare A6	0.34	2.44	59406	12.42±1.85	49.84±2.99
Flare A7	2.35	10.42	59431	14.51±1.78	54.76±2.46

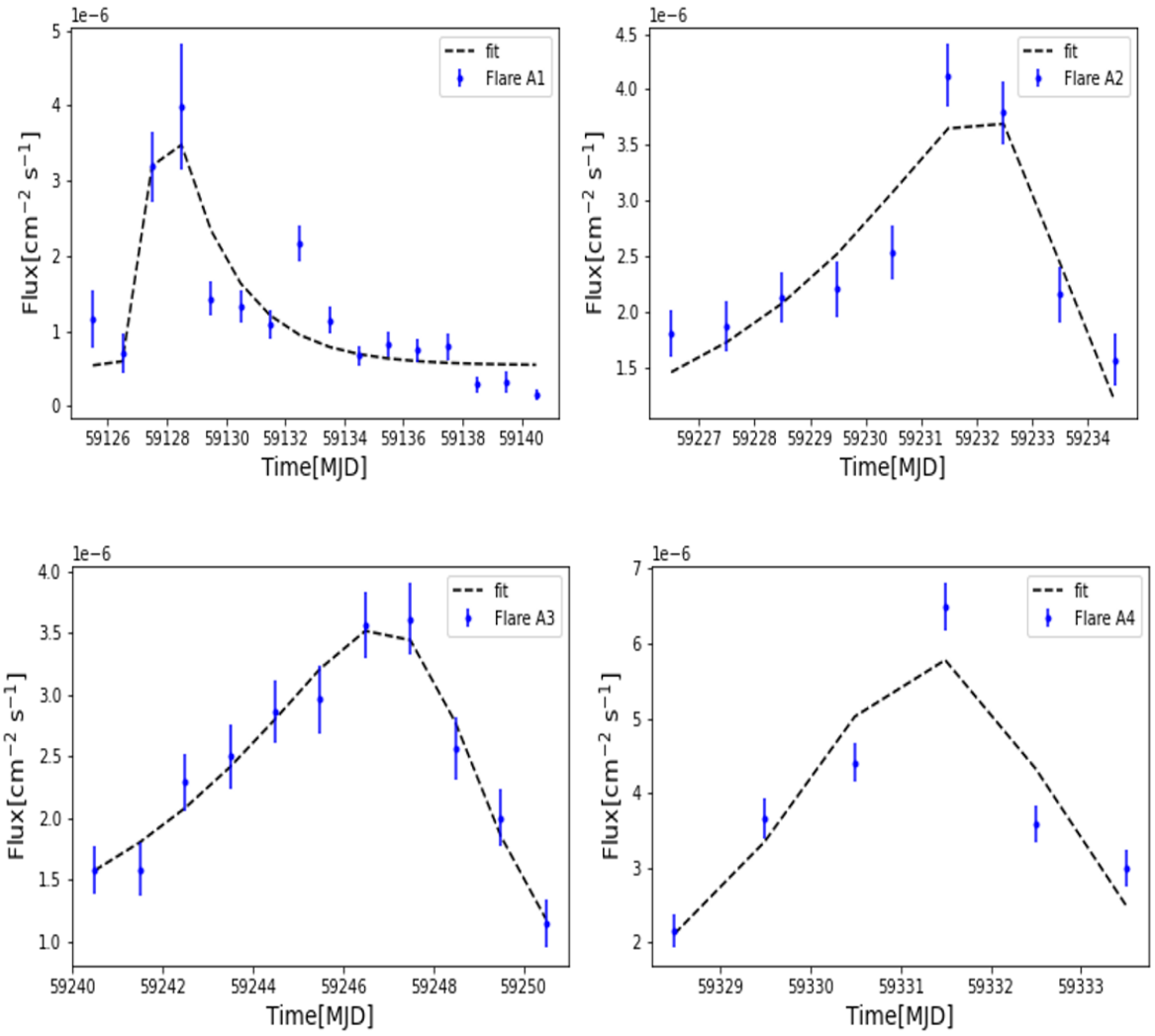


Figure 6.4: The temporal profiles of the flares fitted with the function in Equation 3.6 (continued on the next page).

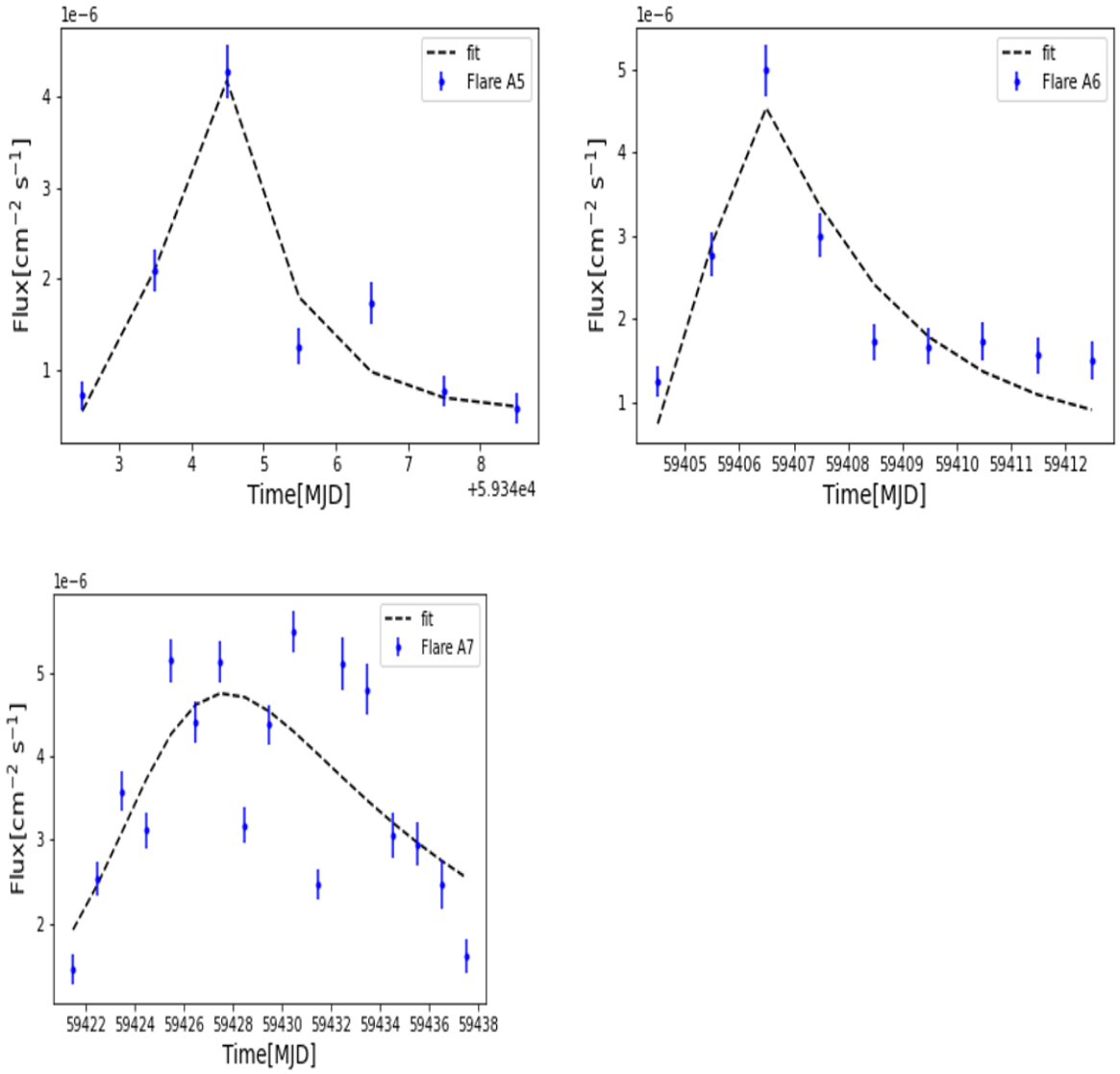


Figure 6.4: Temporal profile of the flares, each fitted with the function in Equation 3.6

6.2 Multiwavelength SED model of BL Lacertae using simultaneous data

In the SED of Flare A1, we make use of multiwavelength X-ray data obtained from Swift/XRT (Table 3.5 and Figure 6.5), the Nuclear Spectroscopic Telescope Array (NuSTAR), and the Neutron star Interior Composition Explorer (NICER) as discussed in Section 3.6.2. The X-ray fluxes measured by these telescopes were analyzed and corrected for galactic extinction (D'Ammando, 2022). We used the decay time to estimate the size of the emitting region. Flare A1 has a rise time (t_r) of ~0.22 day and decay time (t_f) of ~2.01 days (Table 6.4). A Doppler factor (δ) of 7.3, as seen from VLBI observations of BL Lacertae (Hovatta *et al.*, 2009), could not produce a good fit to the quiescent state SED. We, therefore, allowed the Doppler factor to be a free parameter. We estimated the size of the emitting region during the flare using the

relation $R < c\delta t_{var}/(1+z)$, where $t_{var} = t_r \ln 2$, assuming the Doppler factor above, and found R to be $< 2.70 \times 10^{15}$ cm. Furthermore, the distance of the emitting region from the black hole (R_H) can be constrained using the relation $R_H \sim 2c\Gamma^2\, t_{var}/(1+z)$, where Γ is the bulk Lorentz factor with estimated value of 11.60 (Hovatta *et al.*, 2009), resulting in a distance $R_H = 1.37 \times 10^{17}$cm. Using Equation 3.2, the flux doubling time of the X-ray emission in Table 3.5 is 0.24 days between MJD 59127.6383 and MJD 59128.1827, consistent with the flare rise time (t_r) in the gamma-ray band. This implies that the gamma-ray and X-ray emissions are from the same emitting region.

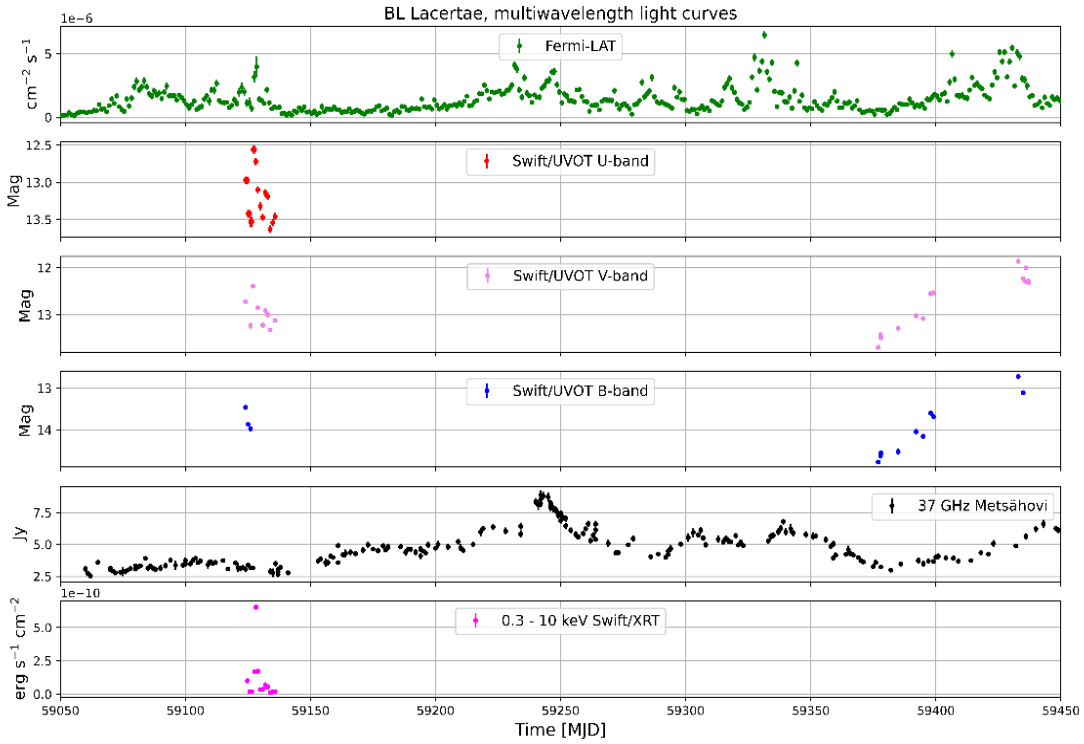


Figure 6.5: Multiwavelength light curves of BL Lacertae during the 2020 and 2021 flaring periods.

Several authors have used various models, both analytical and numerical, to explain the very short timescale variability observed in BL Lacertae. For example, Morris, Potter, and Cotter, (2019) used numerical simulations to demonstrate that plasmoids undergoing magnetic reconnection can reproduce the light curve of the 2016 BL Lacertae flares. However, they overproduce the synchrotron radiation in a single-zone SSC model, suggesting the possibility of external seed photons undergoing the inverse Compton scattering. Several multiwavelength

studies of BL Lacertae have been conducted due to the complex nature of the observed emission. The MAGIC Collaboration modelled the emission from BL Lacertae by assuming multiple emitting regions involving different scenarios mentioned in Subsection 2.3.1.1. They suggested that the BLR in BL Lacertae may be too weak to absorb the VHE gamma-rays but can provide additional seed photons to the inverse Compton scattering (Acciari *et al.,* 2019).
Using the multiwavelength data discussed in Chapter 3, we model the SED of BL Lacertae using the synchrotron+SSC-only leptonic model and SSC+EC model, assuming that the EC photons are disk photons absorbed and re-emitted by the BLR as UV/Optical photons. A broken power-law electrons distribution was assumed.
The jet parameters in Table 6.5 were obtained by fitting the broadband SED in *JetSeT,* and the values of the parameters are in agreement with the general properties of *Fermi*-LAT detected blazars (e.g., Ghisellini, 2010). The disk temperature (T_{Disk}) used is within the range used in previous studies, as is the disk luminosity (e. g. Raiteri *et al.*, 2009). We adopted the value of the fraction of the reprocessed disk photons from the BLR of 0.13 from a previous study (Böttcher *et al.*, 2013). The disk luminosity used in the flare SSC+EC model cannot fit the quiescent state; instead, a disk luminosity value of 8.79×10^{42} erg/s was used.

Table 6.5: SSC+EC jet structure parameters during the flare.

Symbol (unit)	Description	Value
$R_H \times 10^{17}$cm	Emitting region distance from the BH	1.37
$L_{Disk} \times 10^{44}$ erg/s	Disk luminosity	6.12
$R_{BLR-in} \times 10^{16}$cm	Inner radius of the BLR	0.95
$R_{BLR-out} \times 10^{16}$cm	Outer radius of the BLR	1.91
$T_{Disk} \times 10^4$ K	Disk temperature	3.02
τ_{BLR}	Fraction of disk photons re-emitted from the BLR	0.13

Table 6.6: SSC only and SSC+EC quiescent state best-fit parameters.

Symbol (unit)	Description	Quiescent (SSC)	Quiescent(SSC+EC)
$\gamma_b \times 10^3$	Turn-over-energy Lorentz factor	$9.76^{+0.23}_{-0.23}$	$8.92^{+0.02}_{-0.02}$
p	Low energy spectral slope	$1.85^{+0.01}_{-0.01}$	$1.86^{+0.031}_{-0.031}$
p_1	High energy spectral slope	$5.48^{+0.18}_{-0.18}$	$5.79^{+0.14}_{-0.15}$
γ_{min}	Low-energy-cut-off Lorentz factor	$20.62^{+0.06}_{-0.11}$	$98.25^{+9.31}_{-9.31}$
$\gamma_{max} \times 10^5$	High-energy-cut-off Lorentz factor	$1.07\ ^{+0.02}_{-0.02}$	$2.16\ ^{+0.007}_{-0.007}$
R (cm) $\times 10^{17}$	Emitting region size	$0.94\ ^{+0.02}_{-0.02}$	$0.68\ ^{+0.01}_{-0.01}$
δ	Doppler factor	$18.84^{+0.20}_{-0.20}$	$24.07^{+0.24}_{-0.58}$
B (G)	Magnetic field	$0.013^{+0.0001}_{-0.0001}$	$0.011^{+0.0002}_{-0.0002}$
N (cm^{-3})	Emitter density	$90.29^{+1.89}_{-1.89}$	$30.82^{+1.82}_{-2.50}$
χ^2/dof	Chi-square/degrees of freedom	$84.26/27$	$45.34/21$

Table 6.7: SSC only and SSC+EC Flare A1 best fit parameters.

Symbol (unit)	Description	Flare A1(SSC)	Flare A1(SSC+EC)
$\gamma_b \times 10^3$	Turn-over-energy Lorentz factor	$6.40^{+0.02}_{-0.02}$	$0.13^{+0.026}_{-0.030}$
p	Low energy spectral slope	$2.28^{+0.08}_{-0.09}$	$1.76^{+0.28}_{-0.14}$
p_1	High energy spectral slope	$2.92^{+0.01}_{-0.01}$	$2.95^{+0.10}_{-0.13}$
γ_{min}	Low-energy-cut-off Lorentz factor	$2.67^{+0.30}_{-0.30}$	$2.19^{+0.35}_{-0.14}$
$\gamma_{max} \times 10^5$	High-energy-cut-off Lorentz factor	$1.01\ ^{+0.04}_{-0.03}$	$0.57\ ^{+0.10}_{-0.09}$
R (cm) $\times 10^{17}$	Emitting region size	$5.93\ ^{+0.13}_{-0.13}$	$1.38\ ^{+0.001}_{-0.001}$
δ	Doppler factor	$20.17^{+0.43}_{-0.43}$	$26.58^{+1.50}_{-1.50}$
B (G)	Magnetic field	$0.02^{+0.00}_{-0.00}$	$0.07^{+0.01}_{-0.01}$
N (cm^{-3})	Emitter density	$9.93^{+0.77}_{-0.77}$	$144.18^{+39.32}_{-30.19}$
χ^2/dof	Chi-square/degrees of freedom	$5.34/5$	$5.10/5$

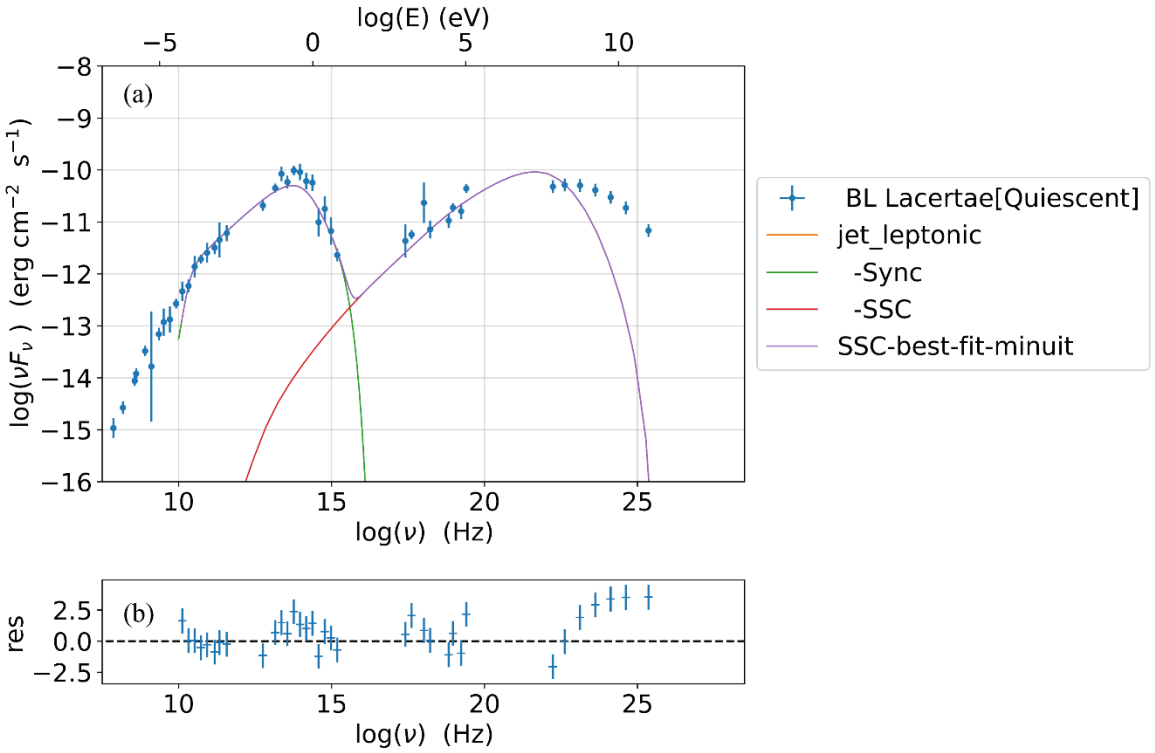


Figure 6.6: (a) BL Lacertae broadband SED (Quiescent state, best-fit SSC model); (b) Residual of the fit.

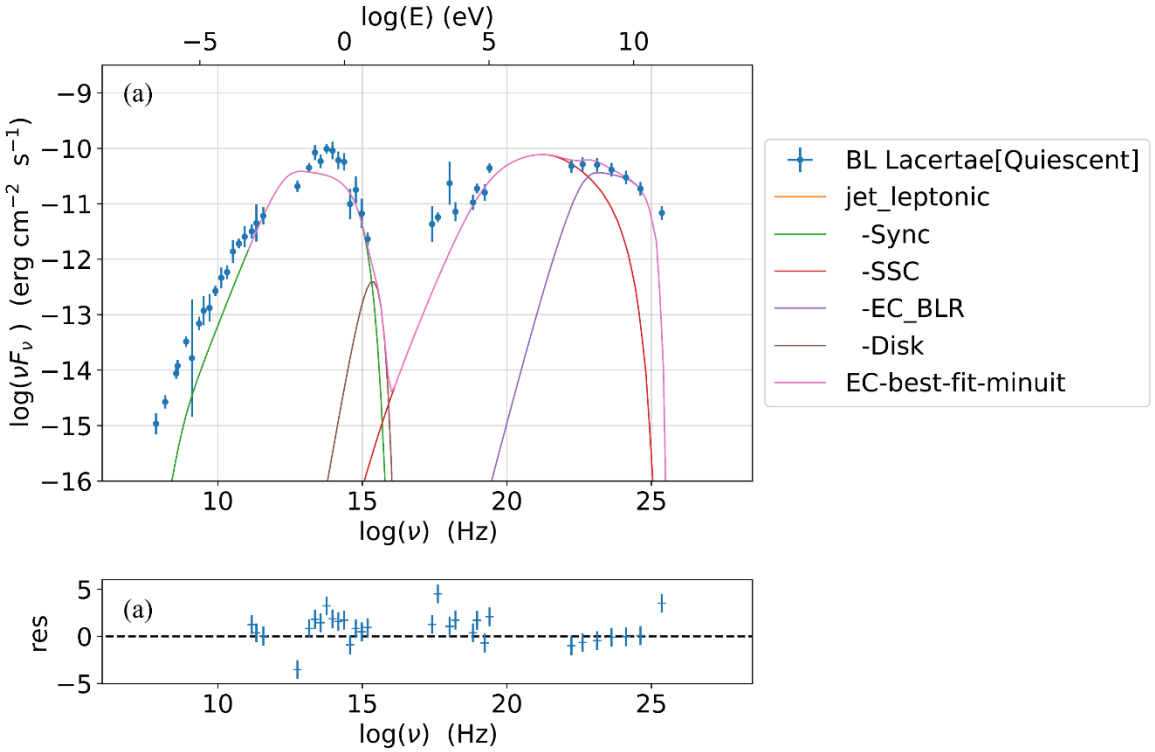


Figure 6.7: (a) BL Lacertae broadband SED (Quiescent state, best-fit SSC+EC model); (b) Residual of the fit.

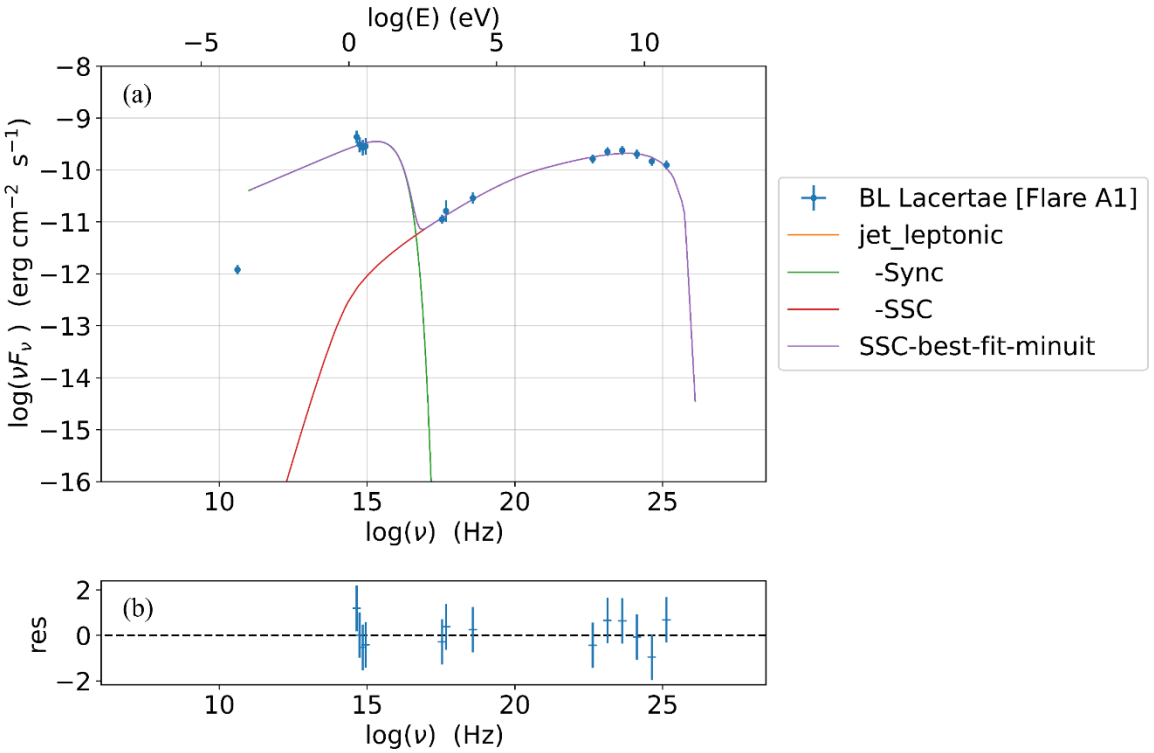


Figure 6.8: (a) BL Lacertae broadband SED (Flare A1, best-fit SSC model); (b) Residual of the fit.

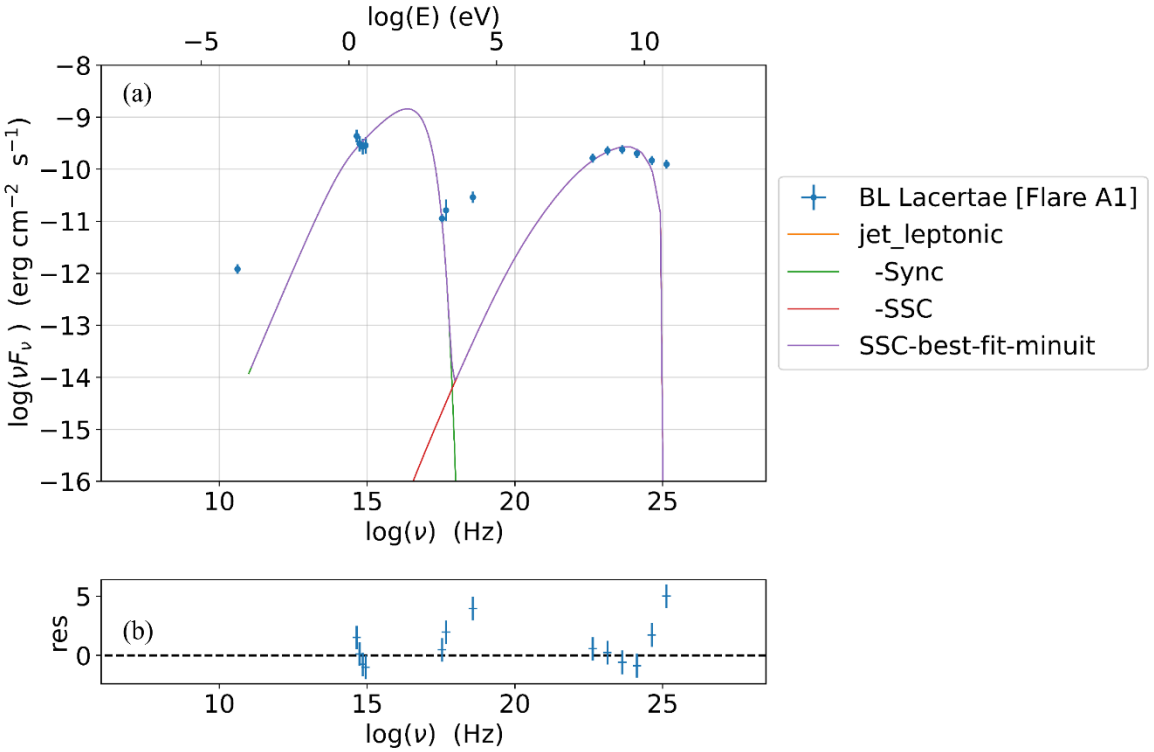


Figure 6.9: (a) BL Lacertae broadband SED (Flare A1, best-fit SSC model) using an emitting region size of 2.60×10^{15}cm as constrained by t_{var}; (b) Residual of the fit.

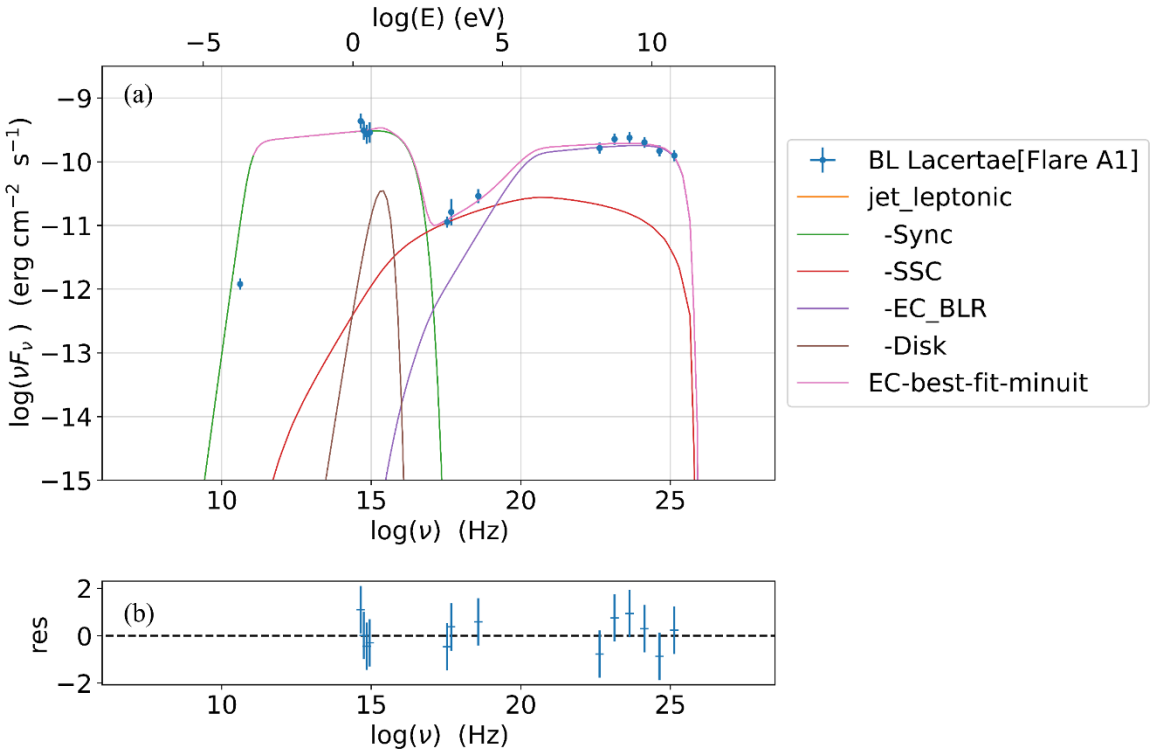
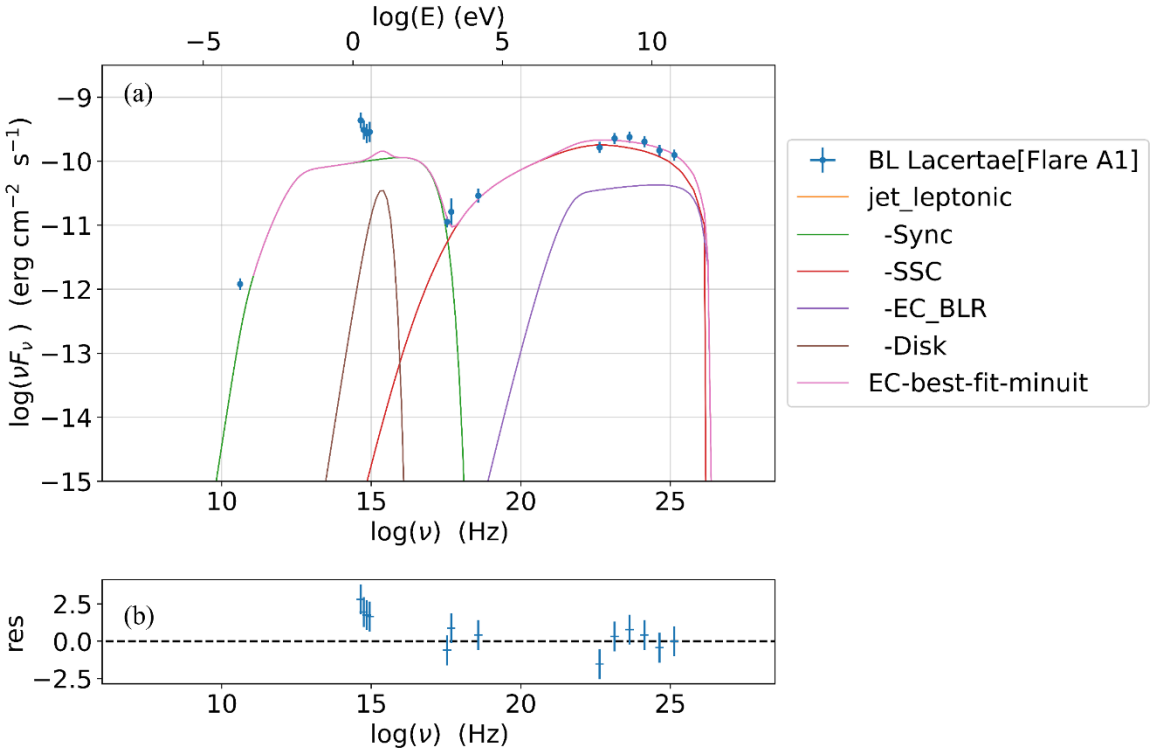


Figure 6.10: (a) BL Lacertae broadband SED (Flare A1, best-fit SSC+EC model); (b) Residual of the fit.



BL Lacertae broadband SED (Flare A1, best-fit SSC+EC model) using an emitting region size of 2.60×10^{15}cm as constrained by t_{var}; (b) Residual of the fit.

6.3 Implications for gamma-ray emission and the emitting region

The best-fit parameters and the reduced χ^2 suggest that the SSC and the external photons re-emitted from the BLR dominate the gamma-ray emission of BL Lacertae during the flare (Table 6.7); however, the single-zone model is a bad fit to the quiescent SED, even if an EC component is included.

BL Lacertae shows a variability time scale of less than a day during Flare A1, which was used to constrain the size of the emitting region to 2.70×10^{15} cm as shown in Figures 6.8, 6.9, 6.10, and 6.11. Neither the SSC-only nor the SSC+EC produces a good fit to the flare nor the quiescent SED with this region size; this could mean that the gamma-ray emitting zone is a smaller emitting blob within the emitting region, consistent with the jet-in-jet scenario of interacting emitting blobs in a reconnecting magnetic field (e.g., Giannios, 2013; Sironi and Spitkovsky, 2014; Sironi, Petropoulou and Giannios, 2015). The Doppler factors from the single-zone model are higher than the minimum Doppler factor estimated in Section 3.8 (Tables 6.6 and 6.7) during the flares and are also higher than the median value of 11 posited by Liodakis et al. (2018) and the value of 20.6 ± 8.4 in Cha et al. (2014).

The single-zone SSC emission model has successfully explained the spectral energy distribution (SED) and variability of many BL Lac objects. Still, there are others that require a different model to explain their unique spectral characteristics (e.g., Hervet, Boisson and Sol, 2015). The SED model fits of the emitting region beyond the BLR are feasible because the BLR is slightly optically thin. Therefore the emitting region outside the BLR will not suffer γ-γ absorption of VHE photons (e.g., Costamante *et al.*, 2018). This result also agrees with the suggestion of Morris et al. (2019) concerning the inclusion of external photons from the BLR. From the single-zone SEDs discussed above, it is clear that a two-zone model with external inverse Compton scattering should be considered for the BL Lacertae emission (a detailed discussion is in Chapter 7).

The quiescent state's lower disk luminosity and the higher disk luminosity during the flare also hint at the possibility of an accretion disk-jet interaction (e.g., Ghisellini *et al.*, 2014; Sbarrato, Padovani and Ghisellini, 2014).

The single-zone SED model returns the emitting region energy densities as given in Table 6.8.

Table 6.8: Emitting region energy densities within the BL Lacertae jet during Flare A1.

$U_e \times 10^{-3}$ erg cm^{-3}	$U_B \times 10^{-4}$erg cm^{-3}
2.819	2.088

The emitting region particle energy density during Flare A1 is higher than the magnetic energy density; this is consistent with magnetic dissipation during the flare in the emitting region with a transition from a magnetic-dominated emitting region to a kinetic-dominated emitting region.

CHAPTER 7

7.0 Results outlook

7.1 Implications of the single-zone fits to the multiwavelength SEDs with *JetSeT*

7.1.1 S5 1803+784

The emitting region intrinsic parameters in the quiescent and flaring states of S5 1803+784 in Table 7.1 show that Flare A coincides with the onset of a higher Doppler factor. The flare could be attributed to intrinsic changes consistent with the rearrangement of the magnetic field lines during magnetic reconnection in the emitting region, which drives the particle distribution and energy to higher Lorentz factors and causes the emitting region size to become more compact.

Table 7.1: Synchrotron+SSC and SSC+EC quiescent and flaring states best-fit parameters.

Symbol (unit)	Description	Quiescent (SSC)	Quiescent (SSC+EC)	Flare A (SSC+EC)
$\gamma_b \times 10^3$	Turn-over-energy Lorentz factor	$0.87^{+0.07}_{-0.07}$	$0.72^{+0.06}_{-0.05}$	$1.36^{+0.03}_{-0.03}$
p	Low energy spectral slope	$2.28^{+0.11}_{-0.24}$	$1.62^{+0.11}_{-0.12}$	$1.87^{+0.08}_{-0.08}$
p_1	High energy spectral slope	$3.77^{+0.11}_{-0.13}$	$3.58^{+0.13}_{-0.11}$	$3.54^{+0.10}_{-0.09}$
γ_{min}	Low-energy-cut-off Lorentz factor	$13.38^{+0.89}_{-1.00}$	$14.74^{+0.89}_{-0.82}$	$32.31^{+1.93}_{-3.78}$
$\gamma_{max} \times 10^5$	High-energy-cut-off Lorentz factor	$9.07^{+0.25}_{-0.68}$	$8.26^{+0.19}_{-0.13}$	$9.56^{+0.37}_{-1.20}$
R (cm) $\times 10^{16}$	Emitting region size	$31.62^{+0.40}_{-1.13}$	$10.39^{+1.81}_{-1.64}$	$3.42^{+0.00}_{-0.00}$
δ	Doppler factor	$12.20^{+0.00}_{-0.00}$	$12.20^{+0.00}_{-0.00}$	$26.07^{+2.41}_{-1.91}$
B (G)	Magnetic field	$0.26^{+0.01}_{-0.01}$	$0.36^{+0.03}_{-0.03}$	$0.37^{+0.01}_{-0.01}$
N (cm^{-3})	Emitter density	$3.08^{+0.39}_{-0.25}$	$5.10^{+0.32}_{-0.29}$	$11.59^{+3.35}_{-2.64}$
χ^2/dof	Chi-square/degrees of freedom	29.03/19	29.69/18	4.21/2

S5 1803+784 observational features are consistent with single-zone SSC+EC emission during the flare. The inverse Compton scattering is dominated by the soft photons re-emitted from the DT. All of the Lorentz factors associated with the electron energy distribution, namely γ_{min}, γ_b and the γ_{max}, increase during the flare, while the size of the emitting region becomes more compact (Table 7.1); this portrays a scenario where there is a collapse of the emitting region size, which could be triggered by sudden rearrangement of the magnetic field lines within the emitting region.

The X-ray emission in the quiescent state comes from the inverse Compton scattering, while during the flare, the X-ray forms part of the upper tail of the synchrotron emission due to the

acceleration of the emitting particles in the photon radiation field (Abdo *et al.*, 2010); this is consistent with the highly curved gamma-ray spectrum during the flare (Tables 5.1 and 5.2). The most viable explanation for the multiwavelength flare that peaked on April 12, 2020, is a sudden dissipation and conversion of magnetic energy in the reconnecting magnetic field lines into particle kinetic energy. It causes sudden particle acceleration whereby the increase in the highest electron energies causes synchrotron emission to extend into the X-ray range, dominating the X-ray emission from inverse Compton emission seen during the quiescent phase. The brightness of the gamma-ray flare (Compton dominance) suggests that the emitting region is closer to an external photon radiation field that provides seed photons for inverse Compton scattering to high-energies (e.g., Ghisellini *et al.*, 2010; Finke, 2013).

7.1.2 BL Lacertae

As stated in Section 6.3, the single-zone emitting region leptonic jet model fails to reproduce the quiescent SED of BL Lacertae and cannot fit the SED of the flare without increasing the size of the emitting beyond the size constraint provided by the short variability time scale. Also, the flux doubling time for the different wavebands in Table 3.12 and the gamma-ray Flare A1 duration and t_{var} from Chapter 6 suggests that the X-ray and γ-ray emissions are from the same emitting region of the jet, while the radio flux with a flux doubling time of 9.43 days is from another region of the jet. Therefore, we propose a two-zone model (see Figure 7.1) for the jet emission, in which the emission comes from two regions of the jet: Zone A, responsible for most of the observed X-ray and gamma-ray emission, and Zone B, which is responsible for most of the radio emission.

In this model, the observed gamma-ray flux variability and the variability timescale (Chapters 3 and 4) in BL Lacertae could be coming from Zone A (Figure 7.1) where R_γ is consistent with the size of the emitting region estimated with $R < c\delta t_{var}/(1+z)$, where $t_{var} = t_r \, ln\, 2$ and $R_\gamma = 2.70 \times 10^{15}$ cm. $R < 1.38 \times 10^{17}$ cm, the value return by the single-zone SED modelling in Chapter 6, is used to constrain the size of the whole emitting region (see Figure 7.1).

Figure 7.2 shows that this model of the gamma-ray emission fits the SED. The BLR re-emitted accretion disk photons provide the seed photons for the external inverse-Compton scattering in Zone A of the emitting region, while the radio flux with a flux doubling time of 9.43 days is from another region of the jet consistent with Zone B.

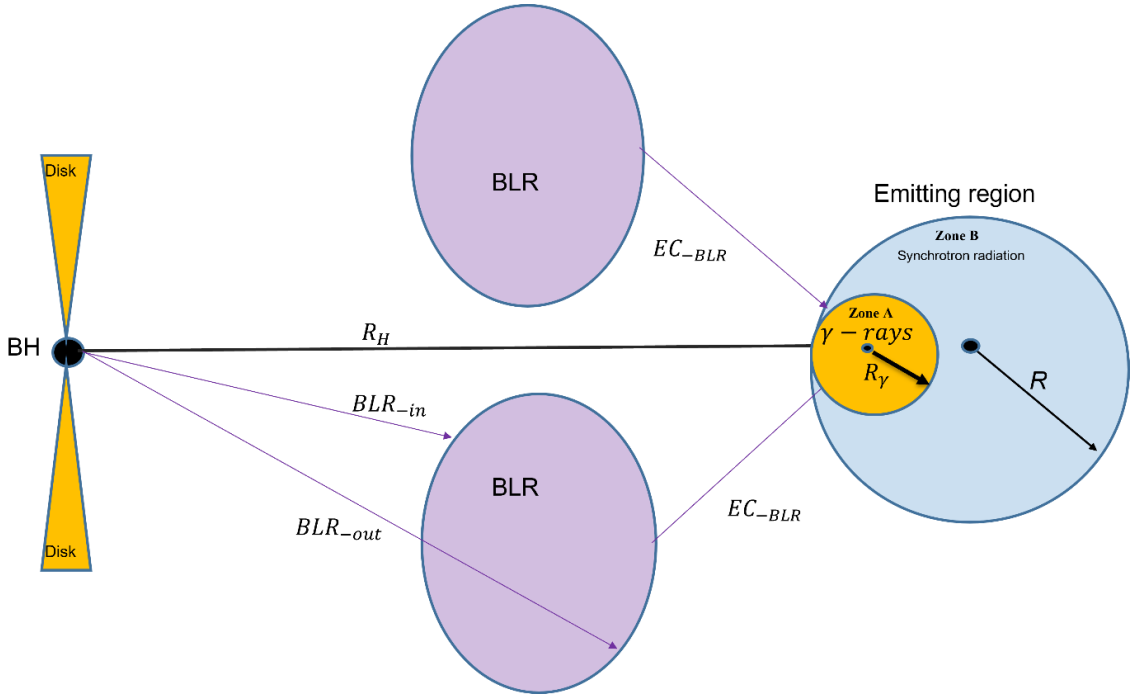


Figure 7.1: BL Lacertae jet components and the emitting region location and structure during Flare A1 (not to scale).

7.2 Two-zone multiwavelength SED model of BL Lacertae Flare A1

BL Lacertae single-zone SED results in Chapter 6 further agree with the assumption that multiple emitting regions in BL Lacertae are possible. The very short variability observed in BL Lacertae could also be because of multiple interacting magnetized blobs (Figure 7.1), resulting in magnetic reconnection and particle acceleration within the reconnecting field lines (e.g., Sironi *et al.*, 2015). Also, the PSF suggests that the γ-ray emission is due to up-scattered re-emitted disk photons from the BLR; this implies that the γ-ray emission suffers minimal absorption in the γ-γ interactions, which would have happened if the emitting region were within the BLR.

The electron distributions in each zone are modeled as broken power-laws. Figure 7.2 shows the SED of BL Lacertae fit to a two-zone synchrotron+SSC-only leptonic model. The SSC-only model cannot fit the high-energy component of the SED without the addition of external photons undergoing inverse Compton scattering. Therefore, Zone A and Zone B are both modeled as SSC+EC components. Zone A is dominated by the high energy emission and is modeled using the jet parameters in Table 6.5, while Zone B is dominated by synchrotron radiation with a weak inverse Compton component (Figure 7.1).

The two-zone model produces a good fit to the quiescent SED, albeit with a lower disk luminosity (8.79×10^{42} erg/s). The two-zone emitting region best-fit parameters and the SED

are in Table 7.2 and Figure 7.3.

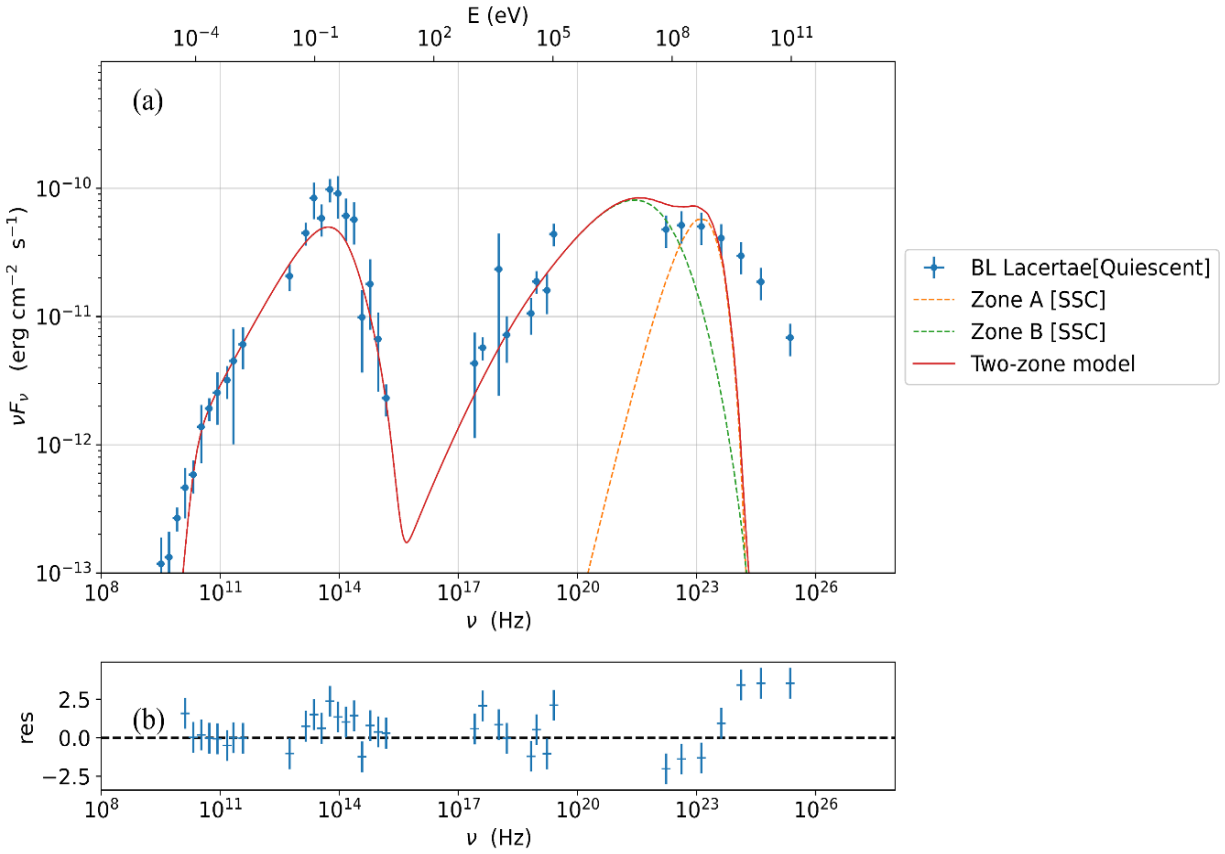


Figure 7.2: BL Lacertae two-zone SSC leptonic jet model fit to the quiescent state.

The quiescent SED model shows that the X-ray emission comes from zones A and B.
The X-ray emission from Zone B dominates the high-energy X-ray emission, while the gamma-ray emission comes primarily from Zone A. The higher high-energy Lorentz factor in Zone B (Table 7.2) and the harder low-energy spectral slope in the zone compared with the flare time spectral slope (Tables 7.2 and 7.3) is consistent with energy injection from Zone A into Zone B. Apart from the possible disk-jet interaction, the dense leptonic particle distribution in the emitting region, the magnetic field and the Doppler factor are the results of particle acceleration in the jet of BL Lacertae.

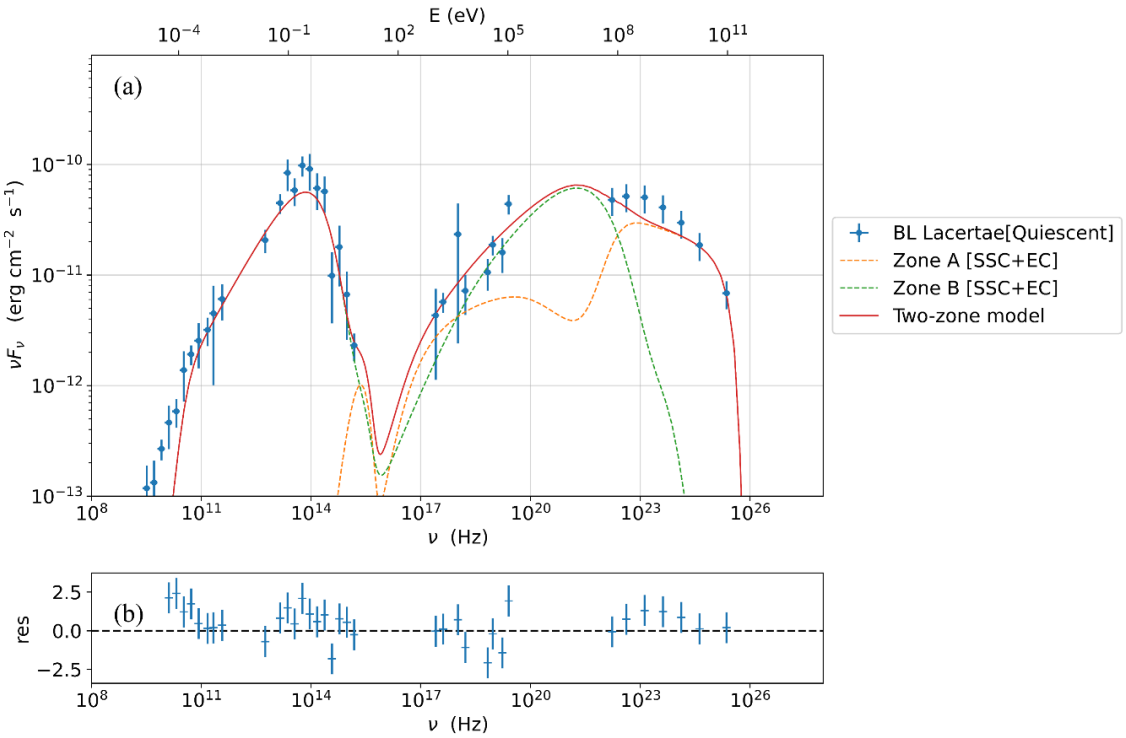


Figure 7.3: BL Lacertae two-zone leptonic jet SED model of the quiescent state.

Table 7.2: Two-zone SED model best-fit parameters of the quiescent state (Q).

Zone A model fit parameters of the quiescent state.

Symbol (unit)	Description	Q (Zone A)
$\gamma_b \times 10^3$	Turn-over-energy Lorentz factor	1.67
p	Low energy spectral slope	2.15
p_1	High energy spectral slope	3.12
γ_{min}	Low-energy-cut-off Lorentz factor	850
$\gamma_{max} \times 10^5$	High-energy-cut-off Lorentz factor	0.35
R_γ (cm) $\times 10^{16}$	Emitting region size	0.27
δ	Doppler factor	20.00
B (G)	Magnetic field	0.00015
N(cm^{-3})	Emitter density	192000

Zone B model fit parameters of the quiescent state.

Symbol (unit)	Description	Q (Zone B)
$\gamma_b \times 10^3$	Turn-over-energy Lorentz factor	6.05
p	Low energy spectral slope	1.81
p_1	High energy spectral slope	5.80
γ_{min}	Low-energy-cut-off Lorentz factor	98

$\gamma_{max} \times 10^5$	High-energy-cut-off Lorentz factor	1.55
R (cm) $\times 10^{16}$	Emitting region size	4.80
δ	Doppler factor	14.00
B (G)	Magnetic field	0.053
N (cm^{-3})	Emitter density	42.90

χ^2/dof= 2.31.

The two-zone emitting region model parameters and the SED during the flare are in Table 7.3 and Figure 7.3, respectively.

The leptonic particles population in Zone A during the flare are accelerated with a harder low energy spectral slope, lower magnetic field, and high Doppler factor. Combined with the multiwavelength short timescale flux variability, these are consistent with magnetic dissipation through reconnecting magnetic field lines as the mechanism enhancing particle acceleration in the zone. Due to magnetic dissipation, which leads to highly dense and accelerated particles, the bulk of the synchrotron photons produced in Zone A are likely up-scattered in an SSC process to produce the X-ray emission, coupled with external inverse Compton scattering of the UV/optical photons re-emitted from the BLR to produce the gamma-ray emission during the flare.

Due to the optical photon flux doubling time (Table 3.11) during the flare, it is difficult to consider the optical photons in Zone B to be the intrinsic synchrotron radiation. Instead, they could be a result of cooling due to the K-N effect when particles in Zone B interact with the high energy photon field at the boundary of Zone A. This scenario could explain the less than a day flux doubling time in the U, V, and B Swift/UVOT observation and the highly curved spectrum observed in gamma-ray emission (Table 6.2). The K-N effect increases the energy of the electron population in Zone B, causing the radio flux to double in 9.43 days.

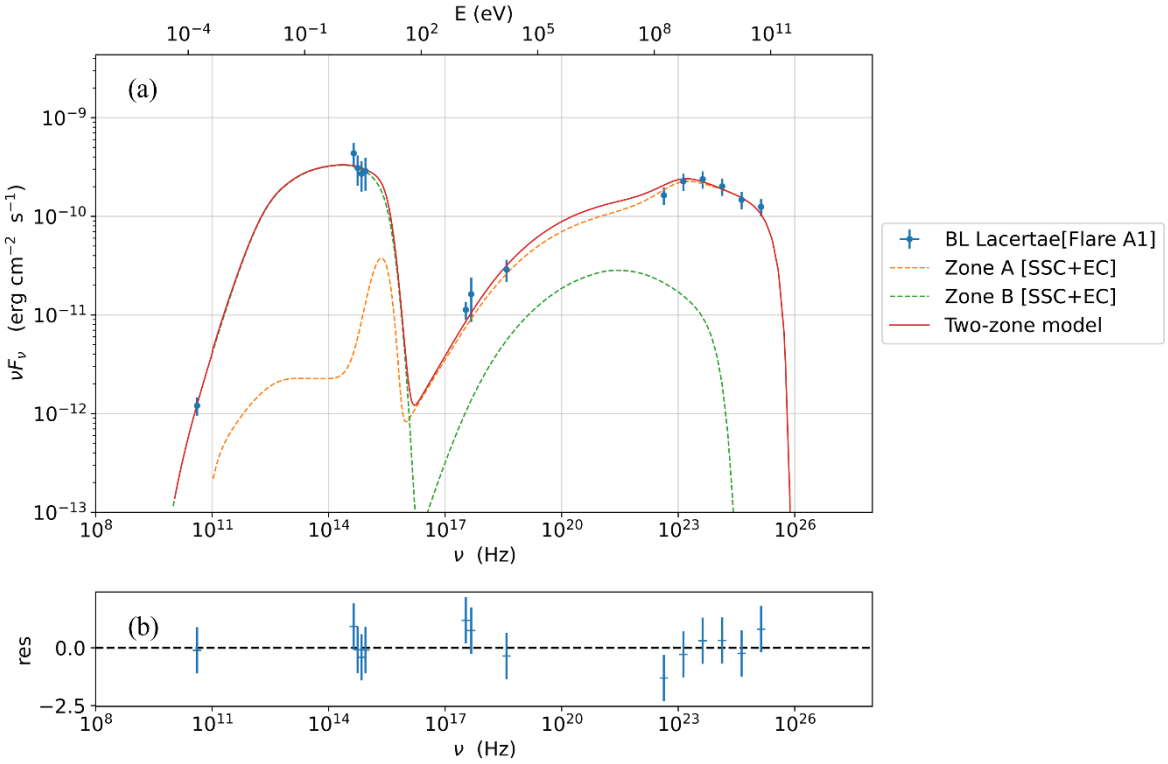


Figure 7.4: BL Lacertae two-zone leptonic jet SED model of Flare A1.

Zone A is a high-energy emitting blob with magnetic energy density $U_B = 4.94 \times 10^{-7}$ erg cm^{-3} and particle energy density $U_e = 44.04$ erg cm^{-3} in the emitting region rest frame, while the synchrotron emission dominates Zone B with a higher magnetic field (Table 7.3) and with $U_B = 9.41 \times 10^{-4}$ erg cm^{-3} and $U_e = 2.86 \times 10^{-3}$ erg cm^{-3}. This result is consistent with magnetic dissipation in Zone A and that the BL Lacertae flare of October 6, 2020, is particle-dominated in Zone A and tends to equipartition in Zone B.

The build-up of energy injection from Zone A on the leptonic particle population in Zone B through the K-N effect is one of the plausible mechanisms to drive the particle acceleration that gives rise to the radio flare observed later around MJD 59249 in Zone B; this scenario could explain why there is no clear correlation between the gamma-ray flare and the radio flare in BL Lacertae flares (refer to Figures 3.2 and 4.2).

Table 7.3: Two-zone SED model best-fit parameters of Flare A1.

Zone A model fit parameters of Flare A1.

Symbol (unit)	Description	Flare A1 (Zone A)
$\gamma_b \times 10^3$	Turn-over-energy Lorentz factor	1.74
p	Low energy spectral slope	1.70
p_1	High energy spectral slope	3.01

γ_{min}	Low-energy-cut-off Lorentz factor	4.50
$\gamma_{max} \times 10^4$	High-energy-cut-off Lorentz factor	3.74
R_γ (cm) $\times 10^{16}$	Emitting region size	0.27
δ	Doppler factor	29.34
B (G)	Magnetic field	0.011
N (cm^{-3})	Emitter density	233000

Zone B model fit parameters of Flare A1.

Symbol (unit)	Description	Flare A1 (Zone B)
$\gamma_b \times 10^3$	Turn-over-energy Lorentz factor	1.00
p	Low energy spectral slope	2.12
p_1	High energy spectral slope	2.80
γ_{min}	Low-energy-cut-off Lorentz factor	362
$\gamma_{max} \times 10^4$	High-energy-cut-off Lorentz factor	1.00
R (cm) $\times 10^{16}$	Emitting region size	9.60
δ	Doppler factor	13.22
B (G)	Magnetic field	0.36
N (cm^{-3})	Emitter density	1.45

$\chi^2/\mathrm{dof} = 2.92$.

Previously, for example, in Cerruti et al. (2017), a two-zone model was used to explain the gamma-ray emission of PKS 1424+240, where the external photon field was modelled as reprocessed infrared radiation from the DT after the standard single-zone SSC model could not satisfactorily reproduce the SED without a very high Doppler factor, i.e. > 250, even though it is a high-frequency peak blazar. With a two-zone model, the Doppler factor returns a reasonable value of 30.

Also, a two-zone multiwavelength time-dependent SED model was developed by Prince et al. (2019) to explain the emitting region structure and emission mechanism of the observed flare of PKS 1510-089, whereby one emitting zone is located near the outer edge of the blazar's BLR and another further away in the DT. The flux doubling-time of the different wavebands implies that the gamma-ray and optical emission regions are co-spatial. At the same time, the X-ray with less variability was assumed to originate from the DT.

In Chapters 5 and 6, I considered the emitting region and the emission mechanism of the two blazars in the framework of the single zone leptonic jet model. While S5 1803+784 is consistent with the single zone emitting region model, BL Lacertae is consistent only with multiple emitting zones, leading to the model discussed in this chapter. The gamma-ray emission could

come from a region such as Zone A in Figure 7.1. The SED, as shown in Figure 7.2, and the highly curved gamma-ray spectrum may not be due to BLR absorption but rather due to K-N cooling of the high energy photon field interacting with the leptonic particle population in Zone B, producing the optical photons with a less than a day flux doubling time average of 0.89 day.

CHAPTER 8

8.0 Summary of results and conclusion

The multi-wavelength SEDs of both the flaring and quiescent states of S5 1803+784 and BL Lacertae were fit to leptonic jet models using the JetSeT code (Tramacere, 2020). S5 1803+784 was well fit by a single-zone SSC+EC model; BL Lacertae requires a two-zone SSC+EC model. The flaring periods were determined using *Fermi*-LAT analysis of the daily binned light curves of the blazars obtained through the Astronomer's Telegram (ATel) alerts (Buson, 2020; Mereu, 2020; Ojha and Valverd, 2020; Venters, Angioni and Ojha, 2020; Buson and de Menezes, 2021; Mura, 2021). The synchrotron radiation of the quiescent data of the blazars was obtained from NED archival data (Raiteri *et al.*, 2009; Paliya *et al.*, 2017) and the gamma-ray spectra from the 4FGL-DR2 catalog (Abdollahi *et al.*, 2020). Multiwavelength data simultaneous with the gamma-ray flare were used for the flare-time SED modelling to study the features of particle acceleration in the two blazars.

8.1 Summary of results

All the gamma-ray flares are well detected with a TS $>$ 900, and the log parabola distribution function describes the gamma-ray spectra well. The two blazars experienced multiwavelength flares in the period studied.

8.1.1 S5 1803+784

The gamma-ray emission in S5 1803+784 is dominated by inverse Compton scattering of re-emitted disk photons from the dusty torus within a single-zone emitting region. S5 1803+784 has very low equivalent width (EW) BLR emission lines in its optical spectrum, which is why it is categorized as a BL Lac. The broadband spectral energy distribution shows that S5 1803+784 transitioning from LSP in the quiescent state to ISP during the flare is consistent with the presence of highly accelerated emitting particles whereby the X-ray emission, which is at the lower end of the inverse Compton scattering in the quiescent state, becomes part of the upper tail of the synchrotron emission during the flare. The flare is Doppler-boosted (about 26.07), with the Doppler factor higher than the 12.2 observed in previous VLBI observations of this blazar (Hovatta *et al.*, 2009).

The distance of the emitting region (R_H) from the black hole is 5.00×10^{17}cm (<0.3pc) with an average disk luminosity (L_{Disk}) of 2.20×10^{44}erg/s during the flares, and the size of the emitting region is 3.42×10^{16}cm. Using the standard model of bright blazars (Ghisellini and

Tavecchio, 2009) for the phenomenological spectral fit, the best-fit parameters for this blazar, both during its flaring states and the quiescent state, show that a single-zone leptonic jet model could best describe Flare A. The temporal analysis shows that four flares labeled as Flares A, C, D, and E have a symmetric profile, while Flares B and F are asymmetric. The asymmetric flares could imply the injection of accelerated particles in the emitting region. The asymmetric feature could also be due to the fast injection of accelerated particles following a sudden magnetic dissipation. The symmetric flares could result from the superposition of several episodes of flares of short duration, as proposed in the previous studies (Abdo *et al.*, 2010). These episodes of short duration are consistent with downstream magnetic dissipation in the emitting region (Sironi, Petropoulou and Giannios, 2015). The low energy spectral slope with a hard power-law spectrum and the emitting region that is particle dominated are features consistent with magnetic dissipation. The daily binned light curve does not capture the gamma-ray flux variability during the flares; with the 7-day binned light curve, the flux variability is significant at 0.70 ± 0.10. The photon seed factor during Flare A also agrees that the dusty torus is the primary source of the external photons responsible for the inverse Compton emission. The single-zone jet leptonic model could fit the observed SED and explain the spectral features of this blazar.

8.1.2 BL Lacertae

BL Lacertae, the prototype BL Lac object, has been active since August 2020 (Cheung, 2020; Mereu, 2020). SSC+EC photons dominate the gamma-ray emission of BL Lacertae during the flares, with re-emitted disk (UV-Optical) photons from the BLR undergoing inverse Compton scattering. A previous SSC+EC SED model (Böttcher *et al.*, 2013) required a 0.13 fraction of the disk photons re-emitted from the BLR because the SSC-only leptonic emission is insufficient to reproduce the high energy hump of the blazar. Also, Ghisellini and Tavecchio. (2009) fit the high energy hump with a combination of SSC and inverse Compton scattering of photons from the dusty torus (DT), but since there is no observational evidence of a DT in BL Lacertae, this may not be a physical representation of the emission processes in the blazar (e.g., Acciari *et al.*, 2019).

In this work, the phenomenological model for the BL Lacertae SED assumed a 13% fraction of the disk luminosity re-emitted from the BLR. The emitting region outside the BLR could reproduce the observed fluxes during the flares. Considering the emitting region outside the BLR is consistent with the Costamante et al. (2018) model.

The emitting region distance from the central black hole is found to be 1.37×10^{17}cm. The size of the emitting region is constrained by both the previous VLBI Doppler factor and the variability time scale to be no larger than 2.70×10^{15} cm. A single-zone model, whether SSC only or SSC+EC, cannot fit the SED without increasing the size of the emitting region beyond this constraint; this points to the possibility of multiple emitting blobs, where the short-timescale gamma-ray flux likely emerges from the smaller of such blobs. A two-zone model is proposed to explain the observed spectral characteristics and features. The high energy emission-dominated Zone A has an emitting region size of 2.70×10^{15} cm, and the synchrotron radiation-dominated Zone B has an emitting region size of 9.60×10^{16} cm. Zone A is particle-dominated, with emitting region rest frame particle and magnetic energy densities during the flare;

$U_e = 44.04$ erg cm^{-3} and $U_B = 4.94 \times 10^{-7}$erg cm^{-3} respectively. The harder low-energy spectral slope of 1.7 in Zone A is consistent with magnetic dissipation (e.g., Guo *et al.*, 2014; Böttcher, 2019).

The symmetric flare labeled as Flare A4 produced the highest daily flux ever observed from BL Lacerate at $(64.86 \pm 3.16) \times 10^{-7}$cm^{-2}s^{-1} in the 0.1-300GeV energy range with an observer frame flare duration of less than six days, the shortest flare is Flare A5, with a duration of 2.1 days. Flare A1 is an asymmetric flare with flare time flux variability of 84%, the highest up to that time from BL Lacertae. A very hard power-law low-energy spectral slope and particle-dominated emitting region are consistent with magnetic dissipation through magnetic reconnection in the emitting region during the flare. The SSC+EC from the BLR model reproduces the observed broadband spectral energy distribution. The Doppler factor in the single-zone SEDs model is 26.58±1.50, consistent with the previously estimated average of 20.6 ± 8.4 (Cha *et al.*, 2014), while the two-zone SED model shows that the flare in the high-energy emitting region (Zone A) is Doppler boosted to a value of 29.34 with a harder low energy spectral slope consistent with magnetic dissipation in the emitting region. The two-zone SED model can reproduce the spectral features and characteristics of both the quiescent and flaring states of BL Lacertae.

8.2 Conclusion and outlook

S5 1803+784 and BL Lacertae each started flaring in 2020 with an average daily gamma-ray flux higher than any previous measurement. The two blazars share similarities: they are both BL Lac objects and LSP in their quiescent states. They are an important testbed to study the

particle acceleration mechanism and the high energy emission process(es). The multiwavelength SEDs and the temporal characteristics of the flares were interpreted in the framework of the leptonic jet model using first the single-zone synchrotron+SSC-only and SSC+EC jet models; while a single zone SSC+EC model was able to explain the emission from S5 1803+784, a two-zone leptonic model was required to explain the observational data in the case of BL Lacertae. The wide variations in the TS_{curve} of BL Lacertae (Table 6.2) could provide an indirect probe as a signature of multiple emitting blobs compared with that of S5 1803+784 with less variation in the TS_{curve} (Table 5.2) consistent with the single-zone emitting region.

In my future work, I will study other blazars with no clear or very weak emission lines and highly curved gamma-ray spectra to search for cases where a two-zone scenario similar to the one used here to model BL Lacertae would also be required. Furthermore, X-ray polarimetry of these blazars may help to ascertain the location and nature of the emitting region and the magnetic field structure and untangle the source(s) of the seed photons of the inverse Compton scattering. High energy polarization signatures can potentially provide a better view of the emitting region's magnetic field structure and the predominant high energy emission mechanism (e.g., Zhang and Böttcher, 2013; Cerruti, 2020). For example, the upcoming Imaging X-ray Polarimetry Explorer (IXPE) data (Weisskopf *et al.*, 2022) may allow us to constrain the magnetic field strength of the high energy emitting region and to know if the dominant inverse Compton seed photons up-scattered in these blazars are intrinsic or external to the jet. The polarization angle of X-rays originating from an ordered magnetic region in the SSC process is expected to be higher than that of X-rays originating from inverse Compton scattering of seed photons external to the jet or from inverse Compton scattering from within the jet in regions of magnetic turbulence. A highly polarized X-ray emission could potentially point exclusively to the SSC process in the jet, and a less polarized X-ray emission could be probed as an external inverse Compton process.

X-ray polarimetry of S5 1803+784 and BL Lacertae during a flare would provide additional constraints on the jet emission mechanism. With the incoming IXPE data, I will study these two blazars and be able to distinguish the X-ray source(s) that originate as the SSC component of the synchrotron radiation in the region of ordered high magnetic field strength in the jet from the external inverse Compton scattering in the emitting region where magnetic dissipation has taken place and to probe the nature of the emitting blobs in such blazars.

REFERENCES

Aartsen, M.G., Abbasi, R., Abdou, Y., *et al.* (2013) 'First observation of PeV-Energy neutrinos with IceCube,' *Physical Review Letters*, 111, p. 021103. doi:10.1103/PhysRevLett.111.021103.

Aartsen, M.G., Ackermann, M., Adams, J., *et al.* (2018) 'Astrophysical neutrinos and cosmic rays observed by IceCube,' *Advances in Space Research*, 62, pp. 2902–2930. doi:10.1016/j.asr.2017.05.030.

Abdalla, H., Aharonian, F., Benkhali, F. A., *et al.* (2019) 'The 2014 TeV Gamma-Ray Flare of Mrk 501 Seen with H.E.S.S.: Temporal and Spectral Constraints on Lorentz Invariance Violation', *The Astrophysical Journal*, 870(2), p. 93. doi:10.3847/1538-4357/aaf1c4.

Abdo, A., Ackermann, M., Ajello, M., *et al.* (2011) 'Insights into the High-Energy Gamma-ray emission of Markarian 501 from extensive multifrequency observations in the *Fermi* era', *Astrophysical Journal*, 727. doi:10.1088/0004-637X/727/2/129.

Abdo, A.A., Ackermann, M., Ajello, M., *et al.* (2010) 'γ Light Curves and Variability of Bright Fermi-detected Blazars', *The Astrophysical Journal*, 722, pp. 520–542. doi:10.1088/0004-637X/722/1/520.

Abdo, A.A., Ackermann, M., Agudo, I., *et al.* (2010) 'The Spectral Energy Distribution of Fermi Bright Blazars', *The Astrophysical Journal*, 716, pp. 30–70. doi:10.1088/0004-637X/716/1/30.

Abdollahi, S., Acero, F., Ackermann, M., *et al.* (2020) 'Fermi Large Area Telescope Fourth Source Catalog,' *The Astrophysical Journal Supplement Series*, 247, p. 33. doi:10.3847/1538-4365/ab6bcb.

Abeysekara, A.U., Benbow, W., Bird, R., *et al.* (2018) 'Multiwavelength Observations of the Blazar BL Lacertae: A New Fast TeV Gamma-ray Flare,' *The Astrophysical Journal*, 856, pp. 95. doi: 10.3847/1538-4357/aab35c.

Acciari, V.A., Ansoldi, S., Antonelli, L.A., *et al.* (2019) 'A fast, very-high-energy Gamma-ray flare from BL Lacertae during a period of multi-wavelength activity in June 2015', *Astronomy & Astrophysics*, 623, p. A175. doi:10.1051/0004-6361/201834010.

Ackermann, M. *et al.* (2011) 'The Second Catalog of Active Galactic Nuclei Detected by the Fermi Large Area Telescope', *The Astrophysical Journal*, 743, p. 171. doi:10.1088/0004-637X/743/2/171.

Ackermann, M., Anantua, R., Asano, K., *et al.* (2016) 'Minute-timescale 100 MeV gamma-ray variability during the giant outburst of quasar 3C 279 observed by *FERMI* -LAT in 2015 June', *The Astrophysical Journal*, 824(2), p. L20. doi:10.3847/2041-8205/824/2/L20.

Aharonian, F., Akhperjanian, A.G., Bazer-Bachi, A.R., *et al.* (2006) 'A low level of extragalactic background light as revealed by Gamma-rays from blazars,' *Nature*, 440(7087), pp. 1018–1021. doi:10.1038/nature04680.

Aharonian, F., Akhperjanian, A.G., Bazer-Bachi, A.R., (2007) 'Detection of VHE Gamma-ray emission from the distant blazar 1ES 1101-232 with HESS and broadband characterisation', *Astronomy and Astrophysics*, 470(2), pp. 475–489. doi:10.1051/0004-6361:20077057.

Arnaud, K.A. (1996) 'XSPEC: The First Ten Years', 101, p. 17.

Arsioli, B. and Chang, Y.-L. (2018) 'The Gamma-ray emitting region in low synchrotron peak blazars - Testing self-synchrotron Compton and external Compton scenarios', *Astronomy & Astrophysics*, 616, p. A63. doi:10.1051/0004-6361/201833005.

Atwood, W., Albert, A., Baldini, L., *et al.* (2013) *Pass 8: Toward the full realization of the Fermi-LAT scientific potential*, *arXiv e-prints*. Available at: https://ui.adsabs.harvard.edu/abs/2013arXiv1303.3514A.

Atwood, W.B., Abdo, A.A., Ackermann, M., *et al.* (2009) 'The Large Area Telescope on the Fermi Gamma-ray Space Telescope Mission,' *The Astrophysical Journal*, 697, pp. 1071–1102. doi:10.1088/0004-637X/697/2/1071.

Bañados, E., Venemans, B. P., Mazzuchelli, C., *et al.* (2018) 'An 800-million-solar-mass black hole in a significantly neutral Universe at a redshift of 7.5', *Nature*, 553, pp. 473–476. doi:10.1038/nature25180.

Begelman, M.C., Fabian, A.C. and Rees, M.J. (2008) 'Implications of very rapid TeV variability in blazars', *Monthly Notices of the Royal Astronomical Society*, 384, pp. L19–L23. doi:10.1111/j.1745-3933.2007.00413.x.

Bhattacharyya, S., Sahayanathan, S. and Kaul, C.L. (2002) 'Effect of Particle Acceleration Process on the Flare Characteristics of Blazars', *Journal of Astrophysics and Astronomy*, 23, p. 95. doi:10.1007/BF02702471.

Bisnovatyi-kogan, G. (2019) 'Accretion into black hole, and formation of magnetically arrested accretion disks'. doi:10.3390/UNIVERSE5060146.

Blandford, R., Meier, D. and Readhead, A. (2019) 'Relativistic jets from active galactic nuclei,' *Annual Review of Astronomy and Astrophysics*, 57(1), pp. 467–509. doi:10.1146/annurev-astro-081817-051948.

Blandford, R.D. and Znajek, R.L. (1977) 'Electromagnetic extraction of energy from Kerr black holes.', *Monthly Notices of the Royal Astronomical Society*, 179, pp. 433–456. doi:10.1093/mnras/179.3.433.

Bloom, S.D. and Marscher, A.P. (1996) 'An Analysis of the Synchrotron Self-Compton Model for the Multi-Wave Band Spectra of Blazars', *The Astrophysical Journal*, 461, p. 657. doi:10.1086/177092.

Blumenthal, G.R. and Gould, R.J. (1970) 'Bremsstrahlung, Synchrotron Radiation, and Compton Scattering of High-Energy Electrons Traversing Dilute Gases', *Reviews of Modern Physics*, 42, pp. 237–271. Available at: https://doi.org/10.1103/RevModPhys.42.237.

Böttcher, M., Reimer, A., Sweeney, K., *et al.* (2013) 'Leptonic and Hadronic modeling of Fermi-detected blazars,' *The Astrophysical Journal*, 768, p. 54. doi:10.1088/0004-637X/768/1/54.

Böttcher, M. (2019) 'Progress in Multi-wavelength and Multi-Messenger Observations of Blazars and Theoretical Challenges', *Galaxies*, 7, p. 20. doi:10.3390/galaxies7010020.

Breeveld, A.A., Curran, P.A, Hoversten, E. A., *et al.* (2010) 'Further calibration of the Swift ultraviolet/optical telescope', *Monthly Notices of the Royal Astronomical Society*, 406, pp. 1687–1700. doi:10.1111/j.1365-2966.2010.16832.x.

Buson, S. (2020) 'Fermi-LAT detection of a bright Gamma-ray flare from the blazar PKS B1406-076', *The Astronomer's Telegram*, 13882, p. 1.

Buson, S. and de Menezes, R. (2021) 'Fermi-LAT detection of continued enhanced Gamma-ray activity from BL Lac', *The Astronomer's Telegram*, 14777, p. 1.

Cash, W. (1979) 'Parameter estimation in astronomy through application of the likelihood ratio.', *The Astrophysical Journal*, 228, pp. 939–947. doi:10.1086/156922.

Cerruti, M. (2020) 'Leptonic and Hadronic Radiative Processes in Supermassive-Black-Hole Jets', *Galaxies*, 8, p. 72. doi:10.3390/galaxies8040072.

Cerruti, M., Benbow, W., Chen, X., *et al.* (2017) 'Luminous and high-frequency peaked blazars: the origin of the Gamma-ray emission from PKS 1424+240', *Astronomy & Astrophysics, Volume 606, id.A68, pp.*, 606, p. A68. Available at: https://doi.org/10.1051/0004-6361/201730799.

Cha, Y., Zhang, H., Zhang, Y., *et al.* (2014) 'The evolutionary sequence of Fermi blazars', *Astrophysics and Space Science*, 349(2), pp. 895–908. doi:10.1007/s10509-013-1667-z.

Cheung, C.C. (2020) 'Fermi-LAT detection of a Gamma-ray flare of the blazar BL Lacertae coincident with an optical flare', *The Astronomer's Telegram*, 13933, p. 1.

Christie, I.M., Petropoulou, M., Sironi, L., *et al.* (2019) 'Radiative signatures of plasmoid-dominated reconnection in blazar jets', *Monthly Notices of the Royal Astronomical Society*, 482, pp. 65–82. Available at: https://doi.org/10.1093/mnras/sty2636.

Cortina, J. and Project, C. l. (2019) 'Status of the Large Size Telescopes of the Cherenkov Telescope Array', 36, p. 653.

Costamante, L., Cutini, S., Tosti, G., *et al.* (2018) 'On the origin of Gamma-rays in Fermi blazars: beyond the broad-line region,' *Monthly Notices of the Royal Astronomical Society*, 477(4), pp. 4749–4767. doi:10.1093/mnras/sty887.

D'Ammando, F. (2020) 'Swift detection of record X-ray flare of BL Lacertae', *The Astronomer's Telegram*, 14069, p. 1.

D'Ammando, F. (2022) 'NICER, NuSTAR, and Swift follow-up observations of the Gamma-ray flaring blazar BL Lacertae in 2020 August-October', *Monthly Notices of the Royal Astronomical Society*, 509, pp. 52–67. doi:10.1093/mnras/stab2616.

Dermer, C.D., Finke, J.D., Krug, H., *et al.* (2009) 'Gamma-ray Studies of Blazars: Synchro-Compton Analysis of Flat Spectrum Radio Quasars', *The Astrophysical Journal*, 692, pp. 32–46. doi:10.1088/0004-637X/692/1/32.

Dermer, C.D. and Schlickeiser, R. (2002) 'Transformation Properties of External Radiation Fields, Energy-Loss Rates and Scattered Spectra, and a Model for Blazar Variability', *The Astrophysical Journal*, 575, pp. 667–686. doi:10.1086/341431.

Dermer, C.D., Schlickeiser, R. and Mastichiadis, A. (1992) 'High-energy gamma radiation from extragalactic radio sources.', *Astronomy and Astrophysics, Vol. 256, p. L27-L30 (1992)*, 256, p. L27.

Dondi, L. and Ghisellini, G. (1995) 'Gamma-ray-loud blazars and beaming', *Monthly Notices of the Royal Astronomical Society*, 273, pp. 583–595. doi:10.1093/mnras/273.3.583.

Edelson, R.A. and Krolik, J.H. (1988) 'The discrete correlation function: a new method for analysing unevenly sampled variability data', 2, pp. 387–390.

Evans, P.A., Beardmore, A.P., Osborne, J. P., *et al.* (2009) 'The unusual 2006 dwarf nova outburst of GK Persei', *Monthly Notices of the Royal Astronomical Society*, 399, pp. 1167–1174. doi:10.1111/j.1365-2966.2009.15376.x.

Falanga, M., Bykov, A.M., Li, Z., *et al.* (2021) 'Phase-resolved hard X-ray emission of the high-mass binary LS 5039: a spectral hardening above 50 keV detected with INTEGRAL', *Astronomy and Astrophysics*, 654, p. A127. doi:10.1051/0004-6361/202141102.

Finke, J.D. (2013) 'Compton Dominance and the Blazar Sequence', *The Astrophysical Journal*, 763, p. 134. doi:10.1088/0004-637X/763/2/134.

Finke, J.D. (2016) 'External Compton Scattering in Blazar Jets and the Location of the Gamma-ray Emitting Region', *The Astrophysical Journal*, 830, p. 94. doi:10.3847/0004-637X/830/2/94.

Foreman-Mackey, D., Conley, A., Meierjurgen, F.W., *et al.* (2013) 'emcee: The MCMC Hammer', *Astrophysics Source Code Library*, p. ascl:1303.002.

Gaidos, J.A., Akerlof, C.W., Biller, S., *et al.* (1996) 'Extremely rapid bursts of TeV photons from the active galaxy Markarian 421', *Nature*, 383(6598), pp. 319–320. doi:10.1038/383319a0.

Gattano, C., Lambert, S.B. and Le Bail, K. (2018) 'Extragalactic radio source stability and VLBI celestial reference frame: insights from the Allan standard deviation', *Astronomy and Astrophysics*, 618, p. A80. doi:10.1051/0004-6361/201833430.

Gehrels, N., Chincarini, G., Giommi, P., *et al.* (2004) 'The Swift Gamma-ray Burst Mission', *The Astrophysical Journal*, 611, pp. 1005–1020. doi:10.1086/422091.

Ghisellini, G. (1996) 'X-Ray and Gamma-ray Emission in Blazars', *Symposium - International Astronomical Union*, 175, pp. 413–416. doi:10.1017/S0074180900081286.

Ghisellini, G. (2013) 'Radiative Processes in High Energy Astrophysics', *Lecture Notes in Physics, Berlin Springer Verlag*, 873. doi:10.1007/978-3-319-00612-3.

Ghisellini, G. and Tavecchio, F. (2009) ‘Canonical high-power blazars’, *Monthly Notices of the Royal Astronomical Society*, 397, pp. 985–1002. doi:10.1111/j.1365-2966.2009.15007.x.

Ghisellini, G., Tavecchio, F., Maraschi *et al.* (2014) ‘The power of relativistic jets is larger than the luminosity of their accretion disks’, *Nature*, 515, pp. 376–378. doi:10.1038/nature13856.

Giannios, D. (2013) ‘Reconnection-driven plasmoids in blazars: fast flares on a slow envelope’, *Monthly Notices of the Royal Astronomical Society*, 431(1), pp. 355–363. doi:10.1093/mnras/stt167.

Giommi, P., Padovani, P. and Polenta, G. (2013) ‘A simplified view of blazars: the Gamma-ray case’, *Monthly Notices of the Royal Astronomical Society*, 431, pp. 1914–1922. doi:10.1093/mnras/stt305.

Guo, F., Li, H., Daughton, W. and Liu, Y.-H. (2014) ‘Formation of Hard Power Laws in the Energetic Particle Spectra Resulting from Relativistic Magnetic Reconnection’, *Physical Review Letters*, 113(15), p. 155005. doi:10.1103/PhysRevLett.113.155005.

Hartman, R.C., Böttcher, M., Aldering, G., *et al.* (2001) ‘Multiepoch multiwavelength spectra and models for blazar 3C 279’, *The Astrophysical Journal*, 553, pp. 683–694. doi:10.1086/320970.

Harvey, A.L.W., Georganopoulos, M. and Meyer, E.T. (2020) ‘Powerful extragalactic jets dissipate their kinetic energy far from the central black hole’, *Nature Communications*, 11(1), p. 5475. doi:10.1038/s41467-020-19296-6.

Hayashida, M., Madejski, G.M., Nalewajko, K., *et al.* (2012) ‘The structure and emission model of the relativistic jet in the quasar 3c 279 inferred from radio to high-energy Gamma-ray observations in 2008-2010’, *The Astrophysical Journal*, 754(2), p. 114. doi:10.1088/0004-637X/754/2/114.

Hervet, O., Boisson, C. and Sol, H. (2015) ‘Linking radio and Gamma-ray emission in Ap Librae’, *Astronomy and Astrophysics*, 578, p. A69. doi:10.1051/0004-6361/201425330.

Homan, D.C., Kadler, M., Kellermann, K.I., *et al.* (2009) ‘MOJAVE: Monitoring of Jets in Active Galactic Nuclei with VLBA Experiments. VII. Blazar Jet Acceleration’, *The Astrophysical Journal*, 706, pp. 1253–1268. Available at: https://doi.org/10.1088/0004-637X/706/2/1253.

Hovatta, T., Valtaoja, E., Tornikoski, M., *et al.* (2009) ‘Doppler factors, Lorentz factors and viewing angles for quasars, BL Lacertae objects and radio galaxies,’ *Astronomy & Astrophysics*, 494(2), pp. 527–537. doi:10.1051/0004-6361:200811150.

Hovatta, T. and Lindfors, E. (2019) ‘Relativistic Jets of Blazars’, *New Astronomy Reviews*, 87, p. 101541. doi:10.1016/j.newar.2020.101541.

IceCube Collaboration *et al.* (2018) ‘Multimessenger observations of a flaring blazar coincident with high-energy neutrino IceCube-170922A’, *Science*, 361, p. eaat1378. doi:10.1126/science.aat1378.

Kapanadze, B., Vercellone, S. and Romano, P. (2020) 'Stochastic acceleration in the relativistic jets of BL Lacertae objects', *New Astronomy*, 79, p. 101393. doi:10.1016/j.newast.2020.101393.

Kataoka, J., Mattox, J.R., Quinn, J., *et al.* (1999) 'High-Energy Emission from the TEV Blazar Markarian 501 during Multiwavelength Observations in 1996', *The Astrophysical Journal*, 514, pp. 138–147. doi:10.1086/306918.

Khangulyan, D., Aharonian, F.A. and Kelner, S.R. (2014) 'Simple Analytical Approximations for Treatment of Inverse Compton Scattering of Relativistic Electrons in the Blackbody Radiation Field', *The Astrophysical Journal*, 783, p. 100. Available at: https://doi.org/10.1088/0004-637X/783/2/100.

Kishimoto, M., Hönig, S.F., Antonucci, R., *et al.* (2011) 'Mapping the radial structure of AGN tori', *Astronomy and Astrophysics*, 536, p. A78. doi:10.1051/0004-6361/201117367.

Kubo, H., Takahashi, T., Madejski, G., *et al.* (1998) 'ASCA Observations of Blazars and Multiband Analysis', *The Astrophysical Journal*, 504, pp. 693–701. doi:10.1086/306125.

Landt, H., Padovani, P., Perlman, E.S., *et al.* (2004) 'A physical classification scheme for blazars', *Monthly Notices of the Royal Astronomical Society*, 351, pp. 83–100. doi:10.1111/j.1365-2966.2004.07750.x.

Larson, D., Dunkley, J., Hinshaw, G., *et al.* (2011) 'Seven-year Wilkinson Microwave Anisotropy Probe (WMAP) Observations: Power Spectra and WMAP-derived Parameters', *The Astrophysical Journal Supplement Series*, 192, p. 16. doi:10.1088/0067-0049/192/2/16.

Liodakis, I., Hovatta, T., Huppenkothen, D., *et al.* (2018) 'Constraining the limiting brightness temperature and Doppler factors for the largest Sample of radio-bright blazars', *The Astrophysical Journal*, 866, p. 137. doi:10.3847/1538-4357/aae2b7.

Lister, M.L., Aller, H. D., Aller, M.F., *et al.* (2009) 'MOJAVE: Monitoring of Jets in Active Galactic Nuclei with VLBA Experiments. VI. Kinematics Analysis of a Complete Sample of Blazar Jets', *The Astronomical Journal*, 138, pp. 1874–1892. Available at: https://doi.org/10.1088/0004-6256/138/6/1874.

Lucchini, M., Markoff, S., Crumley, P., *et al.* (2019) 'Breaking degeneracy in jet dynamics: multi-epoch joint modelling of the BL Lac PKS 2155–304', *Monthly Notices of the Royal Astronomical Society*, 482(4), pp. 4798–4812. doi:10.1093/mnras/sty2929.

Lyutikov, M., Komissarov, S., Sironi, L., *et al.* (2018) 'Particle acceleration in explosive relativistic reconnection events and Crab Nebula Gamma-ray flares,' *Journal of Plasma Physics*, 84, p. 635840201. doi:10.1017/S0022377818000168.

Marcha, M.J.M., Browne, I.W.A., Impey, C.D., *et al.* (1996) 'Optical spectroscopy and polarization of a new sample of optically bright flat radio spectrum sources', *Monthly Notices of the Royal Astronomical Society*, 281, pp. 425–448. doi:10.1093/mnras/281.2.425.

Marcha, M.J.M. and Browne, I.W.A. (1996) 'The prediction of the spectral properties of BL Lac samples', *Monthly Notices of the Royal Astronomical Society*, 279, pp. 72–78. doi:10.1093/mnras/279.1.72.

Marscher, A.P. (2016) ‘Variability of Blazars and Blazar Models over 38 Years’, *Galaxies*, 4(4), p. 37. doi:10.3390/galaxies4040037.

Massaro, E., Tramacere, A., Perri, M., *et al.* (2006) ‘Log-parabolic spectra and particle acceleration in blazars. III. SSC emission in the TeV band from Mkn501’, *Astronomy and Astrophysics*, 448(3), pp. 861–871. doi:10.1051/0004-6361:20053644.

Mattox, J.R., Bertsch, D.L., Chiang, J., *et al.* (1996) ‘The likelihood analysis of EGRET Data,’ *The Astrophysical Journal*, 461, p. 396. doi:10.1086/177068.

Max-Moerbeck, W., Hovatta, T., Richards, J.L., *et al.* (2014) ‘Time correlation between the radio and Gamma-ray activity in blazars and the production site of the Gamma-ray emission’, *Monthly Notices of the Royal Astronomical Society*, 445, pp. 428–436. doi:10.1093/mnras/stu1749.

Mereu, I. (2020) ‘Fermi-LAT detection of record Gamma-ray flare in BL Lacertae contemporaneous with record X-ray flare’, *The Astronomer’s Telegram*, 14072, p. 1.

Meyer, M., Scargle, J.D. and Blandford, R.D. (2019) ‘Characterizing the Gamma-ray Variability of the Brightest Flat Spectrum Radio Quasars Observed with the Fermi LAT’, *The Astrophysical Journal*, 877, p. 39. doi:10.3847/1538-4357/ab1651.

Miller, J.S. and Hawley, S.A. (1977) ‘The Spectrum and Redshift of BL Lacertae’, *The Astrophysical Journal*, 212, p. L47. doi:10.1086/182372.

Morris, P.J., Potter, W.J. and Cotter, G. (2019) ‘The feasibility of magnetic reconnection powered blazar flares from synchrotron self-Compton emission’, *Monthly Notices of the Royal Astronomical Society*, 486, pp. 1548–1562. doi:10.1093/mnras/stz920.

Mura, G.L. (2021) ‘Fermi-LAT detection of enhanced Gamma-ray activity from BL Lac’, *The Astronomer’s Telegram*, 14583, p. 1.

Nalewajko, K. (2013) ‘The brightest Gamma-ray flares of blazars’, *Monthly Notices of the Royal Astronomical Society*, 430(2), pp. 1324–1333. doi:10.1093/mnras/sts711.

Nesci, R., Massaro, E., Maesano, M., *et al.* (2002) ‘Optical and Radio Monitoring of S5 1803+784’, *The Astronomical Journal*, 124, pp. 53–64. Available at: https://doi.org/10.1086/341038.

Nesci, R., Cutini, S., Stanghellini, C., *et al.* (2021) ‘Multiwavelength flare observations of the blazar S5 1803+784’, *Monthly Notices of the Royal Astronomical Society*, 502(4), pp. 6177–6187. doi:10.1093/mnras/stab501.

Nilsson, K., Lindfors, E., Takalo, L.O., *et al.* (2018) ‘Long-term optical monitoring of TeV emitting blazars. I. Data analysis’, *Astronomy & Astrophysics, Volume 620, id.A185, pp.*, 620, p. A185. doi:10.1051/0004-6361/201833621.

Nolan, P.L., Abdo, A.A., Ackermann, M., *et al.* (2012) ‘Fermi Large Area Telescope second source catalog’, *The Astrophysical Journal Supplement Series*, 199, p. 31. doi:10.1088/0067-0049/199/2/31.

Ojha, R. and Valverd, J. (2020) ‘Fermi-LAT detection of record Gamma-ray flare in BL Lacertae contemporaneous with record optical flaring’, *The Astronomer’s Telegram*, 13964, p. 1.

Padovani, P., Oikonomou, F., Petropoulou, M., *et al.* (2019) ‘TXS 0506+056, the first cosmic neutrino source, is not a BL Lac’, *Monthly Notices of the Royal Astronomical Society: Letters*, 484(1), pp. L104–L108. doi: 10.1093/mnrasl/slz011.

Paliya, V.S., Marcotulli, L., Ajello, M., *et al.* (2017) ‘General Physical Properties of CGRaBS Blazars’, *The Astrophysical Journal*, 851, p. 33. doi:10.3847/1538-4357/aa98e1.

Pittori, C., Verrecchia, F., Chen, A.W., *et al.* (2009) ‘First AGILE catalog of high-confidence Gamma-ray sources’, *Astronomy and Astrophysics, Volume 506, Issue 3, 2009, pp.1563-1574*, 506(3), p. 1563. doi:10.1051/0004-6361/200911783.

Prince, R., Gupta, N. and Nalewajko, K. (2019) ‘Two-zone Emission Modeling of PKS 1510-089 during the High State of 2015’, *The Astrophysical Journal*, 883, p. 137. Available at: https://doi.org/10.3847/1538-4357/ab3afa.

Prince, R., Khatoon, R. and Agarwal, A. (2021) ‘Swift XRT/UVOT follow-up of the recent optical activity of blazar BL Lacertae’, *The Astronomer’s Telegram*, 14774, p. 1.

Priya, S., Prince, R., Agarwal, A., *et al.* (2022) ‘Multiwavelength temporal and spectral analysis of Blazar S5 1803+78’, *Monthly Notices of the Royal Astronomical Society*, 513, pp. 2239–2251. doi:10.1093/mnras/stac1009.

Raiteri, C.M., Villata, M., Capetti, A., *et al.* (2009) ‘WEBT multiwavelength monitoring and XMM-Newton observations of BL Lacertae in 2007-2008. Unveiling different emission components’, *Astronomy and Astrophysics*, 507(2), pp. 769–779. doi:10.1051/0004-6361/200912953.

Rajput, B., Stalin, C.S. and Rakshit, S. (2020) ‘Long term Gamma-ray variability of blazars,’ *Astronomy & Astrophysics*, 634, p. A80. doi:10.1051/0004-6361/201936769.

Rajput, B. and Pandey, A. (2021) ‘Gamma-ray Flux and Spectral Variability of Blazar Ton 599 during Its 2021 Flare’, *Galaxies*, 9, p. 118. doi:10.3390/galaxies9040118.

Ravasio, M., Tagliaferri, G., Ghisellini, G., *et al.* (2002) ‘BL Lacertae: Complex spectral variability and rapid synchrotron flare detected with BeppoSAX’, *Astronomy and Astrophysics*, 383, pp. 763–772. doi:10.1051/0004-6361:20011828.

Richards, J.L., Max-Moerbeck, W., Pavlidou, V., *et al.* (2011) ‘Blazars in the Fermi era: The OVRO 40 m Telescope Monitoring Program’, *The Astrophysical Journal Supplement Series*, 194, p. 29. doi:10.1088/0067-0049/194/2/29.

Robertson, D.R.S., Gallo, L.C., Zoghbi, A., *et al.* (2015) ‘Searching for correlations in simultaneous X-ray and UV emission in the narrow-line Seyfert 1 galaxy 1H 0707-495’, *Monthly Notices of the Royal Astronomical Society*, 453, pp. 3455–3460. doi:10.1093/mnras/stv1575.

Romero, G.E., Böttcher, M., Markoff, S., *et al.* (2017) 'Relativistic jets in Active Galactic Nuclei and Microquasars,' *Space Science Reviews*, 207, pp. 5–61. doi:10.1007/s11214-016-0328-2.

Rybicki, G.B. and Lightman, A.P. (2004) *Radiative processes in astrophysics*. Weinheim: Wiley (Physics textbook).

Saito, S., Stawarz, L., Tanaka, Y.T., *et al.* (2013) 'Very rapid high-amplitude Gamma-ray variability in luminous blazar Pks 1510−089 Studied with Fermi-LAT', *The Astrophysical Journal Letters*, 766(1), p. L11. doi:10.1088/2041-8205/766/1/L11.

Sbarrato, T., Padovani, P. and Ghisellini, G. (2014) 'The jet-disc connection in AGN', *Monthly Notices of the Royal Astronomical Society*, 445, pp. 81–92. doi:10.1093/mnras/stu1759.

Scargle, J.D., Norris, J.P., Jackson, B., *et al.* (2013) 'Studies in Astronomical Time Series Analysis. VI. Bayesian Block Representations', *The Astrophysical Journal*, 764, p. 167. doi:10.1088/0004-637X/764/2/167.

Schlafly, E.F. and Finkbeiner, D.P. (2011) 'Measuring Reddening with Sloan Digital Sky Survey Stellar Spectra and Recalibrating SFD', *The Astrophysical Journal*, 737, p. 103. doi:10.1088/0004-637X/737/2/103.

Sikora, M., Stawarz, Ł., Moderski, R., *et al.* (2009) 'Constraining Emission Models of Luminous Blazar Sources', *The Astrophysical Journal*, 704, pp. 38–50. doi:10.1088/0004-637X/704/1/38.

Sillanpaa, A., Haarala, S., Valtonen, M. J., *et al.* (1988) 'OJ 287: Binary pair of supermassive black holes', *The Astrophysical Journal*, 325, p. 628. doi:10.1086/166033.

Singh, K.K., Sahayanathan, S., Sinha, A., *et al.* (2017) 'A time dependent approach to model X-ray and Gamma-ray light curves of Mrk 421 observed during the flare in February 2010', *New Astronomy*, 54, pp. 24–29. doi:10.1016/j.newast.2016.12.003.

Sironi, L., Petropoulou, M. and Giannios, D. (2015) 'Relativistic Jets Shine through Shocks or Magnetic Reconnection', *undefined* [Preprint]. Available at: https://www.semanticscholar.org/paper/Applying-Relativistic-Reconnection-to-Blazar-Jets-Marscher-Jorstad/215317b8f2f8113ca73181ee990896cf1653c9bf (Accessed: 21 September 2021).

Sironi, L., Petropoulou, M. and Giannios, D. (2015) 'Relativistic jets shine through shocks or magnetic reconnection?', *Monthly Notices of the Royal Astronomical Society*, 450, pp. 183–191. doi:10.1093/mnras/stv641.

Sironi, L. and Spitkovsky, A. (2014) 'Relativistic Reconnection: An efficient source of non-thermal particles', *Astrophysical Journal Letters*, 783(1). doi:10.1088/2041-8205/783/1/L21.

Tavecchio, F., Ghisellini, G., Ghirlanda, G., *et al.* (2010) 'TeV BL Lac objects at the dawn of the Fermi era,' *Monthly Notices of the Royal Astronomical Society*, 401, pp. 1570–1586. doi:10.1111/j.1365-2966.2009.15784.x.

Tavecchio, F. and Ghisellini, G. (2008) 'The spectrum of the broad-line region and the high-energy emission of powerful blazars', *Monthly Notices of the Royal Astronomical Society*, 386(2), pp. 945–952. doi:10.1111/j.1365-2966.2008.13072.x.

Thompson, A.R., Moran, J. and Swenson, G.W. (2017) *Interferometry and Synthesis in Radio Astronomy*. 3rd edn. Springer International Publishing (Astronomy and Astrophysics Library). doi:10.1007/978-3-319-44431-4.

Tramacere, A., Giommi, P., Perri, M., *et al.* (2009) 'Swift observations of the very intense flaring activity of Mrk 421 during 2006. I. Phenomenological picture of electron acceleration and predictions for MeV/GeV emission', *Astronomy and Astrophysics*, 501(3), pp. 879–898. doi:10.1051/0004-6361/200810865.

Tramacere, A. (2020) 'JetSeT: Numerical modeling and SED fitting tool for relativistic jets', *Astrophysics Source Code Library*, p. ascl:2009.001.

Tramacere, A., Massaro, E. and Taylor, A.M. (2011) 'Stochastic Acceleration and the Evolution of Spectral Distributions in Synchro-Self-Compton Sources: A Self-consistent Modeling of Blazars' Flares', *The Astrophysical Journal*, 739, p. 66. doi:10.1088/0004-637X/739/2/66.

Urry, C.M. and Padovani, P. (1995) 'Unified Schemes for Radio-Loud Active Galactic Nuclei', *Publications of the Astronomical Society of the Pacific*, 107, p. 803. doi:10.1086/133630.

Uzdensky, D. A. (2016) 'Radiative Magnetic Reconnection in Astrophysics', in Gonzalez, W. and Parker, E. (eds) *Magnetic Reconnection: Concepts and Applications*. Cham: Springer International Publishing (Astrophysics and Space Science Library), pp. 473–519. doi:10.1007/978-3-319-26432-5_12.

Vaughan, S., Edelson, R., Warwick, R.S., *et al.* (2003) 'On characterizing the variability properties of X-ray light curves from active galaxies', *Monthly Notices of the Royal Astronomical Society*, 345, pp. 1271–1284. doi:10.1046/j.1365-2966.2003.07042.x.

Venters, T., Angioni, R. and Ojha, R. (2020) 'Fermi-LAT Detection of a Bright Gamma-ray Flare in the BL Lac S5 1803+784', *The Astronomer's Telegram*, 13633, p. 1.

Wani, K.A. and Gaur, H. (2020) 'X-ray Flux and Spectral Variability of Blazar H 2356-309', *Galaxies*, 8, p. 59. doi:10.3390/galaxies8030059.

Weisskopf, M.C. (2018) 'An Overview of X-Ray Polarimetry of Astronomical Sources', *Galaxies*, 6(1), p. 33. Available at: https://doi.org/10.3390/galaxies6010033.

Weisskopf, M.C., Soffitta, P., Baldini, L., *et al.* (2022) 'The Imaging X-Ray Polarimetry Explorer (IXPE): Pre-Launch', *Journal of Astronomical Telescopes, Instruments, and Systems*, 8, p. 026002. Available at: https://doi.org/10.1117/1.JATIS.8.2.026002.

Werner, G.R., Philippov, A.A. and Uzdensky, D.A. (2019) 'Particle acceleration in relativistic magnetic reconnection with strong inverse-Compton cooling in pair plasmas', *Monthly Notices of the Royal Astronomical Society: Letters*, 482(1), pp. L60–L64. doi:10.1093/mnrasl/sly157.

Wilms, J., Allen, A. and McCray, R. (2000) 'On the Absorption of X-Rays in the Interstellar Medium', *The Astrophysical Journal*, 542, pp. 914–924. doi:10.1086/317016.

Wilson, A.S. and Colbert, E.J.M. (1995) 'The Difference between Radio-loud and Radio-quiet Active Galaxies', *The Astrophysical Journal*, 438, p. 62. doi:10.1086/175054.

Wood, M., Caputo, R., Charles, E., *et al.* (2017) 'Fermipy: An open-source Python package for analysis of Fermi-LAT Data', 35th International Cosmic Ray Conference. 10-20 July 2017. Bexco, Busan, Korea, Proceedings of Science, Vol. 301. Online at https://pos.sissa.it/cgi-bin/reader/conf.cgi?confid=301, id.824.

Xue-Pin, W., Xiong-Wei, B. and Yong-Gang, Z. (2018) 'Study on the Properties of Blazar Jets', *Chinese Astronomy and Astrophysics*, 42(3), pp. 360–378. doi:10.1016/j.chinastron.2018.09.003.

Zank, G.P., Hunana, P., Mostafavi, P., *et al.* (2015) 'Diffusive Shock Acceleration and Reconnection Acceleration Processes', *The Astrophysical Journal*, 814(2), p. 137. doi:10.1088/0004-637X/814/2/137.

Zenitani, S. and Hoshino, M. (2007) 'Particle Acceleration and Magnetic Dissipation in Relativistic Current Sheet of Pair Plasmas'. doi:10.1086/522226.

Zhang, H. and Böttcher, M. (2013) 'X-Ray and Gamma-ray Polarization in Leptonic and Hadronic Jet Models of Blazars', *The Astrophysical Journal*, 774, p. 18. Available at: https://doi.org/10.1088/0004-637X/774/1/18.

Zhang, H., Chen, X., Böttcher, M., *et al.* (2015) 'Polarization Swings Reveal Magnetic Energy Dissipation in Blazars', *The Astrophysical Journal*, 804, p. 58. doi:10.1088/0004-637X/804/1/58.

Zhang, H., Deng, W., Li, H., *et al.* (2016) 'Polarization signatures of relativistic magnetohydrodynamic shocks in the blazar emission region. I. Force-free Helical Magnetic Fields', *The Astrophysical Journal*, 817, p. 63. doi:10.3847/0004-637X/817/1/63.

APPENDIX

SSC+EC sample code

JetSeT_Sample code set-up

```
[ ]: import warnings
     warnings.filterwarnings('ignore')
     import matplotlib.pylab as plt
     import jetset
     from jetset.jet_model import Jet
     from jetset.test_data_helper import test_SEDs
     from jetset.data_loader import ObsData,Data
     from jetset.plot_sedfit import PlotSED
```

```
[ ]: #importing ASCII file to astropy table format
     from jetset.data_loader import Data
     import matplotlib
     import numpy as np

     d=np.genfromtxt('BL_Lacertae_Quiescent.txt')#name of the ASCII file
     data=Data(n_rows=d.shape[0])
     data.set_field('x',d[:,0]) #Frequency column
     data.set_field('y',d[:,1]) #Nu_F_Nu column erg cm^-2 s^-1
     data.set_field('dy',value=d[:,2]) #error in Nu_F_Nu
```

```
[ ]: #set the metadata
     data.set_meta_data('z',0.0686) #redshift #logarithm scale
     data.set_meta_data('restframe','obs') #obs(observer frame)flux or src (source␣
      ↪frame)luminosity
     data.set_meta_data('data_scale','log-log') #logarithm scale
     data.set_meta_data('UL_CL','0.95') #confidence level
     data.set_meta_data('obj_name','BL Lacertae[Quiescent]') #object name 4FGL J2202.
      ↪7+4216,
```

```
[ ]: data.table
```

```
[ ]: %matplotlib inline
     from jetset.cosmo_tools import Cosmo
     c=Cosmo()
     #c=Cosmo(DL_cm=9.4311e26) #BL Lacertae DL= 9.4311e26 luminosity distance
```

```
sed_data=ObsData(data_table=data,cosmo=c)
sed_data.group_data(bin_width=0.1)
sed_data.add_systematics(0.2,[10.**6,10.**29])# add 20% systematics for data␣
↪between 10^6<ν<10^29Hz
```

[ ]:
```
sed_data.save('Blacertae_flareB1_EC.pkl')
```

[ ]:
```
from jetset.sed_shaper import  SEDShape
my_shape=SEDShape(sed_data)
my_shape.eval_indices(silent=True)
p=my_shape.plot_indices()
p.rescale(y_min=-15,y_max=-6)
```

[ ]:
```
m,best_fit=my_shape.sync_fit(check_BBB_template=True,
                             check_host_gal_template=False,
                             use_log_par=True,
                             Ep_start=None,
                             minimizer='minuit',
                             silent=False,
                             fit_range=[10,17.0])
```

[ ]:
```
my_shape.IC_fit(fit_range=[17,26],minimizer='minuit', silent=True)
p=my_shape.plot_shape_fit()
p.rescale(y_min=-15)
#plt.savefig('Flare_A003.png', dpi=1000)
```

[ ]:
```
from jetset.obs_constrain import ObsConstrain
from jetset.model_manager import  FitModel
from jetset.minimizer import fit_SED
sed_obspar=ObsConstrain(beaming=14.70,
                        B_range=[0.00011,0.706],
                        distr_e='bkn',
                        t_var_sec=6.0*86400,   #8 'EC_DT''EC_DT',
                        nu_cut_IR=3.0E12,
                        SEDShape=my_shape)
prefit_jet=sed_obspar.
↪constrain_SSC_EC_model(electron_distribution_log_values=False,EC_componets_list=['EC_BLR'],
```

[ ]:
```
# BLR
#from jetset.jet_model import Jet
#my_jet=Jet(name='BLR␣
↪example',electron_distribution='bkn',beaming_expr='bulk_theta')
#my_jet.add_EC_component(['EC_BLR','EC_Disk'],disk_type='BB')
```

[ ]:
```
prefit_jet.eval()
p=prefit_jet.plot_model(sed_data=sed_data)
p.add_residual_plot(prefit_jet,sed_data)
```

```
prefit_jet.save_model('prefit_jetBL_EC.pkl')
```

[ ]:
```
jet_minuti=Jet.load_model('prefit_jetBL_EC.pkl')
jet_minuti.set_gamma_grid_size(100)
fit_model_minuit=FitModel( jet=jet_minuti, name='EC-best-fit-minuit')
fit_model_minuit.show_model_components()
```

[ ]:
```
jet_minuti=Jet.load_model('prefit_jetBL_EC.pkl')
jet_minuti.set_gamma_grid_size(100)
fit_model_minuit=FitModel( jet=jet_minuti, name='EC-best-fit-minuit')
fit_model_minuit.freeze('jet_leptonic','z_cosm')
fit_model_minuit.freeze('jet_leptonic','R_H')
fit_model_minuit.freeze('jet_leptonic','L_Disk')
fit_model_minuit.freeze('jet_leptonic','R')
fit_model_minuit.freeze('jet_leptonic','R_BLR_in')
fit_model_minuit.freeze('jet_leptonic','R_BLR_out')
#fit_model_minuit.freeze('jet_leptonic','T_DT')
#fit_model_minuit.freeze('jet_leptonic','tau_DT')
fit_model_minuit.freeze('jet_leptonic','tau_BLR')
fit_model_minuit.freeze('jet_leptonic','T_Disk')
fit_model_minuit.jet_leptonic.parameters.R.fit_range=[1E15,5E17]
#fit_model_minuit.jet_leptonic.parameters.gamma_break.val=500
fit_model_minuit.jet_leptonic.parameters.p.val=2.5
fit_model_minuit.jet_leptonic.parameters.gamma_break.fit_range=[100,1500]
fit_model_minuit.jet_leptonic.parameters.gmin.fit_range=[2,35]
fit_model_minuit.jet_leptonic.parameters.gmax.val=1E5
fit_model_minuit.jet_leptonic.parameters.gmax.fit_range=[1000,1E6]
#fit_model_minuit.jet_leptonic.parameters.tau_DT.val=0.01
fit_model_minuit.jet_leptonic.parameters.tau_BLR.val=0.13
fit_model_minuit.jet_leptonic.parameters.p_1.val=2.0
#fit_model_minuit.jet_leptonic.parameters.T_DT.val=1E3
#fit_model_minuit.jet_leptonic.parameters.R_BLR_in.val=9.534279e+15
#fit_model_minuit.jet_leptonic.parameters.R_BLR_out.val=1.906856e+16
#fit_model_minuit.jet_leptonic.parameters.L_Disk.val=6.12e+44 #9.090248e+42 #
#fit_model_minuit.jet_leptonic.parameters.R_H.val=1.3699e+17
#fit_model_minuit.jet_leptonic.parameters.beam_obj.fit_range=[3,50]
```

[ ]:
```
from jetset.minimizer import ModelMinimizer
model_minimizer_minuit=ModelMinimizer('minuit')
best_fit_minuit=model_minimizer_minuit.
 ↪fit(fit_model_minuit,sed_data,1E11,1E29,fitname='EC-best-fit-minuit',repeat=3)
```

[ ]:
```
best_fit_minuit.save_report('EC-BL-best-fit-minuit.txt')
model_minimizer_minuit.save_model('EC_BL_model_minimizer_minuit.pkl')
fit_model_minuit.save_model('EC_BL_fit_model_minuit.pkl')
```

[ ]:
```
%matplotlib inline
fit_model_minuit.set_nu_grid(1E6,1E30,200)
fit_model_minuit.eval()
p2=fit_model_minuit.plot_model(sed_data=sed_data)
p2.rescale(y_min=-15,y_max=-8.5,x_min=6.0,x_max=28.5)
plt.savefig('Flare_A3.png', dpi=1000)
```

[ ]:
```
jet_minuti.energetic_report()
```

[ ]:
```
model_minimizer_minuit.minimizer.mesg
```

[ ]:
```
########MCMC#################################
```

[ ]:
```
from jetset.mcmc import McmcSampler
from jetset.minimizer import ModelMinimizer
```

[ ]:
```
model_minimizer_minuit = ModelMinimizer.
 ↪load_model('EC_BL_model_minimizer_minuit.pkl')


mcmc=McmcSampler(model_minimizer_minuit)

labels=['N','beam_obj','p_1','gamma_break','gmin','gmax','p','R','B']
model_name='jet_leptonic'
use_labels_dict={model_name:labels}

mcmc.run_sampler(nwalkers=128,burnin=10,steps=150,bound=8.
 ↪0,bound_rel=True,threads=None,walker_start_bound=0.
 ↪005,use_labels_dict=use_labels_dict)
```

[ ]:
```
print(mcmc.acceptance_fraction)
```

[ ]:
```
f=mcmc.corner_plot()
```

[ ]:
```
f=mcmc.plot_chain('p_1',log_plot=False)
```

[ ]:
```
mcmc.save('mcmc_BL_EC_Flare_sampler.pkl')
```

[ ]:
```
from jetset.mcmc import McmcSampler
from jetset.data_loader import ObsData
from jetset.plot_sedfit import PlotSED
from jetset.test_data_helper import  test_SEDs

sed_data=ObsData.load('Blacertae_flareB1_EC.pkl')#####

ms=McmcSampler.load('mcmc_BL_EC_Flare_sampler.pkl')
ms.model.set_nu_grid(1E6,1E30,200)
```

```
p=ms.plot_model(sed_data=sed_data,fit_range=[10.,27.4],size=50)
p.rescale(y_min=-16,x_min=6,x_max=28.5)
plt.savefig('A3.png', dpi=1000)
```

[ ]:
```
f=ms.plot_par('beam_obj',log_plot=False)
```

[ ]:
```
##########################################################################3
```

[ ]:
```
f=ms.corner_plot()
```

[ ]:
```
#########################################################################################
```

Synchrotron+SSC-only code set-up

Synchrotron+SSC only JetSeT code set-up

[ ]:
```
import warnings
warnings.filterwarnings('ignore')
import matplotlib.pylab as plt
from jetset.test_data_helper import test_SEDs
from jetset.data_loader import ObsData,Data
from jetset.plot_sedfit import PlotSED
from jetset.test_data_helper import test_SEDs
```

[ ]:
```
#importing ASCII file to astropy table format
from jetset.data_loader import Data
import matplotlib
import numpy as np

d=np.genfromtxt('S51803+784_Quiescent.txt')#name of the ASCII file
data=Data(n_rows=d.shape[0])
data.set_field('x',d[:,0]) #Frequency column
data.set_field('y',d[:,1]) #Nu_F_Nu column erg cm^-2 s^-1
data.set_field('dy',value=d[:,2]) #error in Nu_F_Nu
```

[ ]:
```
#set the metadata
data.set_meta_data('z',0.684) #redshift
data.set_meta_data('restframe','obs') #obs(observer frame)flux or src (source␣
↪frame)luminosity
data.set_meta_data('data_scale','log-log') #logarithm scale
data.set_meta_data('UL_CL','0.95') #confidence level
data.set_meta_data('obj_name','S5 1803+784[Quiescent]') #object name 4FGL J1800.
↪6+7828,
```

[ ]:
```
data.table
```

[ ]:
```
%matplotlib inline
from jetset.cosmo_tools import Cosmo
c=Cosmo()
sed_data=ObsData(data_table=data,cosmo=c)
sed_data.group_data(bin_width=0.2)
sed_data.add_systematics(0.2,[10.**6,10.**29])
```

[ ]:
```
sed_data.save('S51803+784_catalog.pkl')
```

[ ]:
```
p=sed_data.plot_sed()
```

[ ]:
```
from jetset.sed_shaper import SEDShape
my_shape=SEDShape(sed_data)
my_shape.eval_indices()
p=my_shape.plot_indices()
p.rescale(y_min=-15,y_max=-7)
```

[ ]:
```
mm,best_fit=my_shape.
 ↪sync_fit(check_host_gal_template=False,Ep_start=None,minimizer='minuit',silent=True,fit_ran
 ↪,17,])
```

[ ]:
```
mm,best_fit=my_shape.
 ↪sync_fit(check_host_gal_template=False,Ep_start=None,minimizer='minuit',silent=True,fit_ran
 ↪,17.,])
mm.minimizer.minos_errors()
x,y,z,fig,ax=mm.minimizer.draw_contour('Ep','b')
x,y,fig,ax=mm.minimizer.draw_profile('Ep')
```

[ ]:
```
my_shape.IC_fit(fit_range=[17,29],minimizer='minuit')
p=my_shape.plot_shape_fit()
p.rescale(y_min=-15,x_min=7,x_max=29)
```

[ ]:
```
from jetset.obs_constrain import ObsConstrain
from jetset.model_manager import  FitModel
sed_obspar=ObsConstrain(beaming=26.65,
                        B_range=[0.01,0.09],
                        distr_e='bkn',
                        t_var_sec=20.50*86400,
                        nu_cut_IR=5.0E11,
                        SEDShape=my_shape)

prefit_jet=sed_obspar.
 ↪constrain_SSC_model(electron_distribution_log_values=False,silent=True)
prefit_jet.save_model('prefit_S5_catalog_jet.pkl')
```

[ ]:
```
prefit_jet.eval()
pl=prefit_jet.plot_model(sed_data=sed_data)
pl.add_residual_plot(prefit_jet,sed_data)
pl.rescale(y_min=-15,x_min=7,x_max=29)
```

[ ]:
```
from IPython.core.display import HTML
HTML("""
<style>
.output_png {
```

```
    display: table-cell;
    text-align: center;
    vertical-align: middle;
}
</style>
""")
```

[ ]:
```
from jetset.minimizer import fit_SED,ModelMinimizer

from jetset.model_manager import  FitModel
from jetset.jet_model import Jet
```

[ ]:
```
jet_minuit=Jet.load_model('prefit_S5_catalog_jet.pkl')
jet_minuit.set_gamma_grid_size(200)

fit_model_minuit=FitModel( jet=jet_minuit,␣
 ↪name='SSC-best-fit-minuit',template=None)
```

[ ]:
```
fit_model_minuit.show_model_components()
```

[ ]:
```
#Minuit
fit_model_minuit.freeze('jet_leptonic','z_cosm')
fit_model_minuit.freeze('jet_leptonic','R_H')
fit_model_minuit.freeze('jet_leptonic','beam_obj')
#fit_model_minuit.freeze('jet_leptonic','R')
#fit_model_minuit.freeze('jet_leptonic','gmax')
fit_model_minuit.jet_leptonic.parameters.R.fit_range=[10**15.5,10**17.5]
fit_model_minuit.jet_leptonic.parameters.beam_obj.fit_range=[5,50]
fit_model_minuit.jet_leptonic.parameters.gmax.fit_range=[1000,1E6]
fit_model_minuit.jet_leptonic.parameters.R_H.val=4.9999E17
fit_model_minuit.jet_leptonic.parameters.beam_obj.val=12.2
```

[ ]:
```
model_minimizer_minuit=ModelMinimizer('minuit')
best_fit_minuit=model_minimizer_minuit.fit(fit_model_minuit,sed_data,10**11.
 ↪,10**29.0,fitname='SSC-best-fit-minuit',repeat=3)
```

[ ]:
```
model_minimizer_minuit.minimizer.mesg
```

[ ]:
```
best_fit_minuit.save_report('SSC-best-fit-S5-catalog-minuit.txt')
model_minimizer_minuit.save_model('model_minimizer_S5catalog_minuit.pkl')
fit_model_minuit.save_model('fit_model_S5catalog_minuit.pkl')
```

[ ]:
```
best_fit_minuit.bestfit_table
```

[ ]:
```
%matplotlib inline
fit_model_minuit.eval()
p2=fit_model_minuit.plot_model(sed_data=sed_data)
```

```
p2.rescale(y_min=-16,x_min=7,x_max=28.5)
plt.savefig('S5_SSCQ1.png', dpi=1000)
```

[ ]:
```
##########################MCMC#################SAMPLING##########################
```

[ ]:
```
from jetset.mcmc import McmcSampler
from jetset.minimizer import ModelMinimizer
```

[ ]:
```
model_minimizer_minuit = ModelMinimizer.
 ↪load_model('model_minimizer_S5catalog_minuit.pkl')

mcmc=McmcSampler(model_minimizer_minuit)

labels=['N','B','p','p_1','gmin','gmax','gamma_break','R']
model_name='jet_leptonic'
use_labels_dict={model_name:labels}

mcmc.run_sampler(nwalkers=128,burnin=10,steps=100,bound=5.
 ↪0,bound_rel=True,threads=None,walker_start_bound=0.
 ↪005,use_labels_dict=use_labels_dict)
```

[ ]:
```
mcmc.save('mcmc_sampler_S5_catalog.pkl')
```

[ ]:
```
print(mcmc.acceptance_fraction)
```

[ ]:
```
from jetset.mcmc import McmcSampler
from jetset.data_loader import ObsData
from jetset.plot_sedfit import PlotSED
from jetset.test_data_helper import  test_SEDs

sed_data=ObsData.load('S51803+784_catalog.pkl')#####

ms=McmcSampler.load('mcmc_sampler_S5_catalog.pkl')
```

[ ]:
```
ms.model.set_nu_grid(1E6,1E30,200)

p=ms.plot_model(sed_data=sed_data,fit_range=[10., 28.5],size=50)
p.rescale(y_min=-16,x_min=7,x_max=28.5)
plt.savefig('S5_SSCQ2.png', dpi=1000)
```

[ ]:
```
f=mcmc.corner_plot()
```

[ ]:
```

```

Two_zone_model_Sample_code

August 1, 2022

[ ]:
```
##############TWO ZONE Model, Synchrotron+SSC, and EC
```

[ ]:
```
import warnings
warnings.filterwarnings('ignore')
import matplotlib.pylab as plt
import jetset
from jetset.jet_model import Jet
from jetset.test_data_helper import test_SEDs
from jetset.data_loader import ObsData,Data
from jetset.plot_sedfit import PlotSED
from jetset.model_manager import FitModel
```

[ ]:
```
#importing ASCII file to astropy table format
from jetset.data_loader import Data
import matplotlib
import numpy as np

d=np.genfromtxt('FLARE_ASED.txt')#name of the ASCII file bllac_sim.txt
data=Data(n_rows=d.shape[0])
data.set_field('x',d[:,0]) #Frequency column
data.set_field('y',d[:,1]) #Nu_F_Nu column erg cm^-2 s^-1
data.set_field('dy',value=d[:,2]) #error in Nu_F_Nu
```

[ ]:
```
#set the metadata
data.set_meta_data('z',0.0686) #redshiftogarithm scaledata.
 ↪set_meta_data('data_scale','log-log') #logarithm scale
data.set_meta_data('restframe','obs') #obs(observer frame)flux or src (source␣
 ↪frame)luminosity
data.set_meta_data('data_scale','log-log') #logarithm scale
data.set_meta_data('UL_CL','0.95') #confidence level
data.set_meta_data('obj_name','BL Lacertae[Flare A1]') #object name4FGL J2202.
 ↪7+4216,
```

[ ]:
```
data.table
```

[ ]:
```
%matplotlib inline
from jetset.cosmo_tools import Cosmo
```

```
c=Cosmo()
#c=Cosmo(DL_cm=9.4311e26) #BL Lacertae DL= 9.4311e26 luminosity distance
sed_data=ObsData(data_table=data,cosmo=c)
sed_data.group_data(bin_width=0.1)
sed_data.add_systematics(0.2,[10.**6,10.**29])# add 20% systematics for data
 ↪between 10^6<ν<10^29Hz
sed_data.save('Blacertae_flare_jet.pkl')
```

[ ]:
```
p=sed_data.plot_sed()
```

[ ]:
```
from jetset.sed_shaper import  SEDShape
my_shape=SEDShape(sed_data)
my_shape.eval_indices(silent=True)
p=my_shape.plot_indices()
p.setlim(y_min=1E-18,y_max=1E-6)
```

[ ]:
```
from jetset.sed_shaper import  SEDShape
my_shape=SEDShape(sed_data)
my_shape.eval_indices(silent=True)
p=my_shape.plot_indices()
p.setlim(y_min=1E-18,y_max=1E-6)
```

[ ]:
```

```

[ ]:
```
mm,best_fit=my_shape.sync_fit(check_BBB_template=True,
                              check_host_gal_template=False,
                              use_log_par=True,
                              Ep_start=None,
                              minimizer='minuit',
                              silent=True,
                              fit_range=[6.5, 15.5])
```

[ ]:
```
my_shape.IC_fit(fit_range=[17.0, 26.],minimizer='minuit',silent=True)
p=my_shape.plot_shape_fit()
p.setlim(y_min=1E-18)
```

[ ]:
```
from jetset.obs_constrain import ObsConstrain
from jetset.model_manager import FitModel
from jetset.minimizer import fit_SED
sed_obspar=ObsConstrain(beaming=6.60,
                        B_range=[0.00001,0.40], #3 5
                        distr_e='bkn',
                        t_var_sec=6.0*86400, #3
                        nu_cut_IR=3.0E12,
                        SEDShape=my_shape)
prefit_jet=sed_obspar.
 ↪constrain_SSC_EC_model(electron_distribution_log_values=False,EC_componets_list=['EC_BLR'],
```

```
prefit_jet.save_model('prefit_jet1.pkl')
```

[ ]:

[ ]:
```
pl=prefit_jet.plot_model(sed_data=sed_data)
pl.add_residual_plot(prefit_jet,sed_data)
pl.setlim(x_min=1E7,y_min=1E-18)
```

[ ]:
```
from jetset.jet_model import Jet
jet_minuit=Jet.load_model('prefit_jet1.pkl')
jet_minuit.set_gamma_grid_size(200)
```

[ ]:
```
fit_model_minuit=FitModel( jet=jet_minuit, name='Zone B [SSC+EC]',template=None)
jet_minuit.show_model()
```

[ ]:
```
from jetset.minimizer import fit_SED,ModelMinimizer
from jetset.model_manager import  FitModel
from jetset.jet_model import Jet
```

[ ]:
```
#Minuit
#fit_model_minuit=FitModel( jet=jet_minuit, name='Only-Synch-best-fit-minuit')␣
 ↪#Only-Synch-best-fit-minuit
fit_model_minuit.freeze('jet_leptonic','z_cosm')
fit_model_minuit.freeze('jet_leptonic','R_H')
fit_model_minuit.freeze('jet_leptonic','R')
fit_model_minuit.freeze('jet_leptonic','p')
fit_model_minuit.freeze('jet_leptonic','p_1')
########################################
fit_model_minuit.freeze('jet_leptonic','R_H')
#fit_model_minuit.freeze('jet_leptonic','L_Disk')
fit_model_minuit.freeze('jet_leptonic','R_BLR_in')
fit_model_minuit.freeze('jet_leptonic','R_BLR_out')
fit_model_minuit.freeze('jet_leptonic','tau_BLR')
fit_model_minuit.freeze('jet_leptonic','T_Disk')
########################################################
#fit_model_minuit.freeze('jet_leptonic','gmin')
fit_model_minuit.freeze('jet_leptonic','gamma_break')
fit_model_minuit.jet_leptonic.parameters.R_H.fit_range=[1E15,1E18]
fit_model_minuit.jet_leptonic.parameters.gmin.fit_range=[150,3133]
fit_model_minuit.jet_leptonic.parameters.gmax.val=1E5
fit_model_minuit.jet_leptonic.parameters.gmax.fit_range=[1E4,1E8]
fit_model_minuit.jet_leptonic.parameters.R.fit_range=[1E15,5E18]
fit_model_minuit.jet_leptonic.parameters.gamma_break.fit_range=[400,12669]
fit_model_minuit.jet_leptonic.parameters.p.val=2.12
fit_model_minuit.jet_leptonic.parameters.p_1.val=2.8
fit_model_minuit.jet_leptonic.parameters.gmin.val=300
fit_model_minuit.jet_leptonic.parameters.gamma_break.val=1000
```

```
#####################################################################
fit_model_minuit.freeze('jet_leptonic','R_H')
fit_model_minuit.freeze('jet_leptonic','L_Disk')
fit_model_minuit.freeze('jet_leptonic','R_BLR_in')
fit_model_minuit.freeze('jet_leptonic','R_BLR_out')
fit_model_minuit.freeze('jet_leptonic','tau_BLR')
fit_model_minuit.freeze('jet_leptonic','T_Disk')
fit_model_minuit.jet_leptonic.parameters.tau_BLR.val=0.13
fit_model_minuit.jet_leptonic.parameters.R_BLR_in.val=9.534279e+15
fit_model_minuit.jet_leptonic.parameters.R_BLR_out.val=1.906856e+16
fit_model_minuit.jet_leptonic.parameters.L_Disk.val=6.12e+44
fit_model_minuit.jet_leptonic.parameters.R_H.val=1.3699e+17
```

[ ]:

[ ]:
```
model_minimizer_minuit=ModelMinimizer('minuit')
best_fit_minuit=model_minimizer_minuit.fit(fit_model_minuit,sed_data,10**7.
 ↪,10**29.0,fitname='Zone B [SSC+EC]',repeat=3)
```

[ ]:
```
from IPython.core.display import HTML
HTML("""
<style>
.output_png {
    display: table-cell;
    text-align: center;
    vertical-align: middle;
}
</style>
""")
```

[ ]:
```
best_fit_minuit.save_report('SSC-best-fit-jet1-minuit.txt')
model_minimizer_minuit.save_model('model_minimizer_jet1_minuit.pkl')
fit_model_minuit.save_model('fit_model_jet1_minuit.pkl')
```

[ ]:
```
best_fit_minuit.bestfit_table
```

[ ]:
```
%matplotlib inline
fit_model_minuit.set_nu_grid(1E6,1E30,200)
fit_model_minuit.eval()
p2=fit_model_minuit.plot_model(sed_data=sed_data)
p2.setlim(y_min=1E-16,y_max=1E-8,x_min=1E6,x_max=1E29)

plt.savefig('BLLac_jet1.png', dpi=1000)
```

[ ]:
```
jet_minuit.energetic_report()
```

[ ]:

```
[ ]: ##########################################################################################

[ ]: ##########################################ZONE A
     ##################################################################3

[ ]: from jetset.sed_shaper import  SEDShape
     my_shape=SEDShape(sed_data)
     my_shape.eval_indices(silent=True)
     p1=my_shape.plot_indices()
     p1.rescale(y_min=-15,y_max=-6)

[ ]: mm,best_fit=my_shape.sync_fit(check_BBB_template=True,
                                  check_host_gal_template=False,
                                  use_log_par=True,
                                  Ep_start=None,
                                  minimizer='minuit',
                                  silent=True,
                                  fit_range=[14.5,17.5])

[ ]: my_shape.IC_fit(fit_range=[17.5,26],minimizer='minuit', silent=True)
     p1=my_shape.plot_shape_fit()
     p1.rescale(y_min=-15)

[ ]: from jetset.obs_constrain import ObsConstrain
     from jetset.model_manager import  FitModel
     from jetset.minimizer import fit_SED
     sed_obspar=ObsConstrain(beaming=28.50,
                             B_range=[0.000011,0.406],
                             distr_e='bkn',
                             t_var_sec=2.0*86400,
                             nu_cut_IR=3.0E12,
                             SEDShape=my_shape)
     prefit_jet=sed_obspar.
      constrain_SSC_EC_model(electron_distribution_log_values=False,EC_componets_list=['EC_BLR'],

[ ]: #jet_minuit.spectral_components.sync.state='off' ##############Switch off the
      Synch Component
     #jet_minuit.show_model()

[ ]: prefit_jet.eval()
     p1=prefit_jet.plot_model(sed_data=sed_data)
     p1.add_residual_plot(prefit_jet,sed_data)
     prefit_jet.save_model('prefit_jet2.pkl')

[ ]: jet_minuti=Jet.load_model('prefit_jet2.pkl')
     jet_minuti.set_gamma_grid_size(100)
     fit1_model_minuit=FitModel( jet=jet_minuti, name='Zone A')
```

```
fit1_model_minuit.show_model_components()
```

[ ]:
```
jet_minuti=Jet.load_model('prefit_jet2.pkl')
jet_minuti.set_gamma_grid_size(100)
fit1_model_minuit=FitModel( jet=jet_minuti, name='Zone A [SSC+EC]')
fit1_model_minuit.freeze('jet_leptonic','z_cosm')
fit1_model_minuit.freeze('jet_leptonic','R_H')
fit1_model_minuit.freeze('jet_leptonic','L_Disk')
fit1_model_minuit.freeze('jet_leptonic','R')
fit1_model_minuit.freeze('jet_leptonic','R_BLR_in')
fit1_model_minuit.freeze('jet_leptonic','R_BLR_out')
fit1_model_minuit.freeze('jet_leptonic','p')
fit1_model_minuit.freeze('jet_leptonic','tau_BLR')
fit1_model_minuit.freeze('jet_leptonic','T_Disk')
fit1_model_minuit.jet_leptonic.parameters.R.fit_range=[1E14,5E18]
fit1_model_minuit.jet_leptonic.parameters.gamma_break.val=600
fit1_model_minuit.jet_leptonic.parameters.p.val=1.7
fit1_model_minuit.jet_leptonic.parameters.gamma_break.fit_range=[50,2000]␣
 ↪#400,1500
fit1_model_minuit.jet_leptonic.parameters.R_H.fit_range=[1E15,5E18]
fit1_model_minuit.jet_leptonic.parameters.gmax.val=1E5
fit1_model_minuit.jet_leptonic.parameters.gmax.fit_range=[1000,1E6]
fit1_model_minuit.jet_leptonic.parameters.tau_BLR.val=0.13
fit1_model_minuit.jet_leptonic.parameters.p_1.val=2.50
fit1_model_minuit.jet_leptonic.parameters.R_BLR_in.val=9.534279e+15
fit1_model_minuit.jet_leptonic.parameters.R_BLR_out.val=1.906856e+16
fit1_model_minuit.jet_leptonic.parameters.L_Disk.val=6.12e+44
fit1_model_minuit.jet_leptonic.parameters.R.val=2.7e+15
fit1_model_minuit.jet_leptonic.parameters.R_H.val=1.3699e+17
#fit_model_minuit.jet_leptonic.parameters.beam_obj.fit_range=[5,50]
```

[ ]:
```
from jetset.minimizer import ModelMinimizer
model1_minimizer_minuit=ModelMinimizer('minuit')
best_fit2_minuit=model1_minimizer_minuit.
 ↪fit(fit1_model_minuit,sed_data,1E11,1E29,fitname='Zone A [SSC+EC]',repeat=3)
```

[ ]:
```
best_fit2_minuit.save_report('EC-BL-best-jet2-minuit.txt')
model1_minimizer_minuit.save_model('EC_BL_jet2_minimizer_minuit.pkl')
fit1_model_minuit.save_model('EC_BL_fit_jet2_minuit.pkl')
```

[ ]:
```
%matplotlib inline
fit1_model_minuit.set_nu_grid(1E6,1E30,200)
fit1_model_minuit.eval()
p3=fit1_model_minuit.plot_model(sed_data=sed_data)
p3.setlim(y_min=1E-15,y_max=1E-8,x_min=1E6,x_max=1E28)
plt.savefig('Flare_jet2.png', dpi=1000)
```

```
[ ]: ##########################################################################################

[ ]: jet_minuti.energetic_report()

[ ]:

[ ]: ######################Two zone
     model################################################

[ ]: my_jet=fit1_model_minuit.load_model('EC_BL_fit_jet2_minuit.pkl')
     composite_model=FitModel(nu_size=500,name='Combined model')
     composite_model.add_component(my_jet)
     composite_model.show_model_components()

[ ]: composite_model=FitModel(nu_size=500,name='Two-zone model')
     composite_model.add_component(my_jet)

[ ]: #j2=Jet.load_model('fit_model_jet1_minuit.pkl')
     steady_jet=fit_model_minuit.load_model('fit_model_jet1_minuit.pkl')
     composite_model.add_component(steady_jet)
     composite_model.show_model_components()
     #composite_model.steady_jet.IC_nu_size=150

[ ]:

[ ]: composite_model.save_model('composite.pkl')

[ ]: composite_model.show_pars()

[ ]:

[ ]: ####################

[ ]: from jetset.data_loader import ObsData
     from jetset.plot_sedfit import PlotSED
     from jetset.test_data_helper import  test_SEDs

     sed_data=ObsData.load('Blacertae_flare_jet.pkl')

     cm=composite_model.load_model('composite.pkl')

     import matplotlib.pylab as plt
     p4=cm.plot_model(sed_data=sed_data)
     p4.setlim(y_min=1E-13,x_min=1E8,x_max=1E28)
     plt.savefig('2_zone.png', dpi=1000)
```

```
[ ]: ##########################################################SHERPA␣
     ↪FITTING###################################
```

```
[ ]: from jetset.jet_model import Jet
     from jetset.minimizer import ModelMinimizer
     from jetset.sherpa_plugin import JetsetSherpaModel

     model_minimizer_lsb=ModelMinimizer('sherpa')
     best_fit=model_minimizer_lsb.
      ↪fit(composite_model,sed_data,1E10,1E29,fitname='Two-zone model',repeat=3)
```

```
[ ]:
```

```
[ ]: composite_model.eval()
     p5=composite_model.plot_model(sed_data=sed_data)
     p5.setlim(y_min=1E-13,x_min=1E8,x_max=1E28)
     plt.savefig('3_zone.png', dpi=1000)
```

```
[ ]:
```